WCAP-10989

COBRA-NC, ANALYSIS FOR A MAIN STEAMLINE BREAK IN THE CATAWBA UNIT 1 ICE CONDENSER CONTAINMENT

NOVEMBER, 1985

AUTHORS

L. E. HOCHREITER
P. A. LINN
D. S. NIXDORF
J. C. RECK

CONTENTS

a,c

LIST OF TABLES

TABLE

LIST OF FIGURES

SUMMARY

A series of simulations have been performed for a main steamline break in the Catawba Ice Condenser containment. The simulations were performed to predict the local atmosphere temperature and non-condensable gas distribution in the lower containment and the effect of ice condenser drain water flowing into the lower compartment on the atmospheric temperature.

The results indicate that the lower containment is well mixed, both vertically and around the containment. Except for some nearly isolated outer compartments, there was very little air left in the lower containment after the first few seconds following the pipe rupture. The temperature distribution around the lower containment was relatively flat as a result of the mixing induced by the break jet.

For the simulations that included a model for the drain flows into the lower containment, the peak bulk and local temperatures during the transient were below the environmental qualification limit.

1.0 INTRODUCTION

A postulated main steam line break (MSLB) in an ice condenser containment could potentially lead to superheated steam temperatures in the lower containment. Tube uncovery in the steam generator can result in superheated steam injection into the lower containment through the break. Large, double-ended breaks do not result in significant superheat because the entrained liquid in the steam jet is sufficient to eliminate most of the superheat. Small split breaks also do not result in significant lower containment superheat because containment sprays in the upper containment and recirculating fans between the upper and lower containments are on before the steam generator tubes uncover. Sensitivity analyses by Westinghouse (1) indicate that the worst case situation in terms of lower containment superheat occurs with a break size of 0.86 ft.2 The steam generator tubes begin to uncover at about 100 seconds after the rupture for this break size with the recirculating deck fans coming on at 600 seconds.

The COBRA-NC code was used to perform a series of simulations for a 0.86 $ft.^2$ MSLB in one of the Catawba ice condenser containments. Catawba Units 1 and 2 are essentially mirror images of each other. While this analysis was specifically for Unit 1, plant data was more readily available for Unit 2 and was, therefore, used to generate code input. The purpose of these calculations is to examine the containment response to a MSLB as realistically as possible. In this fashion, such items as three-dimensional flow behavior, non-condensable concentration, and mixing effects caused by the break can assessed and compared to the simplier more conservative licensing calculation. During the transient, ice melt and steam condensate drain into the lower containment from the ice condenser bays. This drain water was expected to have a major impact on lower containment temperatures. A drain model was incorporated into COBRA-NC that caused the drain water to be dispersed in the lower containment as drops and films using an upper bound drop size from the drain flow test data obtained by Westinghouse.[2] One simulation was run with the drain flow discarded so that the magnitude of the increased cooling due to the drain flow could be assessed.

While these COBRA-NC calculations have been specifically performed on the Catawba Units, it is believed that the response of other Westinghouse ice condenser plants would be very similar since the containment design of the units is nearly the same. Table 6.1 in Section 6, provides a comparison of the TVA and Duke Power ice condenser plant containment parameters. As this table indicates, the dominant containment variables such as containment volume, steel mass and concrete heat sinks are nearly identical for all plants. Some small differences between plants will exist for the thin metal surface areas for films to collect and condensate to evaporate. However, as will be shown in this report, the long term containment bulk temperature becomes more dependent on the concrete and thick steel heat sinks (such as, structures for steam generator support and pump supports) rather than the thin metal heat sinks.

Section 2 of this report describes the physical geometry of the containment and outlines the accident scenario. A brief description of the COBRA-NC code is presented in Section 3. Complete details of the basic COBRA-NC code are available in the code documentation.[3] The heat transfer models are discussed in detail in this report as they are somewhat different than those described in the code documentation.

Section 4 describes code modifications made especially for these simulations. The code input data is presented in Section 5 and the results for the simulation series are discussed in Section 6. Conclusions are drawn in Section 7.

2.0 CATAWBA ICE CONDENSER CONTAINMENT DESCRIPTION

A sectional elevation of an ice condenser containment is shown in Figure 2.1. A 3.0 foot thick outer concrete shell surrounds the 1.0 inch thick steel containment shell. The interior of the containment is divided into four major regions; the reactor vessel enclosed by the biological shield wall (BSW), the lower containment, the ice condensers and the upper containment. The reactor vessel region connects to the lower containment through ventilation holes and ducting near the top of the 4 ft. thick BSW and through the instrument tunnel to the sump region surrounding the bottom of the reactor vessel. The upper and lower containment are separated bv the operating floor located 54 ft. above the containment floor. There is approximately 2 $ft.^2$ of known leakage area between the upper and lower containment.

A plan view of the lower containment is shown in Figure 2.2. The view is at the elevation of the ice condenser doors, just below the operating floor. There are 24 sets of double doors between the lower compartment and the ice condenser. Each double door opening is approximately 60 $ft.^2$, although the maximum door opening is about one-half that. The dividers between the doors are part of the 3.0 ft. thick wall that supports the polar crane in the upper containment.

Located directly below most of the ice condenser doors are the ice condenser drains. [

]a,c

Between the crane wall and the containment shell are outer compartments that house the accummulator, ventilating equipment and some instrumentation. These compartments communicate with the lower containment through openings where pipe, ducts and cables pass through the crane wall. Most of the compartments are similarly connected to adjacent compartments.

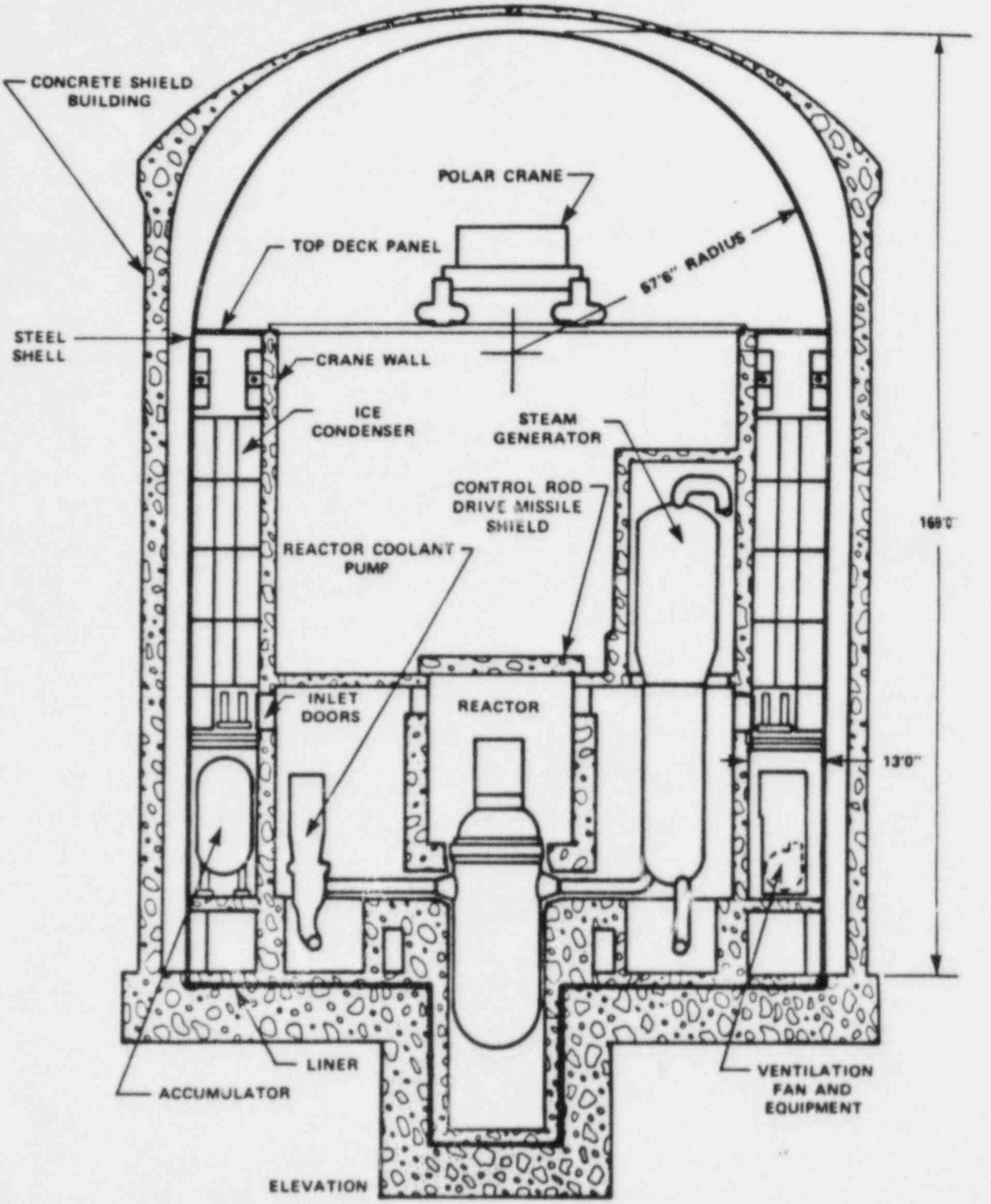

FIGURE 2.1. Typical Ice Condenser Containment

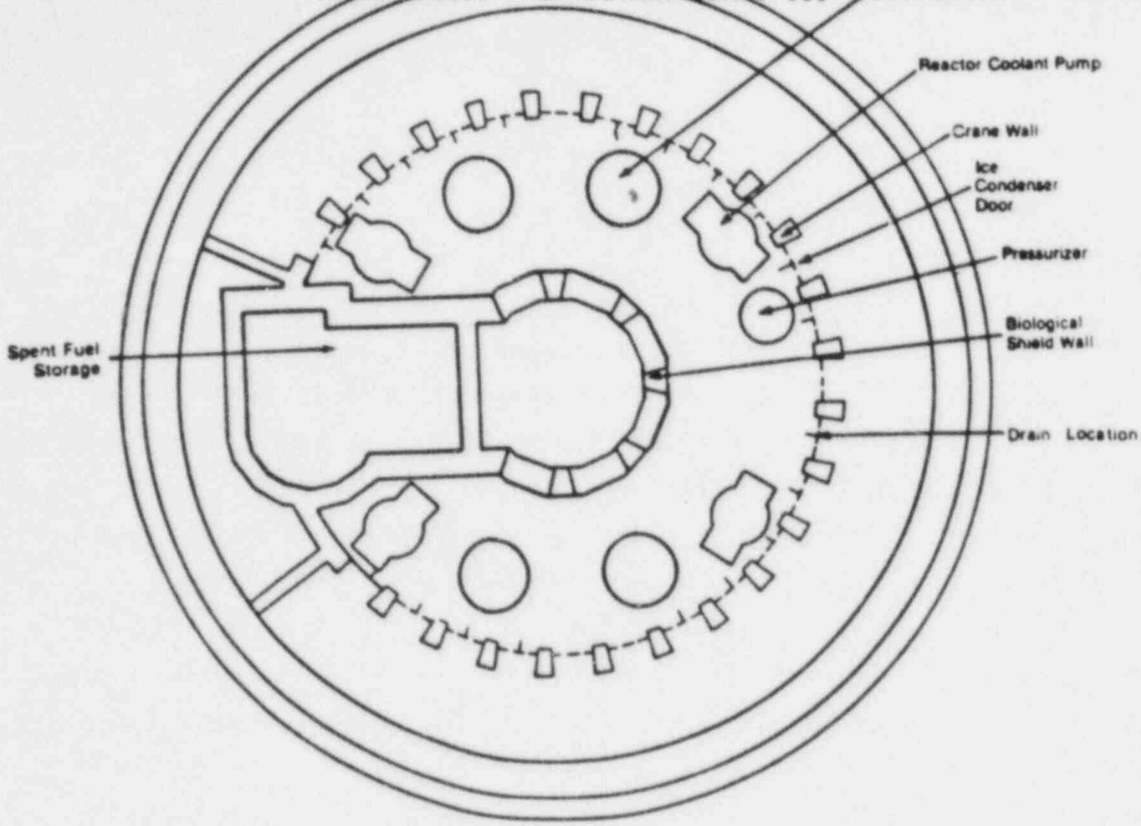

FIGURE 2.2. Lower Containment - Ice Condenser Door Elevation

An 8 ft. high pipe tunnel runs underneath the spent fuel storage region so that there is flow communication around the full 360° at this level. Above this level, the lower containment has the "C" shape shown in Figure 2.2.

Also shown in Figure 2.2 are the reactor coolant pumps (RCP), steam generators, and the pressurizer. The steam generators and pressurizers extend approximately 30 ft. above the operating floor. Enclosures cover the tops of inside the vessel enclosure is considered part of the lower containment. The enclosures are shown in Figure 2.3.

The ice condenser bays are between the crane wall and the containment shell and directly above the outer compartments in the lower containment. Figure 2.3 shows a plan view of the ice condenser, the vessel enclosures and the lower part of the upper containment. The ice condenser consists of 24 modules, each consisting of a 9 x 9 array of ice baskets. The baskets are cylindrical, open lattice, thin steel structures approximately 48 ft. long. A total of about 2.4 million pounds of .1 inch thick flake ice is loaded into the ice baskets. The bottom of the ice baskets is about 11 ft. above the floor of the ice condenser to allow room for the doors to swing open and for the turning vanes that turn and distribute the incoming steam. The doors are vertically hinged and are held shut under normal operation by the static head of the cold air in the ice condensers. The doors open fully with a pressure differential of 0.0015 psi. Ice condenser cooling equipment is located in the region above the ice baskets and below the top deck doors. These doors open to allow air and small amounts of residual steam to enter the upper containment.

The upper containment includes the dome region and all of the open volume outside of the ice condensers and vessel enclosures above the operating floor. The spent fuel storage region is also open to, and considered part of, the upper containment. Containment spray nozzles are located in the upper half of the dome.

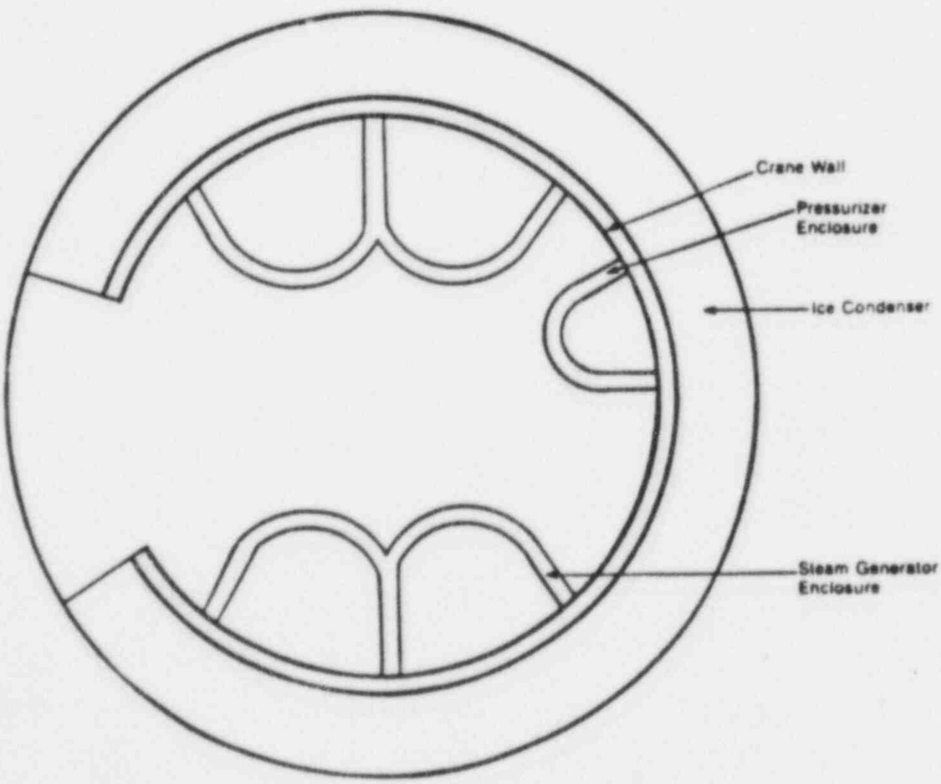

FIGURE 2.3. Upper Containment - Ice Condenser And Vessel Enclosures

2.1 Operation During Steamline Break

In the event of a pipe break on the secondary side in the lower containment, the entering steam will rapidly pressurize the lower containment and force the ice condenser doors open. Air in the lower containment is forced up through the ice condenser and into the upper containment. Essentially all of the steam that enters the ice bays condenses so that the overall pressurization of the containment is limited to the pressure increase resulting from the compression of the initial containment atmosphere into the upper part of the containment.

Ice melt and steam condensate collect at the bottom of the ice bays and run out the drain pipes. The flapper valves on the drains spread the drain flow into a fan that rapidly breaks up into droplets. The drain flow also covers much of the equipment in the lower containment with liquid films. Condensation occurs on the drain flow until the water reaches the saturation temperature. Some of the drain water will be vaporized and the steam will be cooled in the process if the lower containment steam is superheated.

a,c

2.2 COBRA-NC Noding for Catawba

This section contains a general description of the noding capabilities of the COBRA-NC code and then presents the noding used for the Catawba ice condenser containment simulations. Three MSLB simulations were performed. Models 1 and 2 used the noding described in this section. The noding for Model 3 was altered and is described in Section 6.0.

Any geometry modeled using the COBRA-NC code is represented as a matrix of Eulerian mesh cells. The number of mesh cells used depends on the degree of detail required to resolve the flow field, the phenomena being modeled, and practical restrictions such as computing costs and core storage limitations. In two-phase flow, the mesh cell should be large compared to the characteristic size of the two-phase flow pattern. For example, the mesh cell size should be large relative to the drop size so that the averaged quantities (drop size, drag, etc.) used in the calculation will be valid. In slug or film flow, the mesh cell size should be on the order of the hydraulic diameter or larger since the physical models for these flow regimes are based on the physical dimensions of the flow path. These conditions have been met in this analysis.

The equations for the flow field are solved using a staggered difference scheme on the Eulerian mesh. The velocities are obtained at mesh cell faces, and the state variables (e.g., pressure, density, enthalpy and phase volume fractions) are obtained at the cell center. The mesh cell is characterized by cross-sectional area A, height ΔX, and the width of the connections to adjacent mesh cells, S. The basic mesh cell is shown in Figure 2.4. This cell is the control volume for the scalar continuity and energy equations. The momentum equations are solved on a staggered mesh with the momentum cells centered on the scalar cell faces. The momentum cell for vertical velocities is shown in Figure 2.5 and that for transverse velocities in Figure 2.6.

The input has been constructed to allow a great deal of flexibility in defining the mesh for the irregular geometries typical of nuclear containments. The mesh cells are defined by input in terms of channels. A channel is simply a vertical stack of mesh cells, as illustrated in Figure 2.7.

Boundary data for each channel are stored in phantom nodes at its top and bottom. Between these two phantom nodes are NDX nodes that actually enter into the calculation. Node J = 1 contains boundary conditions for the bottom of the channel, and node J = NDX + 2 contains boundary conditions for the top of the channel. Boundaries between mesh cells are identified in Figure 12 with the lower case j and refer to the location of the momentum cell center where velocities are obtained. The velocity corresponding to j = 1 is at the top of the continuity mesh cell corresponding to J = 1.

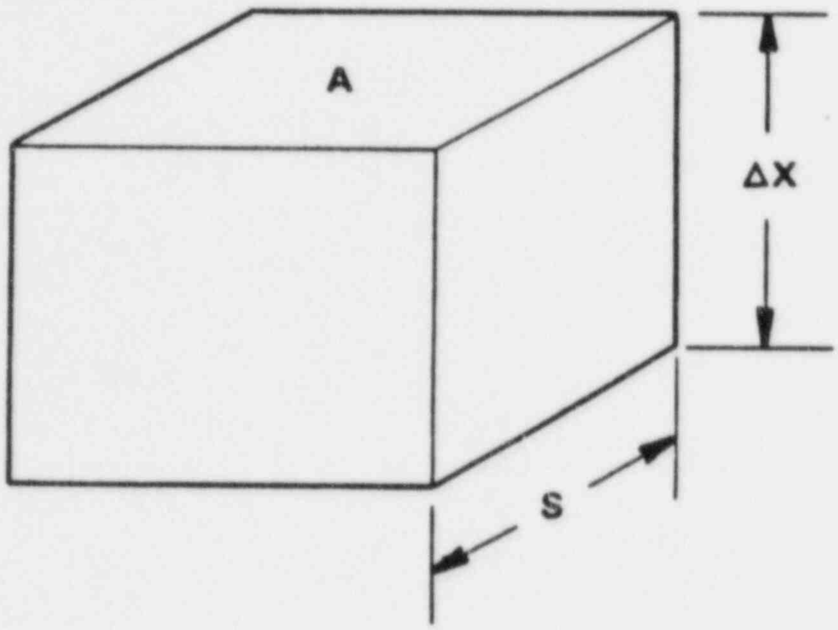

FIGURE 2.4. Mesh Cell For Scalar Equations

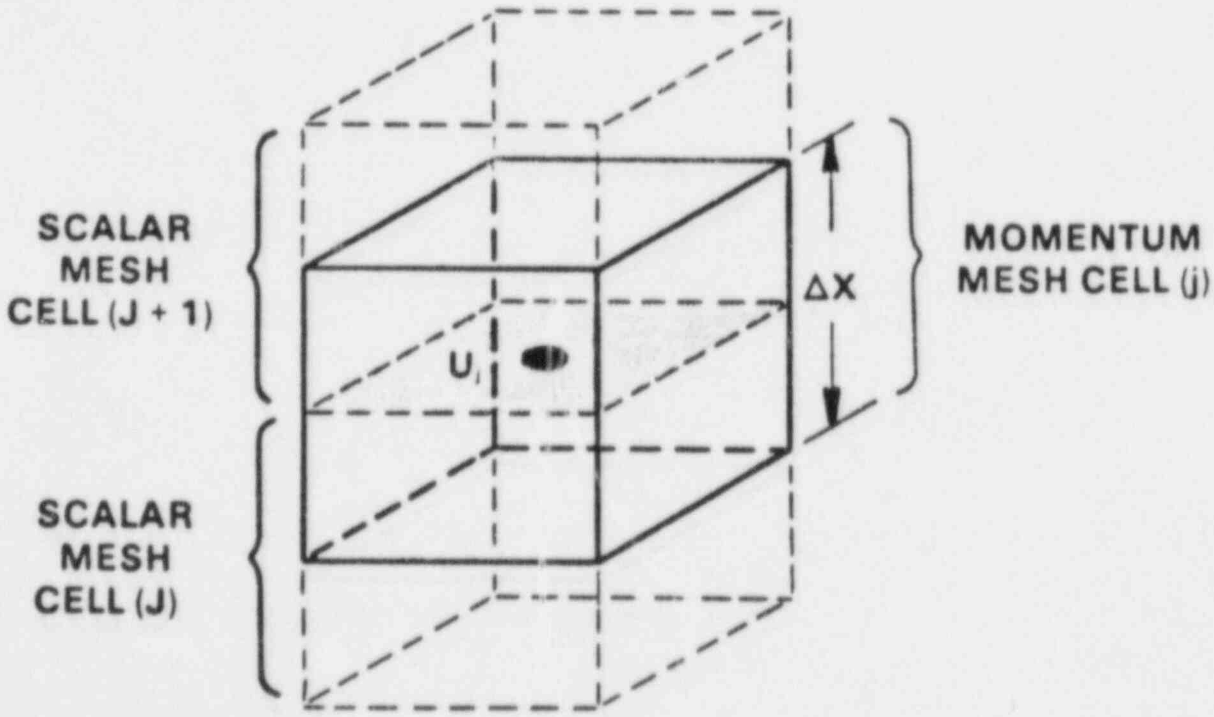

FIGURE 2.5. Control Volume For Axial Momentum

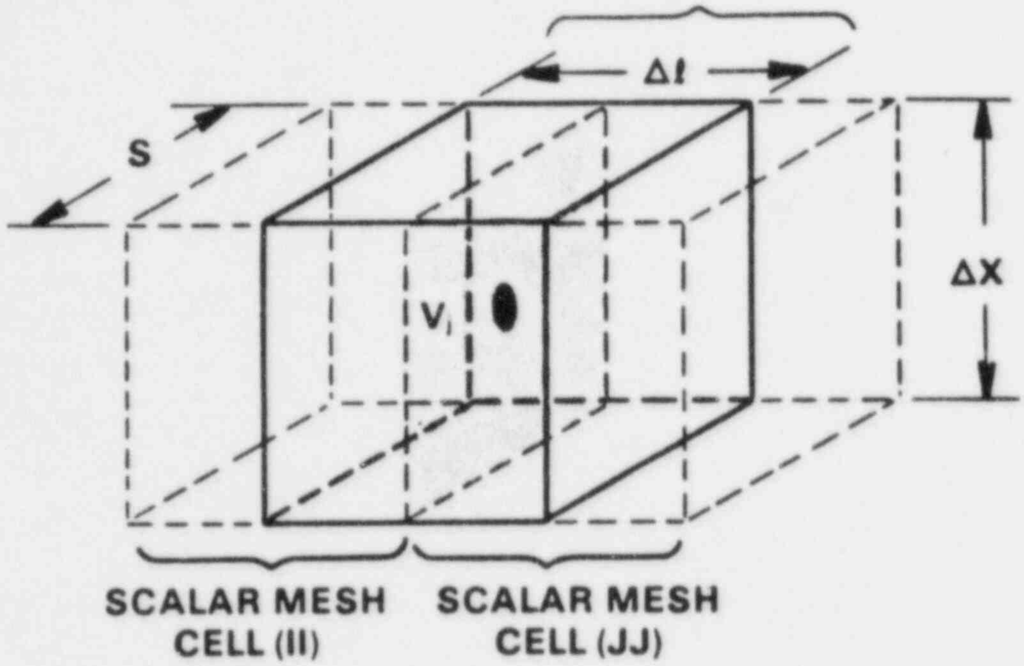

FIGURE 2.6. Control Volume For Transverse Momentum

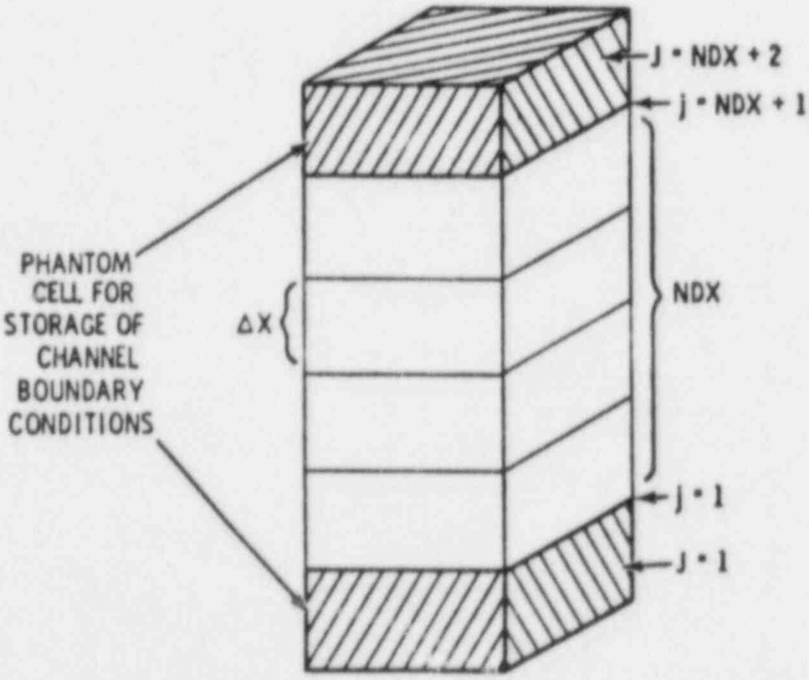

FIGURE 2.7. Channel Noding and Notation

Nominal flow area and wetted perimeter are specified for each channel by input. Each mesh cell within the channel is assumed to have the nominal geometry unless the user specifies a variation for area or wetted perimeter. The mesh for a particular region of the containment is developed by placing a sufficient number of channels in the region to model the geometry and the important flow phenomena of the region. Transverse connections are specified between the channels to complete the multidimensional mesh for the region. These transferse connections are referred to as gaps. Gaps are defined by the width of the flow path between the two channels and the distance between the channel centers. The width of the gap between channels is assumed to be uniform along the total length of the channels unless a vertical variation of the gap is specified. The centroid distance is always equal to the nominal value for the gap; no variation is allowed.

The flexible noding capabilities of the COBRA-NC code allows for very nonuniform meshes. Some cautioned must be exercised to minimize the errors associated with a nonuniform mesh. The COBRA-NC code uses a donor cell differencing scheme which introduces some numerical diffusion into the solution. As a uniform mesh decreases in size, the artificial diffusion coefficient approaches zero. However for a nonuniform mesh, if the mesh is reduced such that the cell-size ratios are maintained, the artificial diffusion coefficient does not disappear. In practice, this is generally not a problem since the mesh refinement can be done in a manner that makes the mesh more uniform as it becomes smaller.

For reactor and containment analysis, the more important consideration is the numerical diffusion that is associated with the large cell size. The artificial coefficient has the general form of $.5U\ \delta Z\ (1-CN)$ where U, δZ and CN are the local velocity, length scale and courant number, respectively. The ratio of numerical diffusional to convective transport is (1-CN). The computational time step is usually limited by the courant condition in some local high velocity region. In this high velocity region, CN is close to unity and so the relative numerical diffusion is small. In regions where the courant number is small, the numerical diffusion can be more significant although it is limited to a value that effectively doubles the convective transport.

For nonuniform meshes, at the scale generally used for reactor analysis, the numerical diffusion coefficient is either increased or decreased depending on whether the velocity is from the larger to the smaller cell or vice-versa. Since diffusional terms generally enhance the stability of numerical fluid mechanics solution algorithums, attempts to remove or reduce the numerical diffusion invariably result in less stable schemes. The influence of noding on numerical diffusion should be kept in mind while constructing a model for a particular simulation. It may be noted that reasonable results have been obtained for various reactor analysis problems where the size of adjacent nodes varies by a factor of two or more.(3)

The vertical elevations of the mesh may be grouped into one or more regions or sections. Figure 2.8 shows the axial mesh divisions for the Catawba containment. The mesh is divided into 5 sections, each having its own grid layout when viewed from above. Section A constitutes the sump/instrument tunnel region. It is modeled with a single channel made up of two cells as shown in Figure 2.9

[ ]a,c The numbers on the mesh are the channel numbers. The grid layout is essentially cylindrical except in the vicinity of the spent fuel storage region. One channel was used to model the reactor vessel enclosure (Channel 2), and one for the spent fuel storage area and the pipe tunnel below (Channel 3). Channel 2 is connected to the lower containment only through the ventilation ducts and holes at the top of the biological shield wall. The bottom two cells of Channel 3 are connected to the lower containment but the spent fuel storage region is isolated from the lower containment. Channels 4, 8, 12, 16, 20, 24, 28, and 32 model the outer compartments. [ ]a,c A circle in a cell indicates a connection to the interior region of the lower containment. Most of the compartments are connected vertically and to the interior of the lower

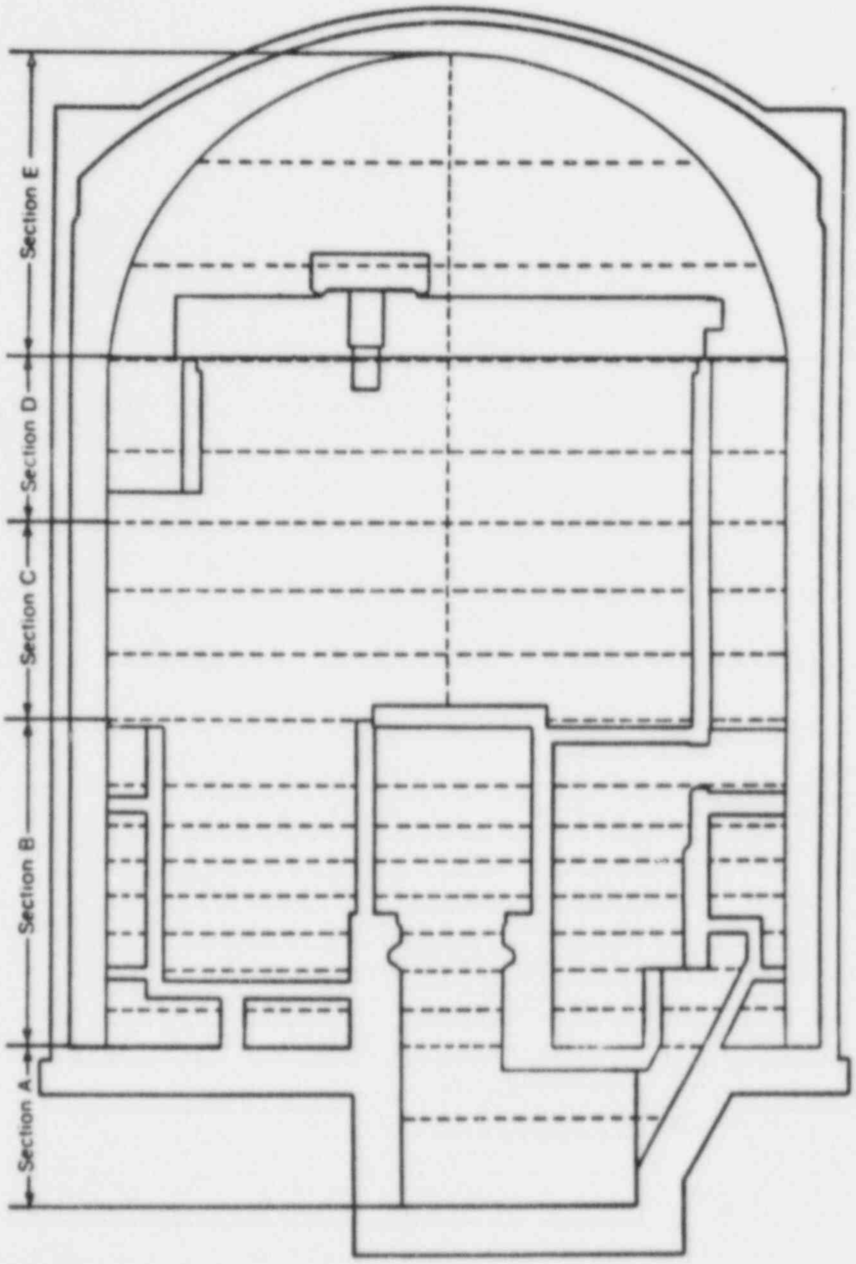

FIGURE 2.8. Axial Mesh For Catawba, Models 1 and 2

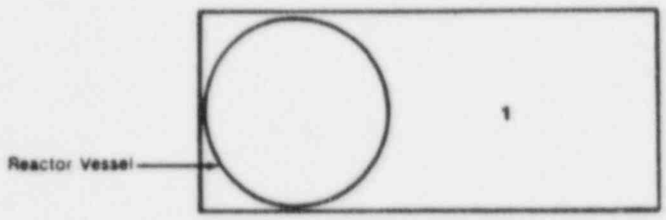

FIGURE 2.9. Section A - Sump/Instrument Tunnel

a,c

FIGURE 2.10.

[ ]a,c

FIGURE 2.11. [ ]a,c

containment. Above the bottom two cells there is very little lateral communication between the outer compartments.

The interior of the lower containment is divided into three radial rings and 8 sectors. The details of the flow connections and the open volumes in this region will be discussed in Section 5 on the code input. The top level of Section B includes the openings to the ice condensers.

[ ]a,c The ice condensers are modeled using a single ring and 8 sectors. The steam generator enclosures are modeled with four channels each and two channels are used for the pressurizer enclosure. Using multiple channels for these enclosures ensures that circulation patterns will be allowed to deveop within the enclosures. Five channels are used to model the open upper containment region in Section C and one channel is used to model the region adjacent to the equipment hatch. The vessel enclosures are sealed at the top of Section C.

a,c

FIGURE 2.12.

a,c

a,c

The noding in the ice condenser is consistent with that in Section C. Two channels are used to model the region between the ends of the ice condenser. This region was split into two channels because of cell coupling limitations in COBRA-NC.

a,c

The sections are joined together to form the complete containment mesh by specifying connections to the channels in adjacent sections at the top and bottom of each channel. The ability to connect one or more channels to the top or bottom of a channel is referred to as channel-splitting. Each channel and gap in the problem is assigned a unique identification number by the input, and these channel numbers are use to identify the connections at the

[ ]a,c

FIGURE 2.13. [ ]a,c

[ ]a,c

FIGURE 2.14. [ ]a,c

top and bottom of each channel. Connections are not specified for channels without a physical flow path at the inlet or outlet. The lower and upper containment region, for example, are separated by the operating floor and the vessel enclosures, so the channels in the open region of the upper containment do not connect to channels in the open region of the lower containment. Similarly, the tops of the channels in the dome and the bottoms of those in the lower containment model the physical boundaries of the containment. Zero flow boundary conditions on the ends of channels that do not connect to channels in an adjacent section are specified by input. This is done at the bottom of most channels in the lower containment and the top of all channels in the dome.

The noding schemes were chosen to provide sufficient detail in the lower containment so that temperature and air concentrations could be predicted. While finer noding may be desireable, particularly in the vicinity of the jet, practical considerations on CPU time requirements limit the allowable mesh fineness. Further details on the modeling in each section are given in Section 5.

3.0 COBRA-NC CODE DESCRIPTION

The COBRA-NC Code is an extension of the COBRA-TF code that was developed to predict the thermal-hydraulic response of nuclear reactor components, primarily the reactor vessel and internals. The flexible noding capability and the addition of non-condensable gas fields make COBRA-NC suitable for modeling transients in reactor containment buildings.

The COBRA-NC computer code provides a two component, two-fluid, three-field representation of two-phase flow. Each field is treated in three dimensions and is compressible. Continuous vapor, continuous liquid and entrained liquid drops are the three fields. The vapor field consists of steam and any number of noncondensable gas components. The properties for eight different gases are available in the code. The conservation equations for each of the three fields and for heat transfer from and within the solid structures in contact with the fluid are solved using a semi-implicit, finite-difference numerical technique on an Eulerian mesh. COBRA-NC features extremely flexible noding for both the hydrodynamic mesh and the heat transfer solution. This flexibility provides the capability to model the wide variety of geometries encountered in various components of nuclear reactors, including the containment building.

The documentation for the COBRA-NC and COBRA-TF codes is broken up into several volumes because of their wide range of application. Volume 1, Equations and Constitutive Models, contains a description of the basic conservation equations and constitutive models used in the code. Volume 2 contains the finite-difference equations and a description of the procedures used for their numerical solution. Volumes 3 through 5 are the User's Manuals. They contain line-by-line input instructions for COBRA-NC and user guidance for application of the code. Volume 3 is the User's Manual for General Two-Phase Thermal Hydraulics. This volume contains an explanation for all of the input data required for general application of the code. Volume 4 is the User's Manual for Containment Analysis. This volume contains an explanation of the input data required for containment analysis only. It also provides examples of containment modeling procedures. Volume 5 is the Users'

Manual for Flow Blockage and Hot Bundle Analysis and describes the input required for performing such analysis.

Volumes 6, 7, and 8 are the Assessment Manuals. They contain the results of simulations run to assess the performance of the code.in each of the areas discussed above. Volume 9 is the Programmers' Manual. It explains the details of COBRA-NC's working parts from a programmers' viewpoint. The structure of the code is described along with a verbal description of the major variables and subroutines used in the code.

A brief description of the code will be given here to familiarize the reader with the code and how it is used in the present analysis. The three- field conservation equations, together with the physical models required to effect closure of these equations, constitute the basic model for two-phase flow used in COBRA-NC. The constitutive relations include state-of-the-art physical models for the interfacial mass transfer, the interfacial drag forces, the liquid and vapor wall drag, the wall and interfacial heat transfer, the rate of entrainment and deentrainment, and the thermodynamic properties of water and noncondensable gases.

The time and space averaged conservation equations used in COBRA-NC are derived following the methods of Ishii.[4] The average used is a simple Eulerian time average over a time interval, Δt , assumed to be long enough to smooth out the random fluctuations present in a multiphase flow but short enough to preserve any gross unsteadiness in the flow. The resulting average equations can be cast in either the mixture form or the two-fluid form. Because of its greater physical appeal and broader range of application, the two-fluid approach is used as the foundation for the COBRA-NC code.

The two-fluid formulation uses a separate set of conservation equations and constitutive relations for each phase. The effects of one phase on another are accounted for by interaction terms appearing in the equations. The conservation equations have the same form for each phase; only the constitutive relations and physical properties differ. Thus, although usually derived for two-phase flow, the two-fluid model immediately generalizes to n-phase flow.

The three-field formulation used in COBRA-NC is a straight forward extension of the two-fluid model. The fields included are vapor, continuous liquid, and entrained liquid. Dividing the liquid phase into two fields is the most convenient and physically reasonable wav of handling flows where the liquid can appear in both film and droplet form. In such flows the motion of the droplets can be quite different from the motion of the film, so a single set of average liquid phase equations cannot adequately describe the liquid flow or the interaction between liquid and vapor.

3.1 Two-Fluid Phasic Conversation Equations

The phasic conservation equations describe the time-averaged behavior of phase k, which can be any phase in a multiphase flow. All fluid variables appearing in these equations are time-averaged quantities. The phasic conservation equations are general within the assumptions listed below.

Assumption

1. Gravity is the only body force.
2. The pressure is the same in all phases.
3. The dissipation can be neglected in the enthalpy formulation of the energy equation.

Conservation of Mass

$$\frac{\partial}{\partial t}(\alpha_k \rho_k) + \nabla \cdot (\alpha_k \rho_k \underline{U}_k) = \Gamma_k''' + \nabla \cdot \alpha_k \rho_m \varepsilon_D \nabla W_k \qquad (3.1)$$

Rate of + change of mass	Mass flux	= Rate of mass transfer to phase k from the other phases	+ Mass flux due to turbulent diffusion

Conservaton of Momentum

$$\frac{\partial}{\partial t}(\alpha_k \rho_k \underline{U}_k) + \nabla \cdot (\alpha_k \rho_k \underline{U}_k \underline{U}_k) = \alpha_k \rho_k \underline{g} - \alpha_k \nabla P$$

$$+ \nabla \cdot \alpha_k (\underline{\underline{\tau}}_k + \underline{\underline{T}}_k^T) + \underline{M}_k^\Gamma + \underline{M}_k^d \tag{3.2}$$

Rate of change of momentum	+	Momentum flux	=	Gravity force	+	Pressure gradient force
+ Viscous and turbulent forces	+	Momentum exchange due to mass transfer to phase k	+	Interfacial drag force		

Conservation of Energy

$$\frac{\partial}{\partial t}(\alpha_k \rho_k h_k) + \nabla \cdot (\alpha_k \rho_k h_k \underline{U}_k) = - \nabla \cdot \alpha_k (\underline{Q}_k + \underline{q}_k^T) + E_k^\Gamma + q_I''' + \alpha_k \frac{\partial P}{\partial t} \tag{3.3}$$

Rate of change of enthalpy	+	Enthalpy flux	=	Conduction and turbulent heat flux
+ Energy exchange due to mass transfer to phase k	+	Interfacial heat transfer	+	Pressure derivative

The following definitions have been used in the above equations:

α_k = average k-phase volume fraction

ϵ_D = k-phase turbulent mass diffusivity

ρ_k = average k-phase density

ρ_m = average vapor/gas mixture density

$\underline{U}_k$ = average k-phase velocity

Γ_k = average rate of mass transfer to phase k from the other phases

$\underline{g}$ = acceleration of gravity

P = average pressure

$\underline{\underline{\tau}}_k$ = average k-phase viscous stress tensor (stress deviator)

$\underline{T}_k^T$ = k-phase turbulent (Reynolds) stress tensor

$\underline{M}_k^\Gamma$ = average supply of momentum to phase k due to mass transfer to phase

$\underline{M}_k^d$ = average drag force on phase k by the other phases

h_k = average k-phase enthalpy

$\underline{Q}_k$ = average k-phase conduction heat flux

$\underline{q}_k^T$ = k-phase turbulent heat flux

E_k^Γ = energy to phase k due to mass transfer to and from phase k

W_k = k-phase mass concentration

3.2 Three-Field Conservation Equations

In the two-component, three-field formulation there are four continuity equations, three momentum equations, and two energy equations. The two liquid fields are assumed to be in thermal equilibrium, within a node. The steam and noncondensable gases are assumed to have a common temperature and velocity. These equations are obtained from Equations 3.1 through 3.3 by introducing the appropriate three-fields notation and a few simplifying assumptions.

3.2.1 Three-Field Model Notation.

In general, the subscripts v, mg, ℓ and e refer to the vapor, noncondensable gas mixture, continuous liquid and entrained liquid fields, respectively. The subscript vg refers to the vapor/gas mixture. The terms associated with a change of phase are discussed below. Let

Γ''' = average rate of vapor generation per unit volume,

S''' = average net rate of entrainment per unit volume

Since both liquid fields can contribute to the vapor generation rate, let

η = the fraction of the total vapor generation coming from the entrained liquid

With the above definitions the mass transfer terms can be written as

$$
\begin{aligned}
\Gamma_v''' &= \Gamma''' \\
\Gamma_\ell''' &= -(1 - \eta)\Gamma''' - S''' \qquad (3.4) \\
\Gamma_e''' &= -\eta\Gamma''' + S'''
\end{aligned}
$$

The interfacial momentum exchange terms can be expressed as

$$
\begin{aligned}
\underline{M}_v^d &= -\,\underline{\tau}_{v\ell}''' - \underline{\tau}_{ve}''' \\
\underline{M}_\ell^d &= \underline{\tau}_{v\ell}''' \qquad (3.5) \\
\underline{M}_e^d &= \underline{\tau}_{ve}'''
\end{aligned}
$$

where

$\underline{\tau}'''_{I_{v\ell}}$ = average drag force per unit volume by the vapor/gas mixture on the continuous liquid

$\underline{\tau}'''_{I_{ve}}$ = average drag force per unit volume by the vapor/gas mixture on the entrained liquid

The momentum exchange due to mass transfer between the three fields can be written as

$$\underline{M}_k^{\Gamma} = (\Gamma'''_k \; \underline{U}) \tag{3.6}$$

It should be noted that according to Equations 3.4 and 3.6, $\underline{M}_v^{\Gamma}$ is due only to vapor generation, but $\underline{M}_\ell^{\Gamma}$ and $\underline{M}_e^{\Gamma}$ are affected by both vapor generation and entrainment.

The energy transport associated with a change of phase is given by

$$E_k^{\Gamma} = \Gamma_k''' h_k^{\Gamma}$$

where h_k^{Γ} is the transported enthalpy.

3.2.2 Three-Field Model Assumptions

To obtain the COBRA-NC three-field model from Equations 3.1 through 3.3, the following assumptions are made.

1. The turbulent stresses and turbulent heat flux of the entrained phase can be neglected, so

$$\begin{aligned} \underline{T}_e^{T} &= 0 \\ \underline{q}_e^{T} &= 0 \end{aligned} \tag{3.7}$$

2. When the equations are solved on a finite-difference grid, the viscous stresses can be partitioned into wall shear and fluid-fluid shear. The fluid-fluid shear can be neglected in the entrained liquid phase. The notation for this is given below.

$$\nabla \cdot (\alpha_e \underline{\underline{\tau}}_e) = \underline{\tau}'''_{we}$$

$$\nabla \cdot (\alpha_v \underline{\underline{\tau}}_v) = \underline{\tau}'''_{wv} + \nabla \cdot (\alpha_v \underline{\underline{\sigma}}_{vg}) \tag{3.8}$$

$$\nabla \cdot (\alpha_\ell \underline{\underline{\tau}}_\ell) = \tau'''_{w\ell} + \cdot \ (\alpha_\ell \underline{\underline{\sigma}}_\ell)$$

In Equation 3.8 $\underline{\tau}'''_{wv}, \underline{\tau}'''_{we}, \underline{\tau}'''_{w\ell}$, are the forces exerted by the wall on the vapor/gas mixture, the entrained liquid and the continuous liquid, respectively; $\underline{\underline{\sigma}}_{vg}$ and $\underline{\underline{\sigma}}_\ell$ are the fluid-fluid viscous shear stress tensors for the vapor/gas mixture and the liquid.

3. The liquid film and the entrained liquid are at the same temperature so that only one liquid energy equation is required.

4. the conduction heat flux can be partitioned into a wall term and a fluid-fluid conduction term. The latter is assumed negligible in the entrained liquid. Thus,

$$-\nabla \cdot (\alpha_v \underline{Q}_{vg}) = -\nabla \cdot (\alpha_v \underline{q}_{vg}) + Q'''_{wv}$$

$$-\nabla \cdot (\alpha_e \underline{Q}_e + \alpha_\ell \underline{Q}_\ell) = -\nabla \cdot (\alpha_\ell \underline{q}_\ell) + Q'''_{w\ell} \tag{3.9}$$

where Q'''_{wv} and $Q'''_{w\ell}$ are the wall heat transfer rates per unit volume to the vapor/gas mixture and liquid, respectively, $\underline{q}_\ell$ is the fluid-fluid conduction vector for the continuous liquid and $\underline{q}_{vg}$ is the fluid-fluid conduction vector for the vapor/gas mixture.

5. All mass entering a phase is at saturation. Therefore,

$$h_v^\Gamma = h_g \text{ (evaporation)}$$
$$h_\ell^\Gamma = h_f \text{ (condensation)} \tag{3.10}$$

All mass leaving a phase is at the phase enthalpy. Therefore

$$h_v^\Gamma = h_v \text{ (condensation)}$$
$$h_\ell^\Gamma = h_\ell \text{ (evaporation)} \tag{3.11}$$

3.2.3 Three-Field Equations

Substituting Equations 3.4 through 3.10 into Equations 3.1 through 3.3 and including separate mass equations for the noncondensable gas mixture and the vapor yields the three-field conservation equations used in COBRA-NC.

Conservation of Mass (4 equations)

$$\frac{\partial}{\partial t}(\alpha_v \rho_v) + \nabla \cdot (\alpha_v \rho_v \underline{U}_{vg}) = \Gamma_v''' + \nabla \cdot \alpha_v \rho_{vg}\, \varepsilon_D \nabla W_v + S_{cv}'''$$
$$\frac{\partial}{\partial t}(\alpha_\ell \rho_\ell) + \nabla \cdot (\alpha_\ell \rho_\ell \underline{U}_\ell) = \Gamma_\ell''' + S_{c\ell}'''$$
$$\frac{\partial}{\partial t}(\alpha_e \rho_\ell) + \nabla \cdot (\alpha_e \rho_\ell \underline{U}_e) = \Gamma_e''' + S_{ce}''' \tag{3.12}$$
$$\frac{\partial}{\partial t}(\alpha_v \rho_{mg}) + \nabla \cdot (\alpha_v \rho_{mg} \underline{U}_{vg}) = \nabla \cdot \alpha_v \rho_{vg}\, \varepsilon_D \nabla W_g + S_{cg}'''$$

Conservation of Momentum (3 equations)

$$\frac{\partial}{\partial t}(\alpha_v \rho_{vg} \underline{U}_{vg}) + \nabla \cdot (\alpha_v \rho_{vg} \underline{U}_{vg} \underline{U}_{vg}) = -\alpha_v \nabla P + \alpha_v \rho_{vg} \underline{g}$$

$$+ \nabla \cdot \alpha_v (\underline{\underline{\sigma}}_{vg} + \underline{\underline{T}}^T_{vg}) + \underline{\tau}'''_{wv} - \underline{\tau}'''_{I_{v\ell}} - \underline{\tau}'''_{I_{ve}} + (\Gamma'''_v \underline{U}) + S'''_{mv}$$

$$\frac{\partial}{\partial t}(\alpha_\ell \rho_\ell \underline{U}_\ell) + \nabla \cdot (\alpha_\ell \rho_\ell \underline{U}_\ell \underline{U}_\ell) = -\alpha_\ell \nabla P + \alpha_\ell \rho_\ell \underline{g}$$

$$+ \nabla . \ \alpha_\ell (\underline{\underline{\sigma}}_\ell + \underline{\underline{T}}^T_\ell) + \underline{\tau}'''_{w\ell} + \underline{\tau}'''_{I_{v\ell}} - (\Gamma'''_\ell \underline{U}) + S'''_{m\ell}$$

$$\frac{\partial}{\partial t}(\alpha_e \rho_\ell \underline{U}_e) + \nabla \cdot (\alpha_e \rho_\ell \underline{U}_e \underline{U}_e) = -\alpha_e \nabla P + \alpha_e \rho_\ell \underline{g} + \underline{\tau}'''_{we} + \underline{\tau}'''_{I_{ve}}$$

$$- (\Gamma'''_e \underline{U}) + S'''_{me} \tag{3.13}$$

Conservation of Energy (2 equations)

$$\frac{\partial}{\partial t} \alpha_v(\rho_v h_v + \rho_g h_g) + \nabla \cdot \alpha_v(\rho_v h_v + \rho_g h_g)\underline{U}_{vg} = -\nabla \cdot \alpha_{vg}(q_{vg} + q^T_{vg})$$

$$+ \Gamma''' h^\Gamma_v + q'''_{I_v} + Q'''_{wv} + \alpha_v \frac{\partial P}{\partial t} + S'''_{ev}$$

$$\frac{\partial}{\partial t} (\alpha_\ell + \alpha_e)\rho_\ell h_\ell + \nabla \cdot (\alpha_\ell \rho_\ell h_\ell \underline{U}_\ell) + \nabla \cdot (\alpha_e \rho_\ell h_\ell \underline{U}_e)$$

$$= -\nabla \cdot \alpha_\ell (q_\ell + q^T_\ell) - \Gamma''' h^\Gamma_\ell + q'''_{I_\ell} + Q'''_{w\ell} + (\alpha_\ell + \alpha_e)\frac{\partial P}{\partial t} + S'''_{e\ell} \tag{3.14}$$

The following terms have been added to the equations to account for sources of mass, momentum and energy as a result of chemical reaction or source boundary conditions:

S'''_{ce} = entrained drop mass source per unit volume

S'''_{cg} = noncondensable mass source per unit volume

$S'''_{c\ell}$ = continuous liquid mass source per unit volume

S'''_{cv} = vapor mass source per unit volume

$S'''_{e\ell}$ = combined liquid energy source per unit volume

S'''_{ev} = vapor/gas mixture energy source per unit volume

S'''_{me} = entrained drop momentum source per unit volume

$S'''_{m\ell}$ = entrained drop momentum source per unit volume

S'''_{mv} = vapor/gas mixture momentum source per unit volume. (3.15)

The use a single energy equation for the combined continuous liquid and liquid droplet fields means that both fields are assumed to be at the same temperature. In regions where both liquid droplets and liquid films are prese this can usually be justified in view of the large rate of mass transfer between the two fields, which will tend to draw both to the same temperature. The use of single momentum and energy equations for the vapor/gas mixture means that the vapor and the noncondensable gas mixture travel at the same velocity and have the same temperature within each computation cell.

Additional mass transport equations are solved to determine the mass of each gas species in the noncondensable gas mixture. If the gas mixture is comprised of N species, then N-1 gas continuity equations are solved for the mass concentrations of N-1 species of the gas mixture. The mass concentration of the Nth species is determined from the expression:

$$\rho_N^{n+1} = \rho_{mg}^{n+1} - \sum_{i=1}^{N-1} \rho_i^{n+1} \tag{3.16}$$

The first N-1 mass transport equations have the same form as the vapor and noncondensable gas mixture mass conservation equations shown in Equation 3.11.

A transport equation for the drop area is solved that accounts for area source due to drop injection and area change due to phase change. The area transport equation is

$$\frac{\partial A'''_{I_d}}{\partial t} + \nabla \cdot (A'''_{I_d} \underline{U}_e) = \frac{6S'''_e}{\rho_\ell D_s} + \frac{2}{3} \frac{A'''_{I_d} \eta \Gamma'''}{\alpha_e \rho_\ell} \tag{3.17}$$

where A'''_{I_d} is the drop surface area per unit volume, S'''_e is the volumetric drop source, and D_s is the diameter of the injected drops.

3.3 Component Form of the Momentum Equations

The momentum equations in COBRA-NC can be solved in the full three-dimensional form shown in Equation 3.12 or in a lumped parameter form where the momentum flux term and the viscous and turbulent shear terms are neglected. The standard version of COBRA-NC, available through the Nuclear Regulatory Commission, solves the three-dimensional momentum equations on a rectangular mesh. For the geometry of the Catawba ice condenser cylindrical coordinates are more appropriate. As part of this modeling effort, a capability to use 2-dimensional generalized coordinates was added to the code. The third dimension is the vertical direction so that the computational mesh is a stack of 2-dimension generalized coordinate grids. The details of the generalized coordinates are described in Section 4.1 in conjunction with the other changes made to the code specifically for these simulations.

3.4 Physical Models

The conservation equations presented in Section 3.2 are solved numerically on a finite-difference mesh made up of numerous computational cells. Closure of the equation set requires physical models for the mass exchange among the three fields at the phase interfaces, the exchange of momentum at the interfaces, the drag forces at solid boundaries, the viscous stress and turbulence terms in the continuous fields, and the entrainment rate. In addition, property relations for water and noncondensable gases are needed. The reader should refer to the code documentation for a complete description of these models.

3.5 Heat Transfer Models

The heat transfer models in COBRA-NC account for the stored energy, heat generation and heat transfer to the surrounding fluid for various types of structural components. All of the heat transfer calculations are performed at the beginning of each time step before the hydrodynamic solution. Heat transfer coefficients based on old time fluid conditions are used to advance the material conduction solution. The resultant heat release rates are explicitly coupled to the hydrodynamic solution as source terms in the fluid energy equations. Although the code is capable of modeling nuclear fuel rods and the associated boiling heat transfer, dryout and quenching, these models are not generally important for containment analysis and will not be discussed here. Rather, this section will concentrate on the important aspects of the heat transfer model for the superheat problem in an ice condenser containment.

The code can model composite conductors with thermal connections to fluid cells on either or both sides of the conductor. The allowable conductor types are shown in Figure 3.1. Wall conductors may be insulated on one side or connect to fluid cells on both sides. Cylindrical conductors can be solid or hollow with fluid connections on both inside and outside surfaces. Heat transfer in these conductors is one dimensional, i.e. perpendicular to the wall or tube surface. The conductors can be made up of layers of various

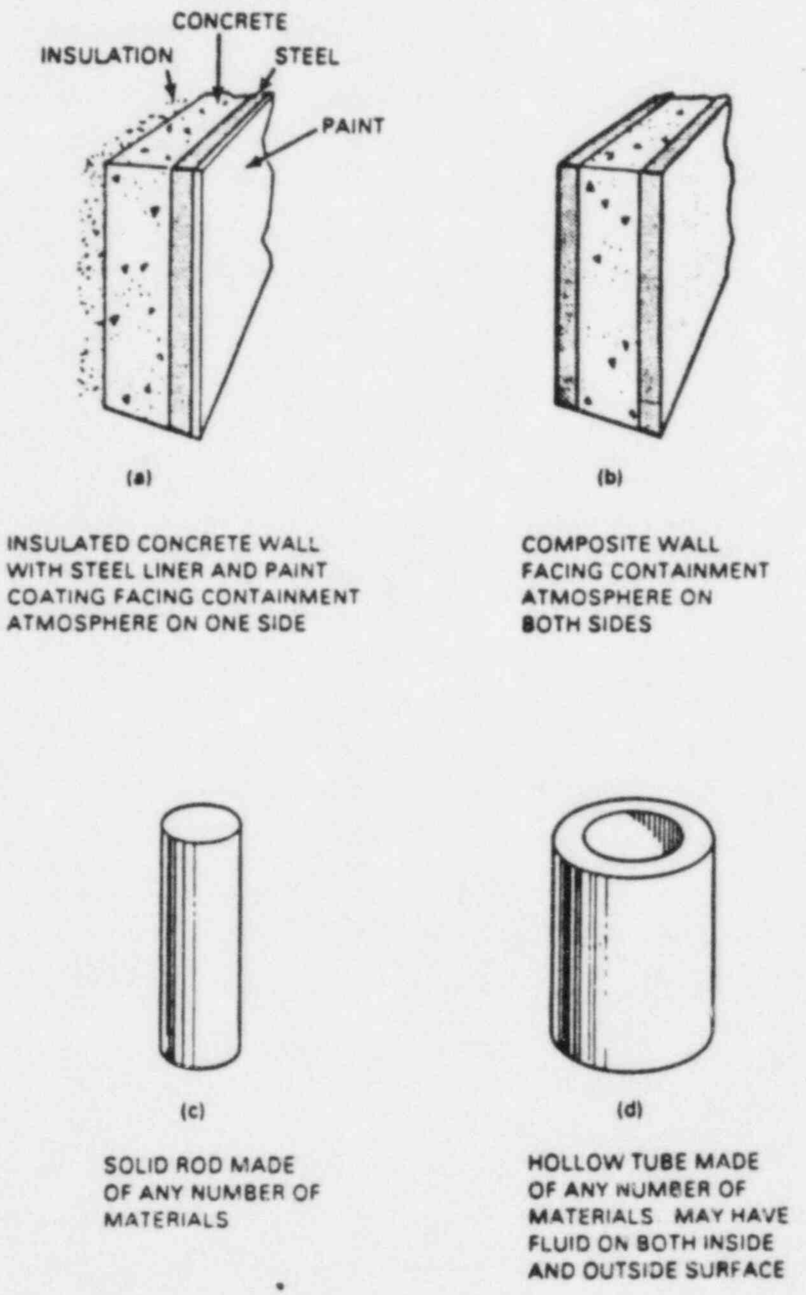

FIGURE 3.1. Available Conduction Types

materials. The one dimensional conduction equation solved for the walls and cylinders is

$$\rho c_p \frac{\partial T}{\partial t} = - \nabla . k \nabla T \tag{3.18}$$

with boundary conditions

$\nabla T = 0$ for insulated surface or solid cylinder centerline

or

$$- A_s k \nabla T = A_v H_v (T_w - T_v) + A_\ell H_\ell (T_w - T_\ell)$$

where A_s is the surface area of the conductor, A_v and A_ℓ are those portions of the surface in contact with vapor and liquid respectively, H_v and H_ℓ are the associated heat transfer coefficients, T_w is the conductor surface temperature and T_v and T_ℓ are the bulk vapor and liquid temperatures.

3.5.1. Wall Heat Transfer

A given fluid cell may be thermally connected to any number of heat transfer surfaces, each haying its own temperature distribution and heat transfer coefficient. The fluid conditions used to calculate the heat transfer coefficients are the same for all heat transfer surfaces connected to the cell. The wall heat transfer logic is formulated so that the heat transfer is to a liquid film or to single phase vapor, or a combination of both during transition as films form or dry out.

For the containment superheat problem the wall heat transfer logic has been specifically designed to allow condensation of steam in the presence of a subcooled surface when the bulk steam temperature is superheated. Because of the different wall types connecting to a single fluid cell, it is possible to arrive at a situation where the fluid temperature is higher than the surface temperature of some walls but lower than that for other connecting walls. This creats a potential heat path from the hot wall to the cold wall through the intermediate temperature fluid. The wall heat transfer logic is formulated to eliminate this possible heat path as described below.

The first step in calculating the wall heat transfer coefficients and heat fluxes is to determine the wettable surface. A conductor surface is defined as wettable if the surface temperature is subcooled and is below the liquid temperature. These are the surfaces that could be covered with a liquid film. Eliminating surfaces with T_w T_ℓ from the film heat transfer regime ensures that all heat is from the liquid to the wall and consequently there is no heat transfer between walls connecting to a common fluid cell.

The fraction of a wettable surface that is covered by a film is a function of the amount of liquid film available in the fluid cell. As the liquid film in the cell disappears the fraction of wetted heat transfer surface area approaches zero. For each wettable surface, the wetted surface area is calculated as

$$A_{wet} = A_{surf} \min \begin{cases} 1. \\ \delta/\delta_{min} \end{cases} \tag{3.19}$$

$$\delta = \frac{V\alpha_\ell}{\sum\limits_{cell} A_{wettable}}$$

where δ_{min} is the minimum allowable film and thickness, V is the cell volume, α_ℓ is the liquid film volume fraction and A_{surf} is the surface area of the conductor associated with the fluid cell. The actual film thickness, δ, is calculated as the film volume in the cell divided by the total wettable heat transfer surface area associated with the cell. The

[

]a,c

$$A_{dry} = A_{surf} - A_{wet} \tag{3.20}$$

On the wet portion of the surface the heat transfer coefficient is calculated assuming the surface is covered with a film of thickness δ. The heat transfer coefficient is given by

$$H_\ell = \max \begin{cases} 3.66 \dfrac{k_\ell}{D_h} \\ .023\, Re_\ell^{.8}\, Pr_\ell^{.4} \dfrac{k_\ell}{D_h} \\ 2.\dfrac{k_\ell}{\delta_e},\ \delta_e = \max \begin{cases} \delta_{min} \\ \delta \end{cases} \end{cases} \tag{3.21}$$

where k_ℓ is the liquid conductively, D_h is the hydraulic diameter, Re_ℓ is the liquid Reynolds number, and Pr_ℓ is the liquid Prandtl number. The heat to the wall f:om the liquid for one surface is computed as

$$Q_{w\ell} = H_\ell A_{wet}\,(T_\ell - T_w) \tag{3.22}$$

where T_ℓ and T_w are the bulk liquid temperature and the wall surface temperature, respectively.

Single phase vapor heat transfer is used for the dry portion of any conductor surface. The surface may be dry for one of two reasons; either there is not sufficient liquid film available to cover the surface, or the wall temperature is greater than the liquid temperature. If the wall temperature is subcooled and less than T_ℓ then condensation is allowed to occur on the surface. The condensation rate is obtained from the Uchida[5, 6] heat transfer correlation and the total heat flux is the sum of convective and condensation components, i.e.

For $T_w < T_\ell$ and $T_w < T_s$

$$Q_w = A_{dry} H_v (T_v - T_s) + A_{dry} H_U (T_s - T_w) \tag{3.23}$$

where H_v is the convective heat transfer coefficient, H_U is the Uchida heat transfer coefficient and T_s is the saturation temperature at the steam partial pressure.

The Uchida correlation is based on experimental data for condensation of saturated steam. The correlation has been used in the COBRA-NC code to model various experiments that included the condensation of saturated steam. The comparisons with data for these simulations is generally good as documented in the COBRA-NC manuals.(3) The condensation heat transfer is based on the temperature difference $T_s - T_w$ and, therefore, does not depend directly on the vapor superheat. [

] a,c

$$H_v = \max \begin{cases} 3.66\ k_{vg}/D_h \\ .023\ Re_{vg}^{.8}\ Pr_{vg}^{.4} \dfrac{k_{vg}}{D_h} \\ [\qquad\qquad]^{a,c} \end{cases} \tag{3.24}$$

$$H_U = \max \begin{cases} \min \begin{cases} 280. \\ 79.33\ (\rho_v/\rho_g)^{.8} \end{cases} \\ H_v \end{cases} \tag{3.25}$$

where k_{vg}, Re_{vg}, Pr_{vg} are the conductivity, Reynold's number, and Prandtl number for the steam/air mixture, ρ_v is the steam density and ρ_g is the air density.[

]a,c

The condensation rate consistent with the condensation heat transfer is given by

$$\Gamma_U = \frac{H_U\ (T_s - T_w)}{h_v - h_f} \tag{3.26}$$

The condensate leaves the vapor at h_v and enters the liquid at h_f with the heat of vaporization going to the wall. The vapor and liquid heat sink terms are therefore given by

$$\begin{aligned} Q_{wv} &= H_v(T_v - T_s) + \Gamma_U h_v \\ Q_{w\ell} &= - \Gamma_U h_f \end{aligned} \tag{3.27}$$

There are corresponding ma source terms for the vapor and the liquid film given by

$$M_{sv} = - \Gamma_U$$
$$M_{s\ell} = \Gamma_U \tag{3.28}$$

The COBRA-NC code has a heat transfer package that includes coefficients for the full range of flow regimes. The COBRA-NC documentation should be consulted for information on the wall heat transfer logic not covered here.

3.5.2 Interfacial Heat and Mass Transfer

The interfacial heat transfer package in COBRA-NC accounts for heat transfer between each of the phases across the phase interfaces. The interfacial heat transfer is divided into four parts; subcooled liquid, superheated liquid, subcooled vapor, and superheated vapor. The heat transfer coefficients for each component are calculated individually and the interfacial heat transfer is calculated with the assumption that the interface is at T_s. The heat components can be written as

$$Q_{scl} = A_I H_{scl} (T_\ell - T_s)$$

$$Q_{shl} = A_I H_{shl} (T_\ell - T_s)$$

$$Q_{scv} = A_I H_{scv} (T_v - T_s)$$

$$Q_{shv} = A_I H_{shv} (T_v - T_s)$$

Since there can be no mass or energy storage at the interface, the heat to or from the interface must be balanced by an appropriate change of phase. Since each of the heat components above are independent of the others, an energy balance at the interface must hold for each component. This gives

$$Q_{scl} = \Gamma_{scl} (h_v - h_f)$$

$$Q_{shl} = \Gamma_{shl} (h_g - h_\ell)$$

$$Q_{scv} = \Gamma_{scv} (h_v - h_f)$$

$$Q_{shv} = \Gamma_{shv} (h_g - h_\ell) \tag{3.30}$$

where Γ_{scl}, Γ_{shl}, Γ_{scv} and Γ_{shv} are the phase change rates associated with the four components of the interfacial heat transfer. The enthalpy jumps used are $(h_v - h_g)$ and $(h_g - h_\ell)$ rather than h_{fg}. This is because some of the heat to the interface from one phase must be used to bring a portion of the other phase to saturation before the phase change can be accomplished.

The net rate of phase change is given by

$$\Gamma = \Gamma_{scl} + \Gamma_{shl} + \Gamma_{scv} + \Gamma_{shv} \tag{3.31}$$

The interfacial area and heat transfer coefficients depend on the flow regime dictated by the wall temperature and fluid conditions. In this report only the film/drop flow regime is considered. Details concerning other flow regimes are available in the COBRA-NC documentation. In the film/drop regime, the total heat transfer coefficient is given as the sum of drop and film heat transfer coefficient, i.e.

$$A_I H_{scl} = A_{I_d} H_{scl_d} + A_{I_f} H_{scl_f}$$

$$A_I H_{shl} = A_{I_d} H_{shl_d} + A_{I_f} H_{scl_f}$$

$$A_I H_{scv} = A_{I_d} H_{shv_d} + A_{I_f} H_{scv_f}$$

$$A_I H_{shv} = A_{I_d} H_{scv_d} + A_{I_f} H_{shv_f} \tag{3.32}$$

where the d and f subscripts refer to drops and film, respectively.

The drop interfacial area is calculated using the volumetric drop area obtained from the solution of the drop area transport equation discussed in Section 3.2. Thus,

$$A_{I_d} = V\ A''' \tag{3.33}$$

where V is the cell volume.

The film interfacial area is the total wetted surface area in the fluid. To be consistent with the wall heat transfer model A_{I_f} is calculated as

$$A_{I_f} = \sum_{\substack{\text{Heat Transfer Surfaces} \\ \text{Connecting to Cell}}} A_{wet} \tag{3.34}$$

The heat transfer coefficients used for the various interfacial heat components are listed below.

$$H_{scl_d} = 0. \tag{3.35}$$

$$H_{schl_d} = 17.76\ \frac{K_\ell}{D_d} \tag{3.36}$$

$$H_{scv_d} = H_{shv_d} = (2.0 + 0.74\ Re_{vg}^{.5} Pr_{vg}^{.333})\ k_\ell / D_d \tag{3.37}$$

$$H_{scl_f} = 2.0 \text{ Max} \begin{cases} 18. \\ \min \begin{cases} 280. \\ 79.33 \left(\frac{\rho_v}{\rho_g}\right)^{.8} \text{ Btu/hr-ft}^2\text{-°F} \end{cases} \end{cases} \tag{3.38}$$

$$H_{shl_f} = 1. \times 10^6 \quad \text{Btu/hr-ft}^2\text{-°F} \tag{3.39}$$

$$H_{scv_f} = H_{shv_f} = \text{Max} \begin{cases} 0.5 f_I \rho_{vg} c_{p_{vg}} \left| U_v - U_\ell \right| Pr_{vg}^{-2/3} \\ \left[\qquad \qquad \qquad \right]^{a,c} \end{cases} \tag{3.40}$$

$$f_I = 0.005 \, (1.0 + 75.0 \alpha_\ell) \tag{3.41}$$

There are two departures from the documented COBRA-NC heat transfer model in the heat transfer coefficients listed above. For the containment superheat analysis the subcooled liquid heat transfer coefficient for the drops was set zero. The reason for this will be discussed in conjunction with the drain model in Section 4.3. The second difference is in the use of the Uchida correlation for the case of a subcooled liquid film. This was used so that the condensation heat transfer on a subcooled wall would be the same for both film covered and dry subcooled walls. The factor of 2 on the Uchida correlation accounts for the liquid film temperature being midway between T_w and T_s. The subcooled liquid heat component is

$$Q_{scl} = 2\ H_U\ (T_\ell - T_s) \tag{3.42}$$

substituting

$$T_\ell = .5\ (T_w + T_s) \tag{3.43}$$

gives

$$Q_{scl} = H_U\ (T_w - T_s) \tag{3.44}$$

which yields the same condensation heat transfer as a surface at T_w without the film.

4. MODIFICATION TO COBRA-NC FOR ICE CONDENSER CONTAINMENT ANALYSIS

Several modifications were made to COBRA-NC specifically for performing the MSLB transient analysis for an ice condenser containment. [ ]a,c

[ ]a,c

PAGES 44 THRU 114 ARE CONSIDERED PROPRIETARY
IN THEIR ENTIRETY a,c

6 RESULTS AND DISCUSSION

Selected results for the three simulations are presented and discussed in this section. Figures 6.1 through 6.15 show results from Model 1 with the drain flow discarded. Results from Model 2 are shown in Figures 6.16 through 6.23 and results from Model 3 with the finer noding are presented in Figures 6.24 through 6.70.

6.1 Model 1 Results

Figure 6.1 shows the volume weighted average steam/air temperature of the lower containment during the MSLB transient. The outer compartments are not included in this average. The temperature increases rapidly from its initial level of 120°F to about 295°F. During this period , the tubes in the steam generator are still covered and the steam leaving the steam generator is at saturation. At 100 seconds into the transient the tubes begin to uncover and

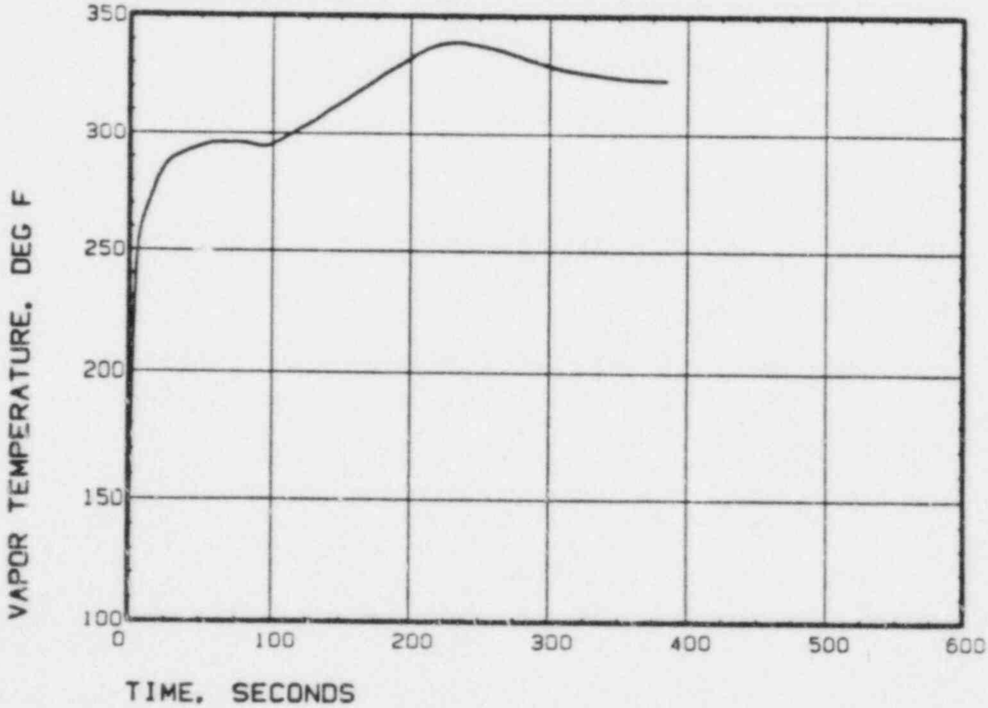

FIGURE 6.1. Model 1 Steam/Air Lower Containment Average Temperature

there is a corresponding increase in the break temperature. The bulk temperature reaches a peak of 337°F at approximately 230 seconds. The break cell temperature does not reach its peak until 300 seconds when it is 350°F. The bulk temperature begins to drop earlier than the break temperature because the vaporization increases as some of the film water accumulates in the lower containment. The transient was not run out all the way to 600 seconds when the deck fans come on since it was apparent that the peak temperature had been reached. The shape of the curve is very similar to those obtained from the LOTIC-III code which does not predict any upturn in temperature after the initial peak. Furthermore, previous runs with slight differences in some of the models were run to about 500 seconds with no upturn in the temperature.

Figures 6.2, 6.3 and 6.4 show the local temperature for three channels in the lower containment. The break is located in channel 31 at level 6, channel 23 is half way around the lower containment, and channel 11 is on the colder side of the containment, directly opposite the break. In general the local temperature curves follow the shape of the bulk temperature. The peak local temperature occurs at the break cell and is 358°F. It should be noted that the local temperatures are average temperatures for the computational cell. There may be some significant temperature distribution within the break cell. The temperature just downstream of the break orifice is likely to be close to the break temperature. For other cells, the surrounding temperature distribution is rather flat and the cell average temperatures are good indicators of the actual local temperatures. The temperature of the level 2 cell in channel 31 drops off fairly rapidly at about 230 seconds. This is the result of condensate films running down the walls and collecting on the floor. In this particular cell the vapor flow is coming in from all sides and going out the top, causing water to build up in the cell to a volume fraction of .02.

Channels 23 and 11 show about the same temperature history with the peak temperature decreasing as we move around the containment. The peak in channel 23 is 350°F and in channel 11, it is 331°F. In channels away from the break where the bouancy force is relatively more significant the peak temperature generally occurs near the top of the lower containment. The temperature dip at

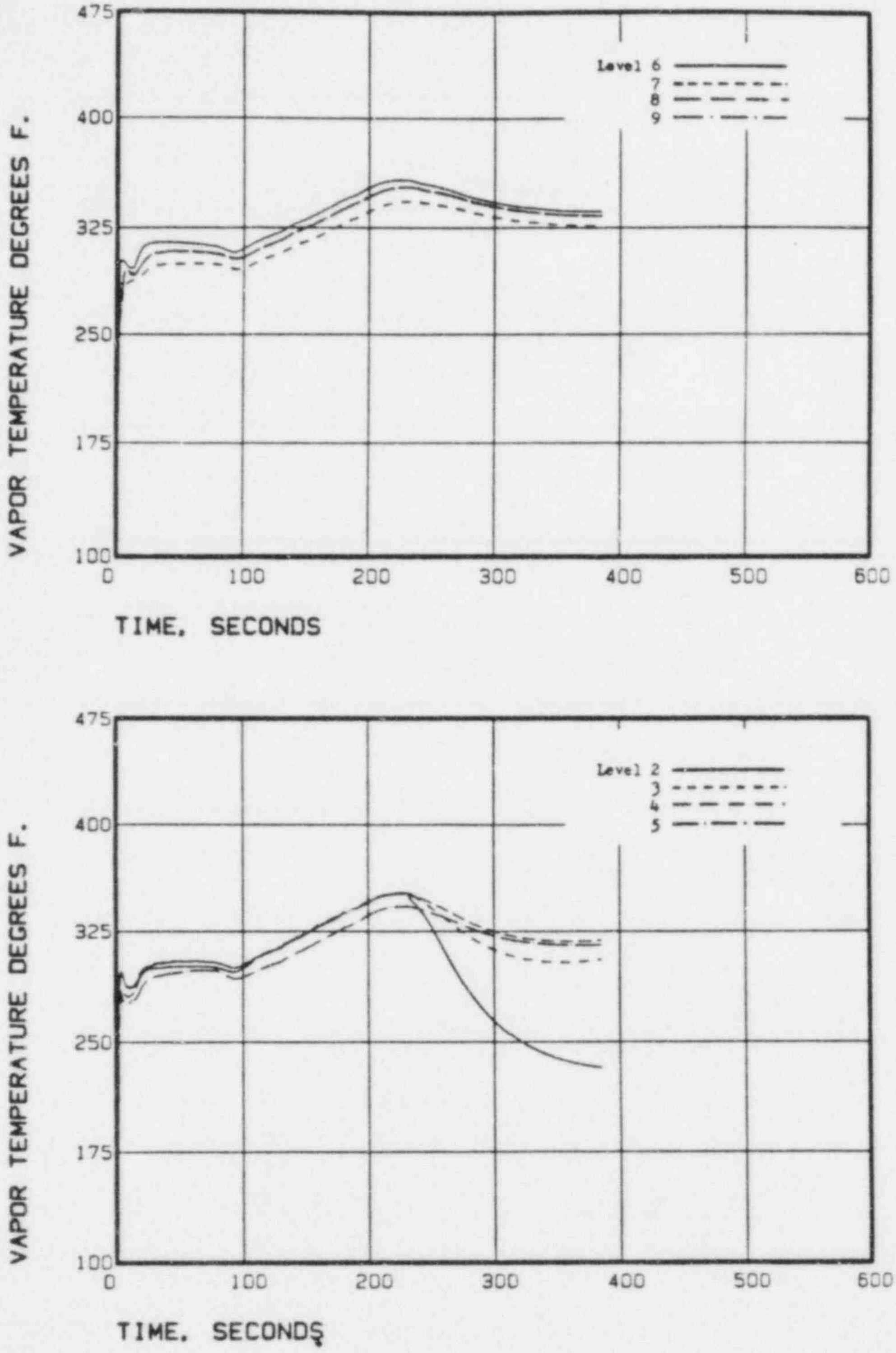

FIGURE 6.2. Model 1 Temperature History In Channel 31

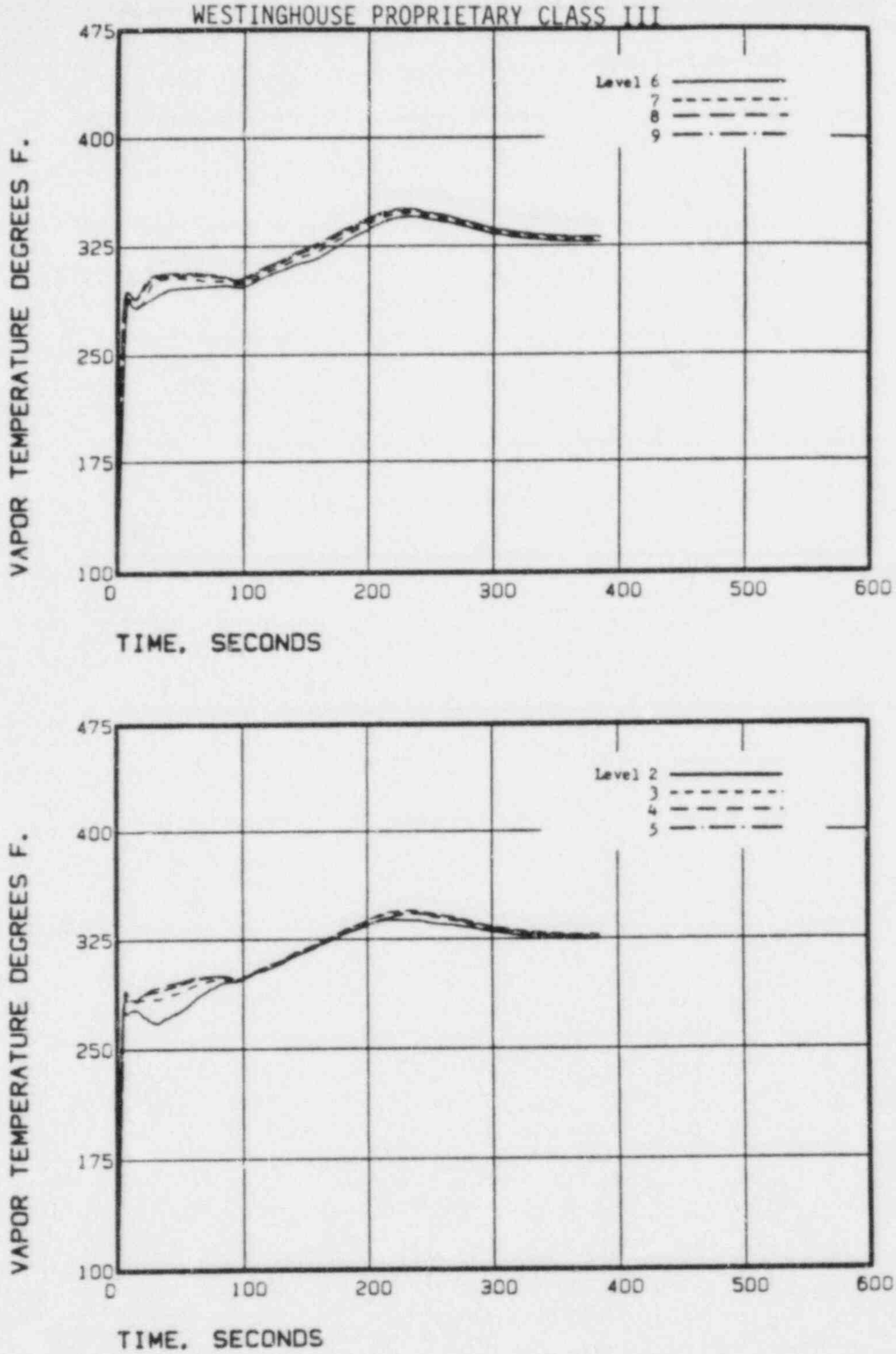

FIGURE 6.3. Model 1 Temperature History in Channel 23

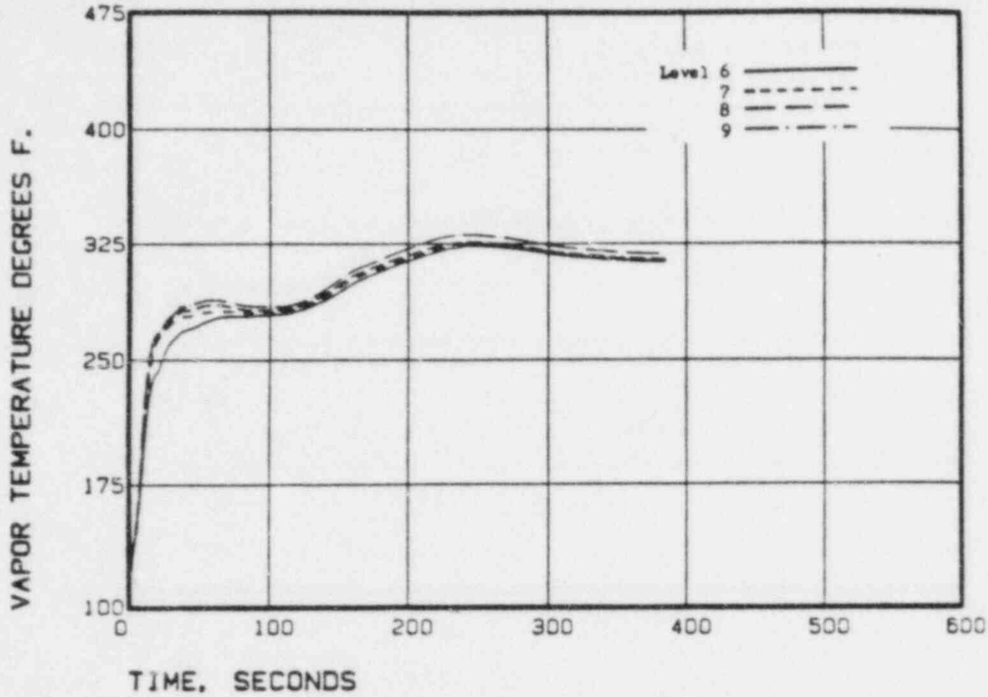

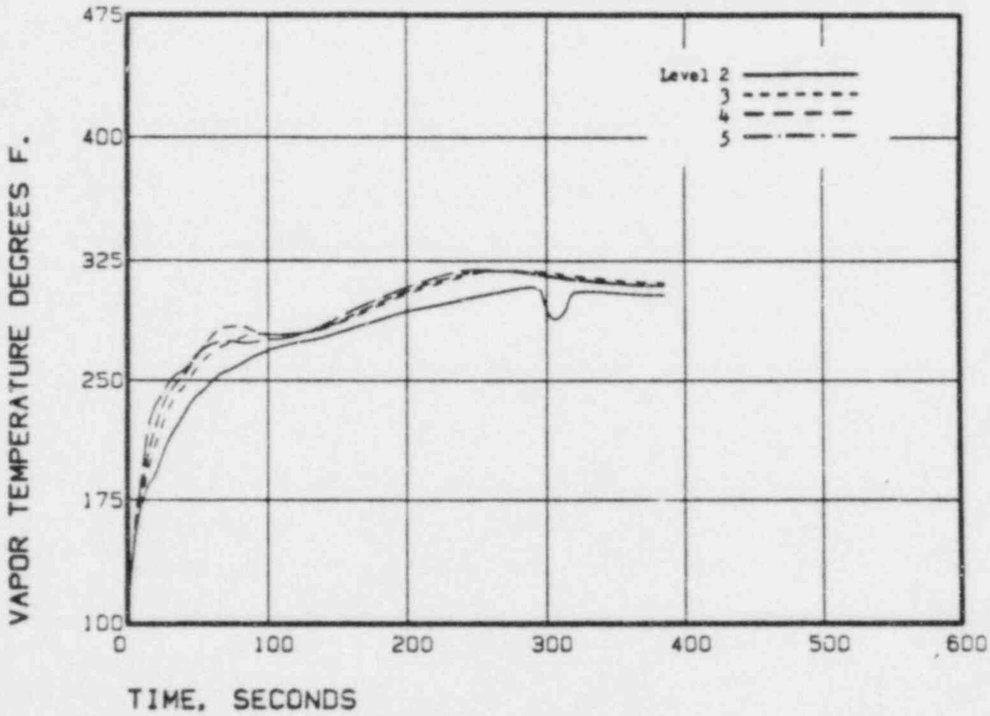

FIGURE 6.4. Model 1 Temperature History in Channel 11

300 seconds at level 2 of channel 11 resulted from an ice condenser door opening and closing causing a change in the flow pattern. Cold vapor from the outer compartment was drawn into the cell. The flow at 300 seconds is going from the bottom of channel, through the pipe tunnel and up into the ice condenser above channel 36.

Figure 6.5 shows temperature contour plots at 300 seconds for the lower containment. The three plots correspond to the three unwrapped radial rings. The first plot is for the ring adjacent to the crane wall followed by the middle ring and the ring next to the biological shield wall. The break location is noted in the outer ring. Because of the averaging required in the contour plotting program, local peaks and valleys may get washed out. This is evident in these plots since the high break cell temperature does not show up. Nevertheless, the plots do give a rather clear picture of the mixing in the lower containment. There is very little axial temperature gradient and the circumferential gradient is limited to about 30°F.

Some typical slab temperatures around the containment are shown in Figures 6.6, 6.7, and 6.8. These curves are for the surface temperatures of three conductor types at level 6 in channels 31, 23, and 11. As can be seen in Figure 6.6, the thin steel dries out within the first 30 seconds of the transient and starts to superheat. The concrete surface temperature remains just below the saturation temperature throughout the transient. The thicker steel dries at about 60 seconds but heats up more slowly than the thinner steel. The same behavior can be observed for the conductors in channels 23 and 11 although the degree of superheating is much less. These results are consistent with Figure 6.9 that shows the total wetted surface area in the lower containment (excluding the outer compartments and the vessel enclosures) as a function of time.

Condensate from the superheated steam quickly raises the wetted surface area from an value of zero to around 43,000 ft.^{2} The thin and thick steel begin to dry out and the wetted surface area tapers off to about 27,000 ft.^{2} This is very close to the amount of concrete surface area in the lower containment. That is, the only surfaces that are condensing and have a liquid film on them

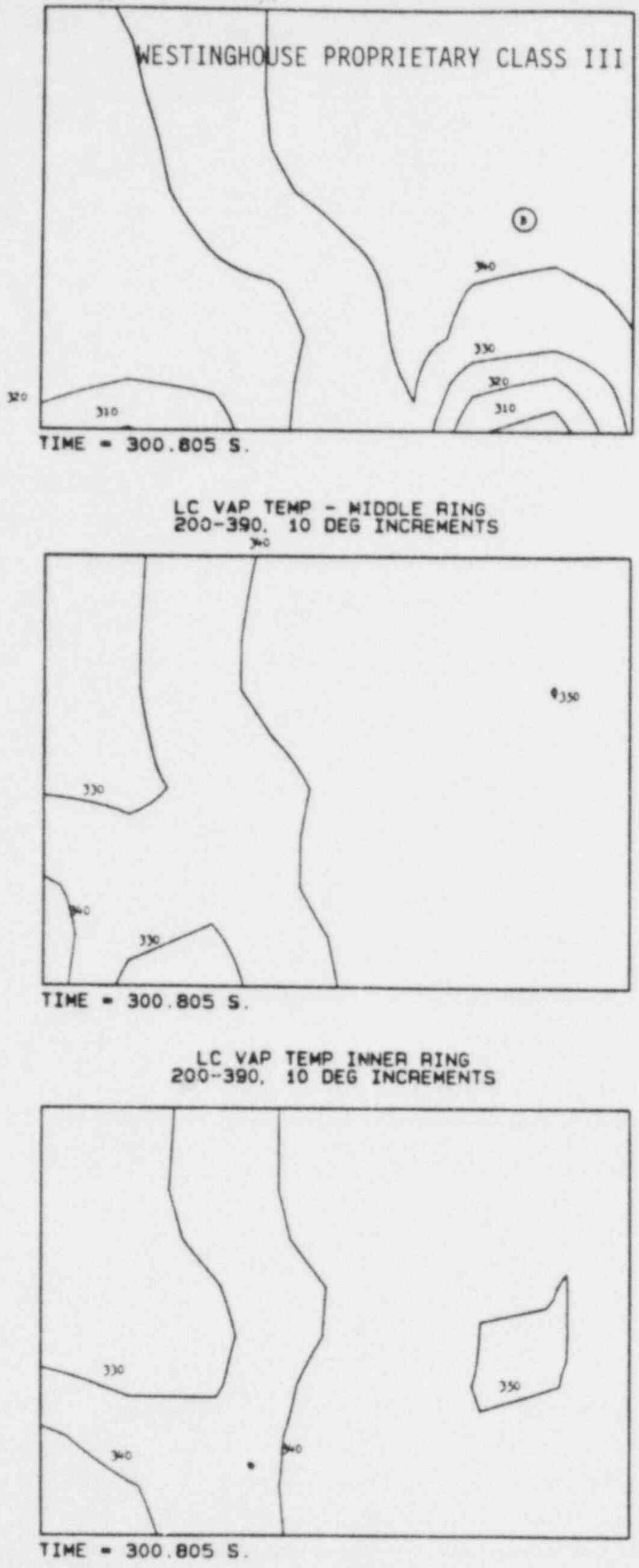

FIGURE 6.5. Model 1 Lower Containment Vapor Temperature Contours at 300 Seconds

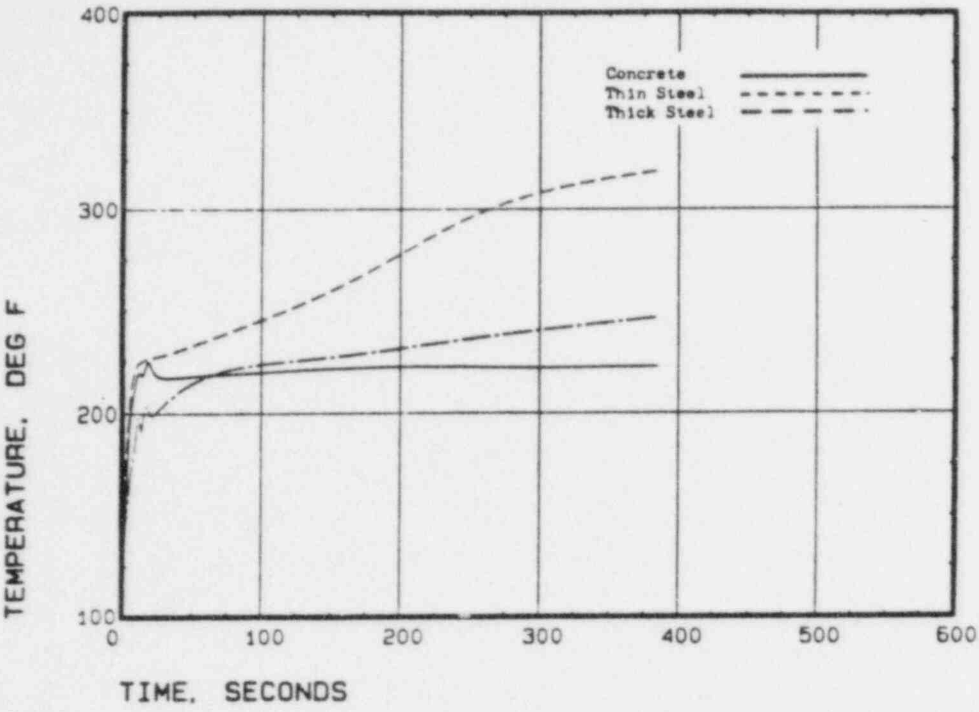

FIGURE 6.6. Model 1 Typical Slab Surface Temperatures, Channel 32, Level 6

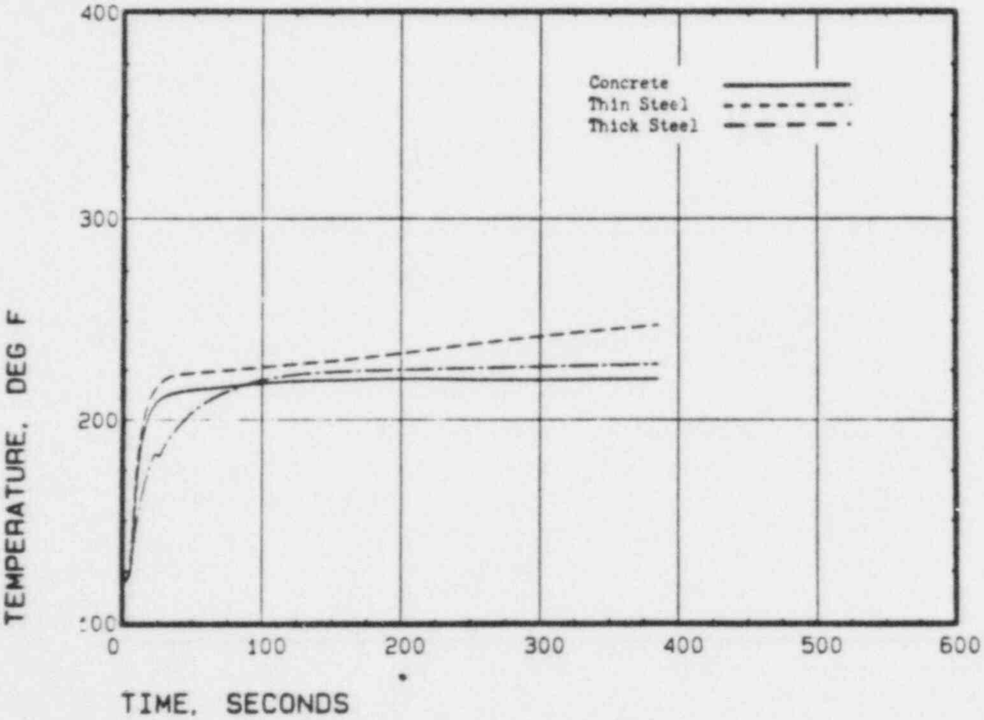

FIGURE 6.7. Model 1 Typical Slab Surface Temperatures, Channel 23, Level 6

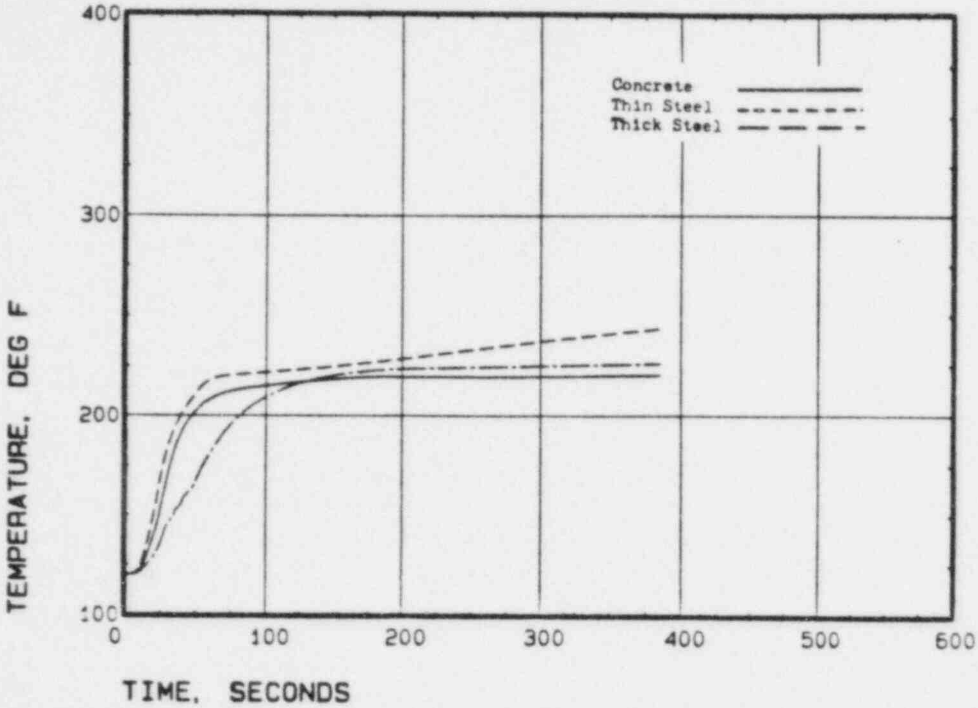

FIGURE 6.8. Model 1 Typical Slab Surface Temperatures, Channel 11, Level 6

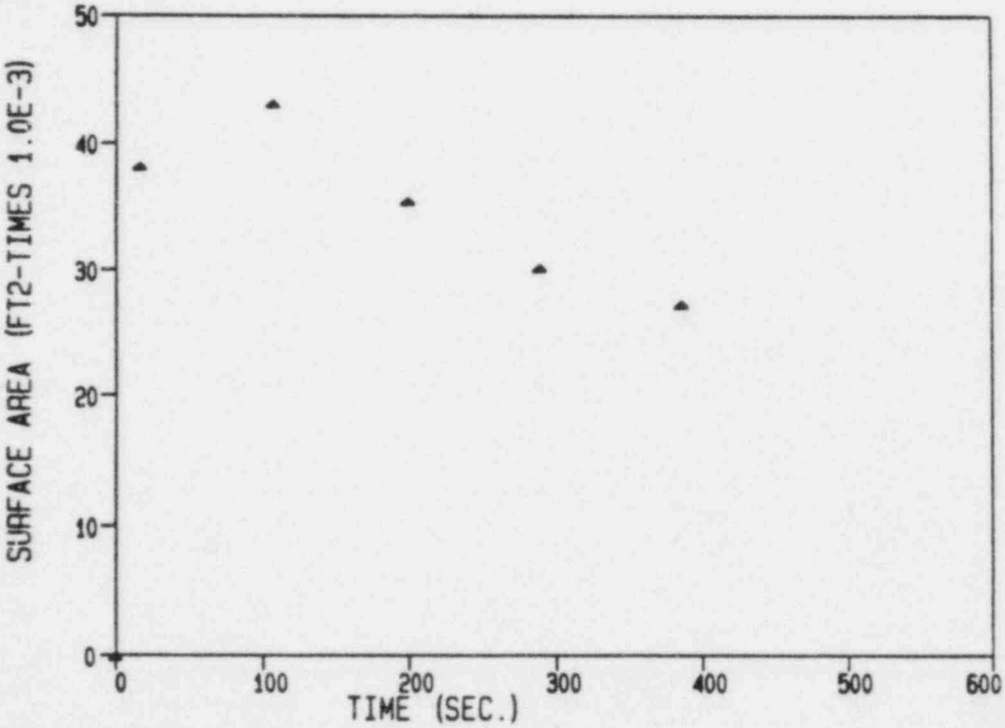

FIGURE 6.9. Model 1 Total Wetted Surface in Lower Containment

during the later part of the transient are the concrete walls, floors and ceilings.

The total condensation and vaporization in the lower containment are of interest because they can be related to the revaporization model used in LOTIC-III. Relevant plots are shown in Figure 6.10 through 6.13. In LOTIC-III, approximately 8.0 percent of the condensate is immediately revaporized and the remaining liquid immediately removed to the sump. As can be seen in Figure 6.10 and 6.11 the cummulative vaporization is much less than 8.0 percent of the cumulative condensation during the first 200 seconds of the transients but reaches nearly 7 percent at the end of the calculation at 380 seconds. Figures 6.12 and 6.13 show the total lower containment condensation and vaporization rate as a function of time. For the first 200 seconds the fraction vaporized is 5 percent or less. The higher steam temperatures and the increased liquid inventory cause the vaporization rate to increase so that at 300 seconds it is about 23 percent of the condensation rate.

Figures 6.14 and 6.15 show some vector plots for the steam/air velocity at 300 seconds. In these plots the arrow length indicates the magnitude of the velocity. The maximum arrow length and its associated velocity are shown at the bottom of each plot. Figure 6.14 shows a cut through the entire containment through the break. On the hot side of the containment the circulation pattern induced by the steam jet is clearly seen. The jet entrains fluid from above and below and even from the outer compartment behind it. It creates a flow down along the containment floor and up through the outer compartments. The circulation pattern on the cold side is not easily seen from this plot alone. Similar vector plots at other times indicate that the flow pattern is not constant on the cold side of the containment, typical of mixed convection flow regimes.

Figure 6.15 shows vector plots for the three computational rings of the lower containment. These plots are arranged from the outermost ring to the innermost ring going from top to bottom. The jet entrainment can be seen in the outer ring. The vector plot is somewhat misleading because of the averaging required to find the cell centered velocities. It appears here that the axial entrainment is much larger than the lateral entrainment. The lateral

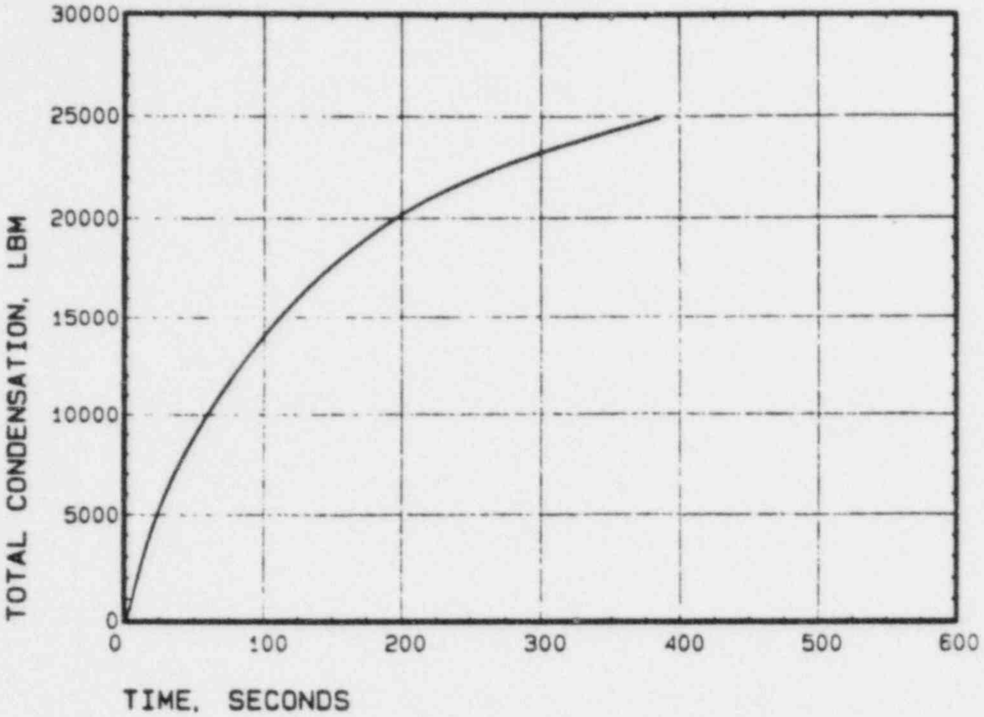

FIGURE 6.10. Model 1 Cumulative Condensation in Lower Containment

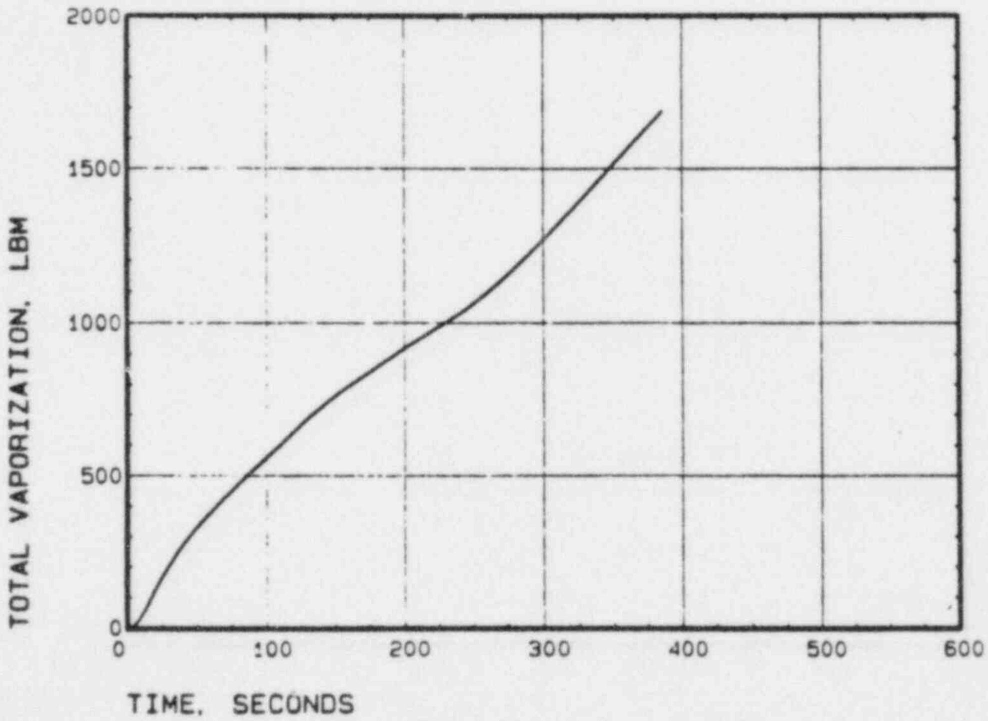

FIGURE 6.11. Model 1 Cumulative Vaporization in Lower Containment

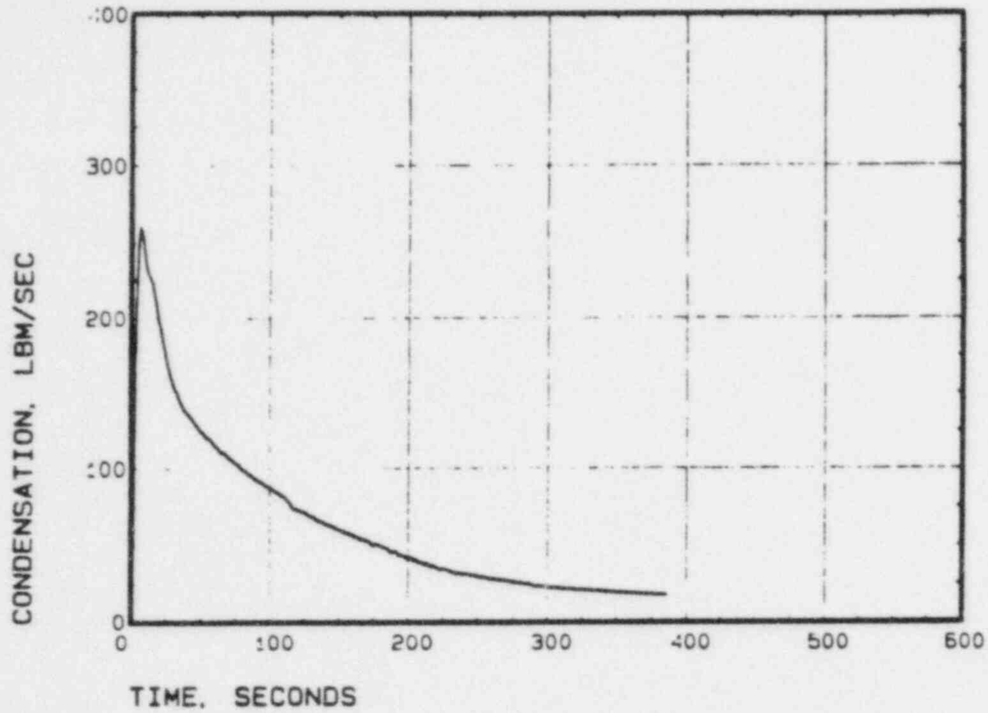

FIGURE 6.12. Model 1 Total Condensation Rate in Lower Containment

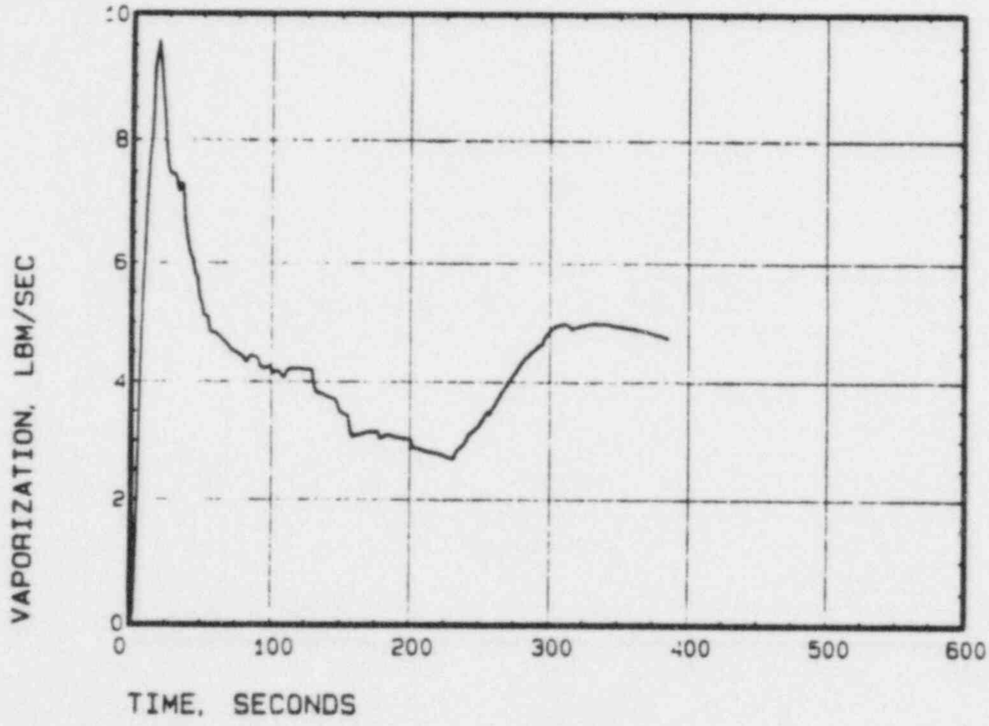

FIGURE 6.13. Model 1 Total Vaporization Rate in Lower Containment

RADIAL CUT THRU BREAK

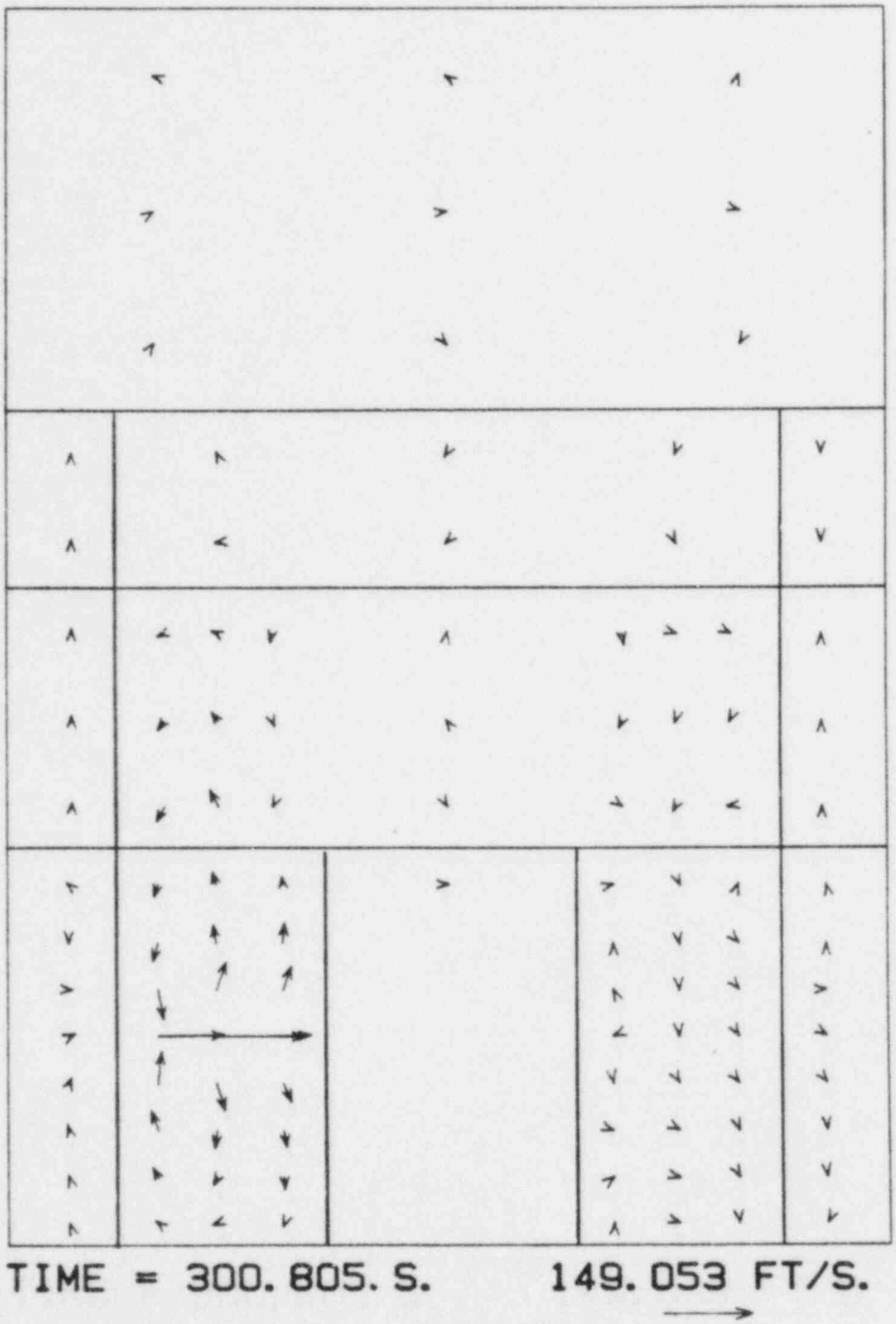

FIGURE 6.14. Model 1 Vapor Lower Containment Vapor Velocity Vectors at 300 Seconds.

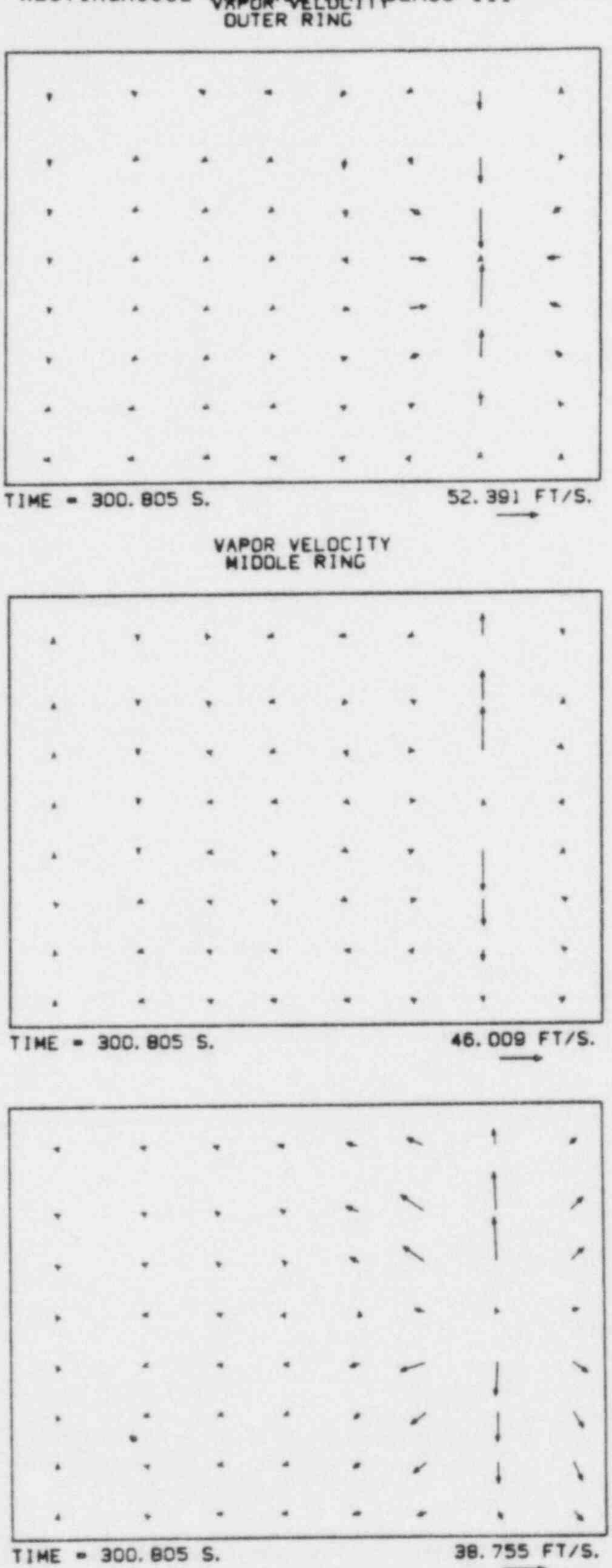

FIGURE 6.15. Model 1 Vapor Velocity Vectors at 300 Seconds

velocities are smaller than the axial velocities because of the high lateral loss coefficients around the steam generators and the cell aspect ratio. The lateral velocities are about 35 ft./sec. compared to 55 ft./sec. for the axial velocities. The center ring shows only axial velocities in the break region because the steam generators on either side block any lateral flow. The bottom plot shows the velocity pattern in the cells adjacent to the biological sheld wall. It is interesting to note that since all the ice condenser doors are at this time closed on the cold side of the containment, the cold side flow is due mainly to steam going all the way around the biological shield wall, down through the pipe tunnel and up through the ice condenser door above channel 36.

6.2 Model 2 Results

Model 2 differed from Model 1 only in that the ice condenser drains flows were injected into the lower containment in Model 2 as described in Section 4.3. Comparing Figure 6.16 for the lower containment bulk vapor temperature to the same results from Model 1, it is observed that the drains flows decreased the peak bulk temperature by 46F to 291F. The peak occurs later in time at about 360 seconds.

Figures 6.17, 6.18 and 6.19 show the local temperature histories in the break channel (31), channel 23, and channel 11. Except for the spike at 275 seconds in the break cell, the peak local temperature is 330F occurring at 230 seconds. The anomolous spike is due to injection of a large number of drops into the break cell for a very short period of time. To accommodate the drain test data, the normal entrainment and de-entrainment models were turned off in COBRA-NC. While this approach worked well in the lower containment, it created some unanticipated behavior in the ice condenser and drain model. Early in the transient, high vapor velocities carried some of the drops up into the ice condenser. Since there was no mechanism for de- entrainment, the drops began to accumulate in the ice condenser, being held up by the high steam flow rate through the few doors that remained open. At 275 seconds into the transient the door located directly above the steam line break closed. The suspended drops fell to the bottom of the ice condenser, de-entrained

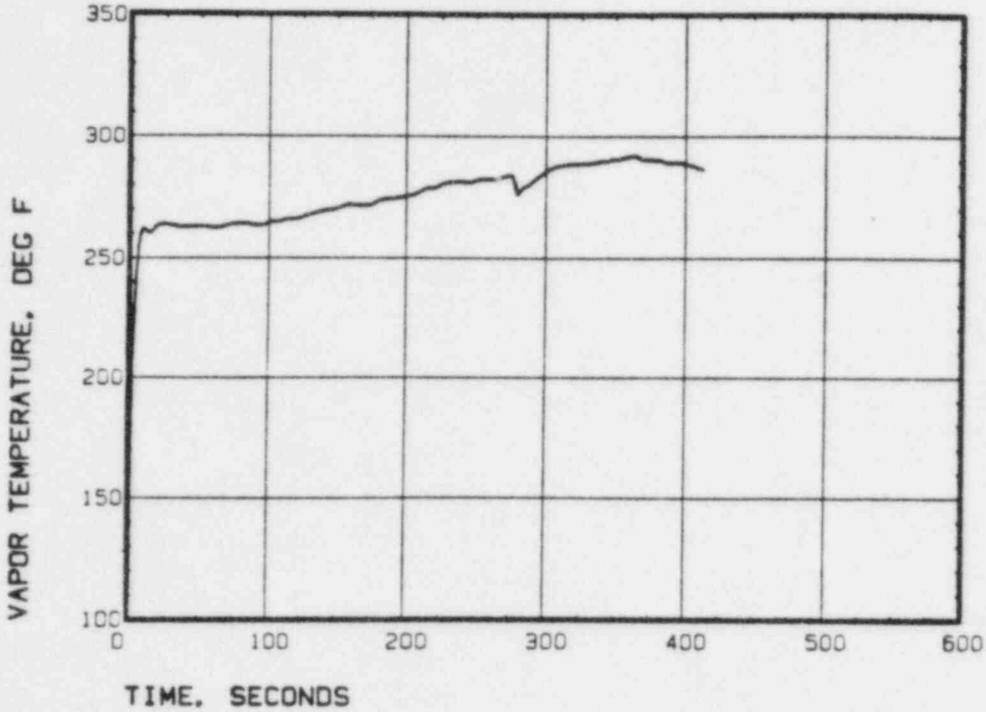

FIGURE 6.16. Model 2 Steam/Air Lower Containment Average Temperature

on the floor and were then included in the drain flow rate. This produced an unphysically high drain flow rate for a brief period and caused a large number of drops to be injected into or near the break cell. The drops rapidly vaporized in the presence of the high jet temperature causing the flow pattern at the jet to be reversed. Rather than entraining flow from all directions, the high vaporization rate caused flow to be out of the cell on all sides of the jet. The high drop injection rate rapidly returned to a normal value but in the time it took for the flow pattern to be reestablished, there was steam entering the cell at nearly 450F with no cooler steam being entrained. Consequently, the cell temperature quickly approached the break temperature. The momentary high vaporization rate created a substantial amount of steam at the saturation temperature showing up as a drop in the bulk temperature as can be seen in Figure 6.16. In summary, the spike observed in the break cell temperature is a numerical anomally caused by the nonphysical treatment of the drop field in the ice condenser had the COBRA-NC de-entrained models been opertive, this effect would not have occurred. From the shapes of the local

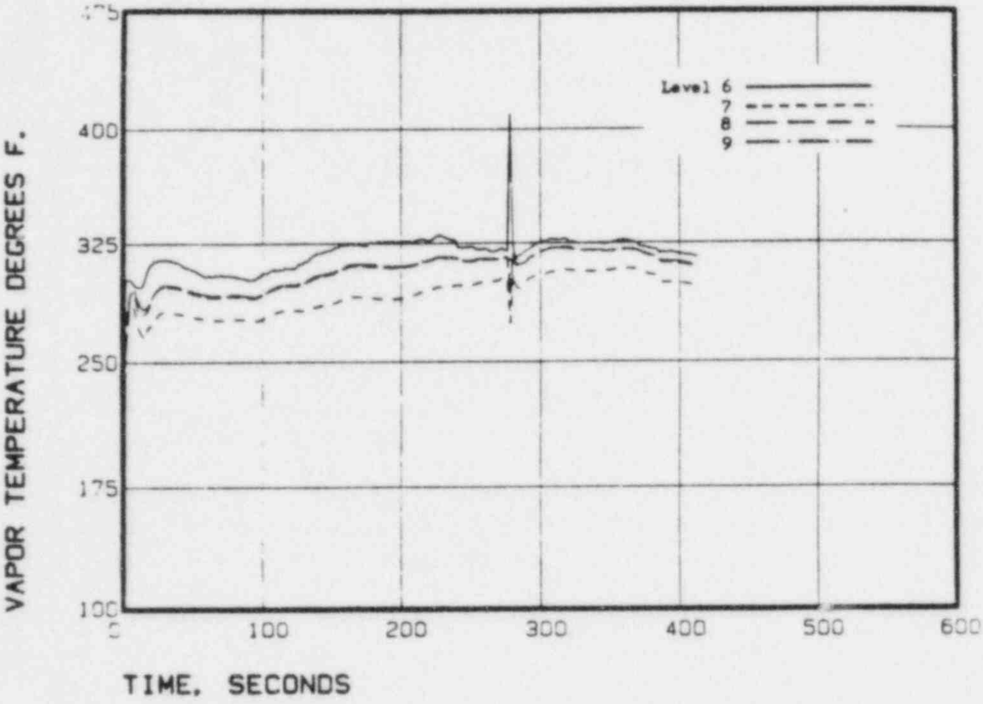

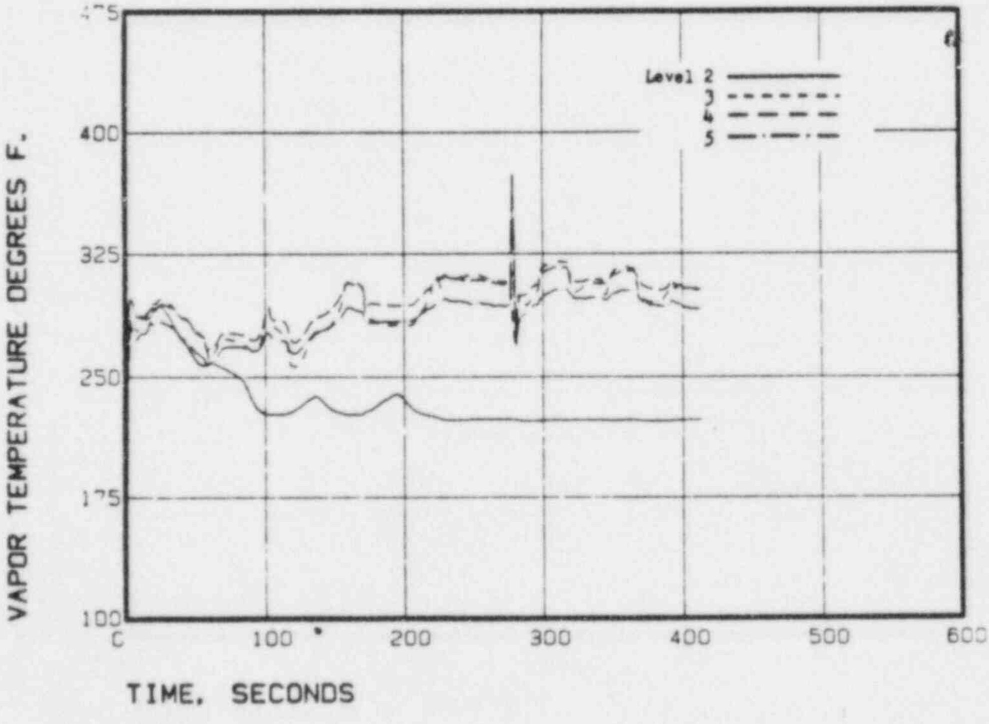

FIGURE 6.17. Model 2 Temperature History in Channel 31

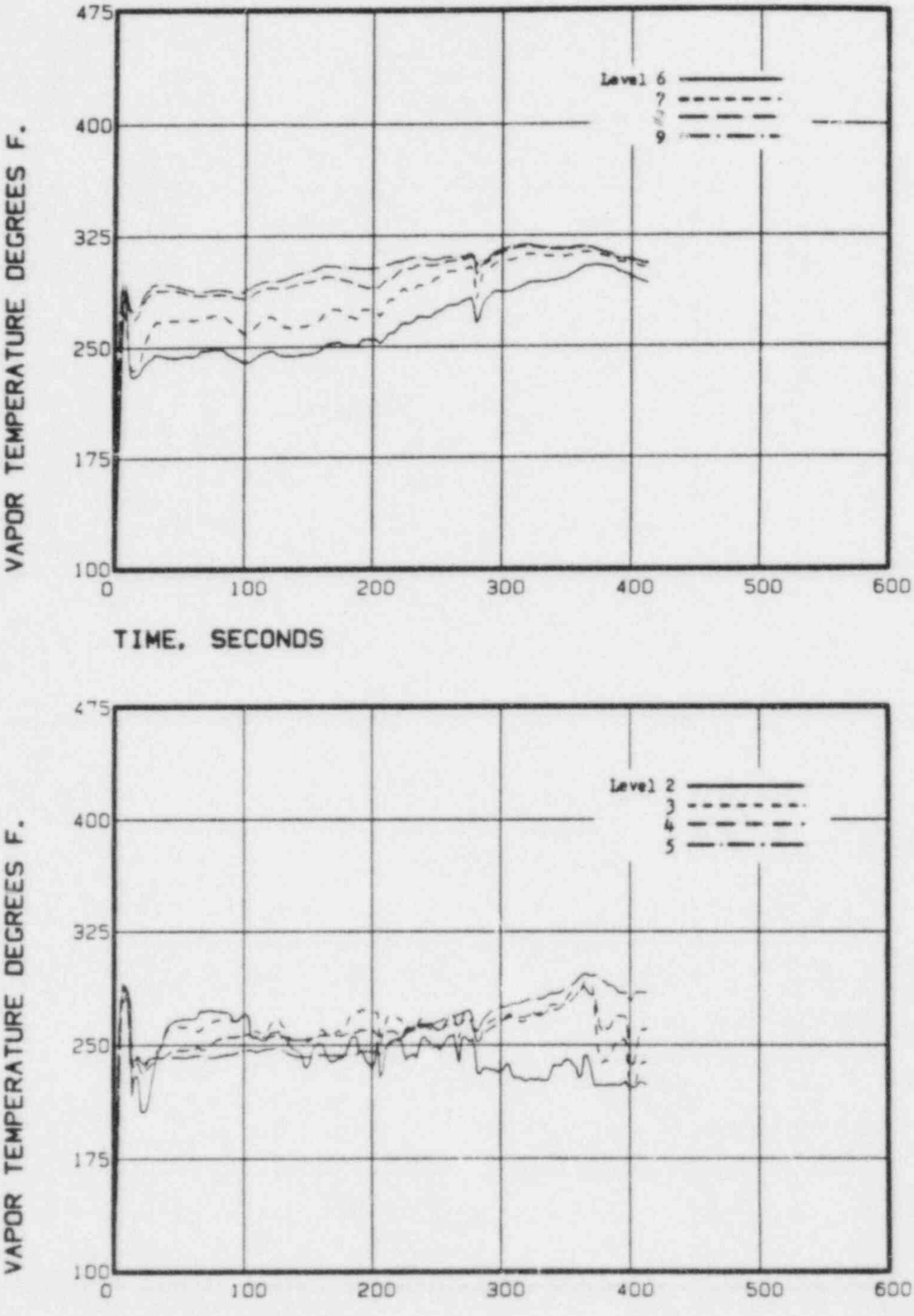

FIGURE 6.18. MODEL 2 Temperature History in Channel 23

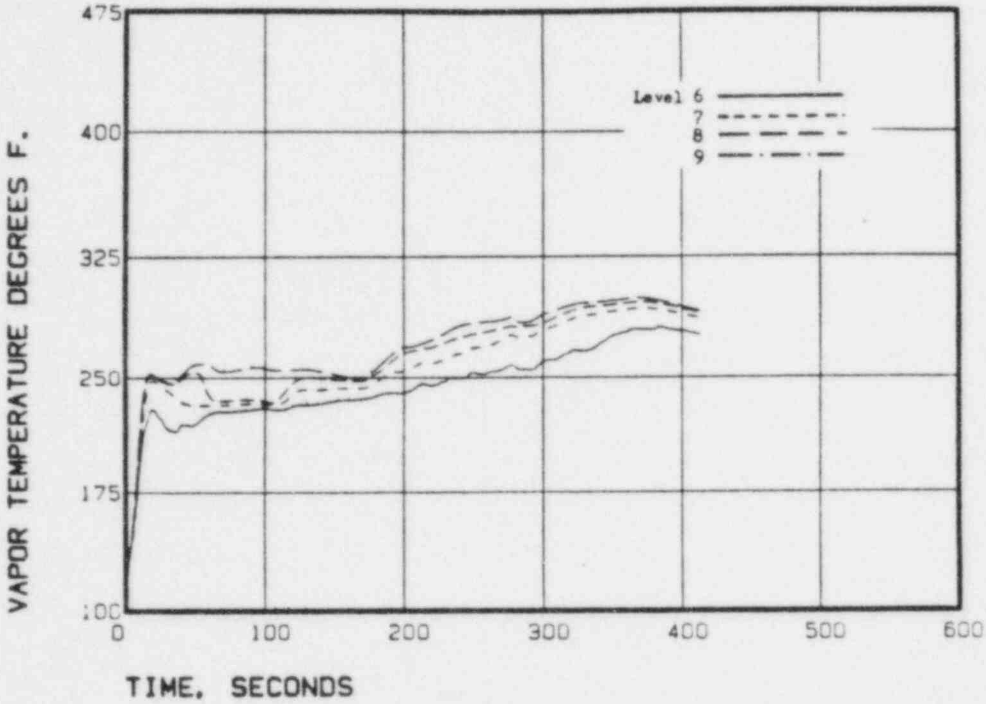

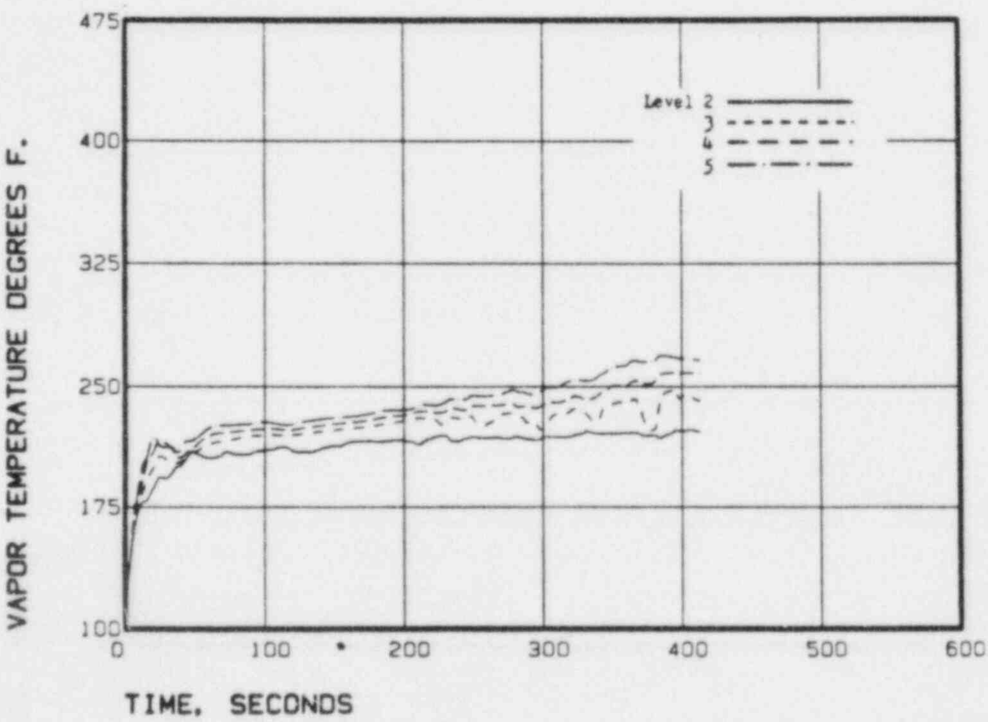

FIGURE 6.19. MODEL 2 Temperature History in Channel 11

and average temperature curves, it is evident that the short excursion did not appreciably influence the transient behavior that followed.

In channels 23 and 11 the peak temperature occurs at the top of the lower containment just as it did in the simulation without drains. The peak temperature at the top of channel 23 is 296°F while in channel 11 it reaches only to 269°F. Apparent in Figures 6.17, 6.18, and 6.19 and the contour plots in Figure 6.20 is the larger axial variation in the temperature as compared to the same results for Model 1. The drops continue to cool the atmosphere as they fall to the containment floor. Also, the drain model injects some drops directly into the lower levels of the lower containment and does not give them a chance to interact directly with the hotter steam at the upper elevations. From the contour plots it can be seen that the degree of mixing around the containment is about the same as for Model 1.

Figures 6.21 and 6.22 show the ice condenser door velocities versus the transient time. The doors represented in Figure 6.21 are for the ice bed sectors above channels 8, 12, 16 & 20 in the lower containment. Figure 6.22 is for the doors associated with channels 24, 28, 32 and 36. Referring to the doors by their associated channel numbers, from Figure 6.21, it can be seen that door 12 closes first followed by doors 8, 16 and 20 in order. Once the doors close, they stay closed except for the brief period at 275 seconds when the rapid drop vaporization at the break forced the doors slightly open. Door 8 remains open longer than door 12 because it receives most of its steam flow from the pipe tunnel and is therefore closer to the break location.

On the hotter side of the containment, door 24 closed at 200 seconds, door 28 above the break closed at about 275 seconds, door 24 never completely closed and door 32 received most of the steam flow during the later parts of the transient. The door closing sequence is consistent with the flow patterns shown in Figures 6.14 and 6.15. Flow goes from the break, around the steam generator, bypassing door 28 and leaving through door 24. On the other side of the break, flow is forced through door 36 because of the presence of the spent fuel storage region wall. Door 32 tends to close because of the low pressure region induced by the jet.

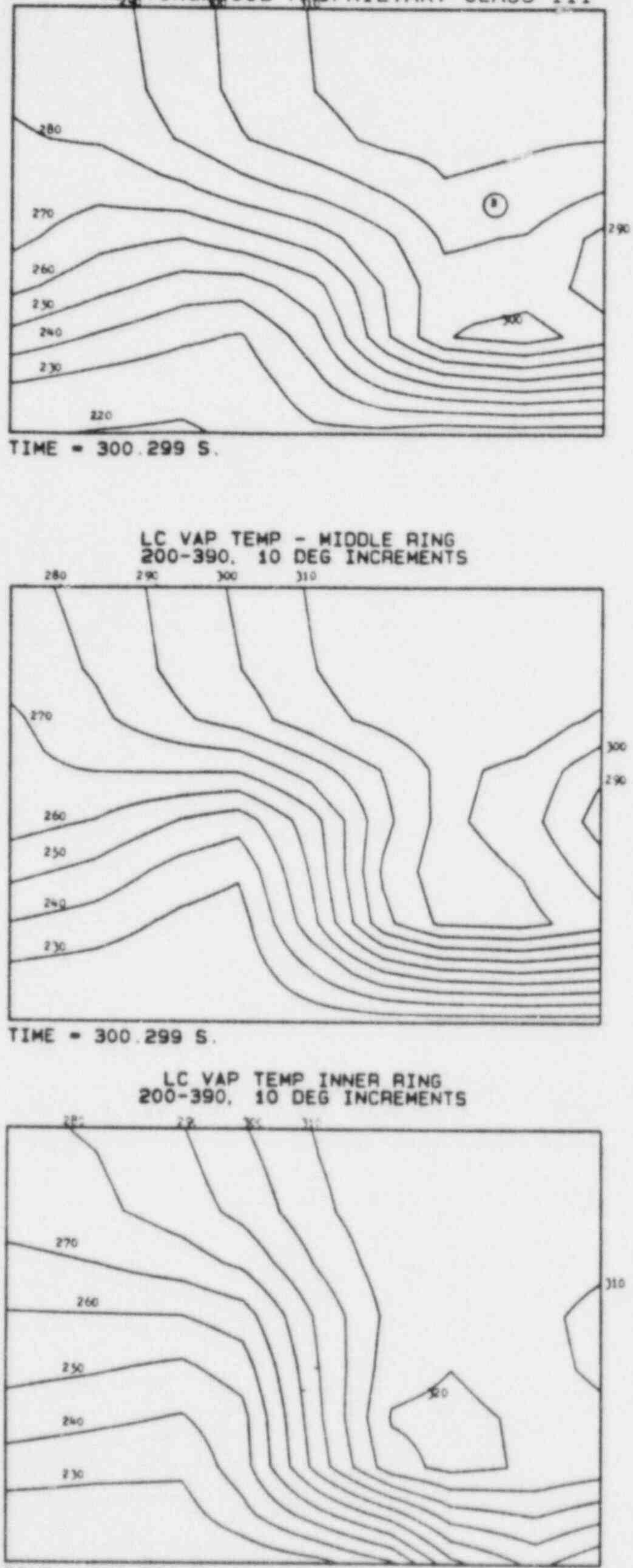

FIGURE 6.20. Model 2 Lower Containment Vapor Temperatures Contours at 300 Seconds

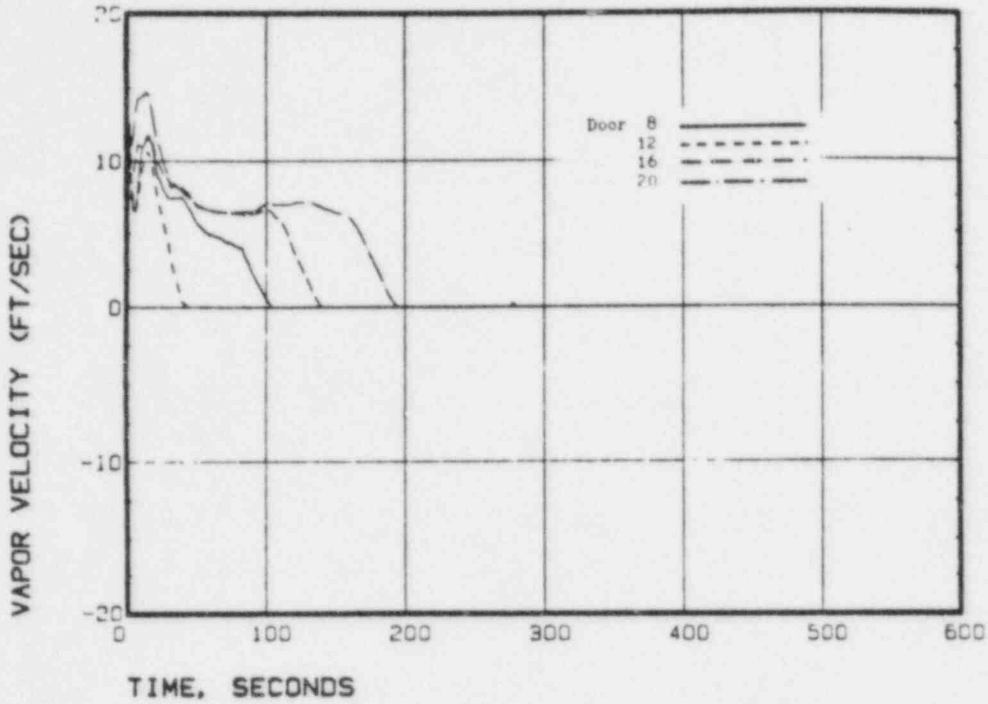

FIGURE 6.21. Model 2 Ice Condenser Door Vapor Velocities Doors 8, 12, 16, and 20.

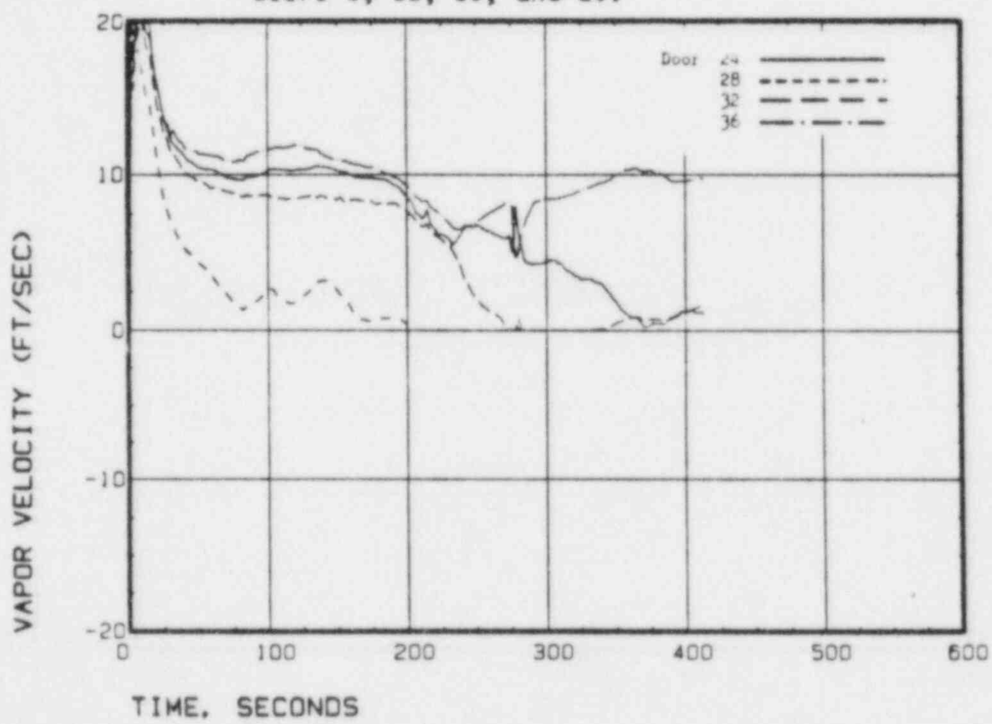

FIGURE 6.22. Model 2 Ice Condenser Door Vapor Velocities Doors 24, ?8, 32 and 36.

6.3 Model 3 Results

Model 3 differs from Model 2 because of the finer noding in the vicinity of the jet and the finer noding in the ice bed and ice condenser doorways. The bulk average temperature history is shown in Figure 6.24. The temperature reaches a peak of 285°F at around 230 seconds and remains fairly steady throughout the rest of the transient. The drop in temperature at 300 seconds is again due to drops collecting in the ice condenser and being dropped into the lower containment as a door closes. The temperature during the first 120 seconds of the transient is somewhat lower and flatter than that for Model 2. The lower temperature results from increased jet entrainment because of the finer noding. At about 120 seconds some of the doors near the break begin closing and the drain flow decreases. The reduced drop entrainment in the jet causes the temperature to rise to a level very close to that obtained with Model 2.

Local temperatures for channels 107, 23 and 11 are presented in Figures 2.25, 6.26 and 6.27. In Model 3 the break is located at level 6 in channel 107. The break cell temperature reaches a peak of 334°F at 200 seconds. This is slightly higher than the break cell peak in Model 2 of 330°F. As the mesh size is reduced, the temperature at the break cell is expected to increase since the jet occupies a greater percentage of the cell volume. The spike at 130 seconds is the result of a door closing near the break. At lower elevations in the same channel there is a small dip in the temperature at the same time resulting from the increased vaporization. In channel 23 the peak temperature is 316°F at 200 seconds and remains at about that level for the remainder of the transient. On the cold side of the containment, the peak temperature attained in channel 11 is 295°F.

Local temperatures in the outer compartments are shown in Figure 6.28 through 6.35. The peak outer compartment is 286 and occurs in channel 16, level 7 at 300 seconds. The temperature at level 8 for some of the channels approaches the initial structure temperature towards the end of the simulation. These cells have very limited communication with the surrounding cells. Some steam was forced into these compartments during the initial stages of blowdown,

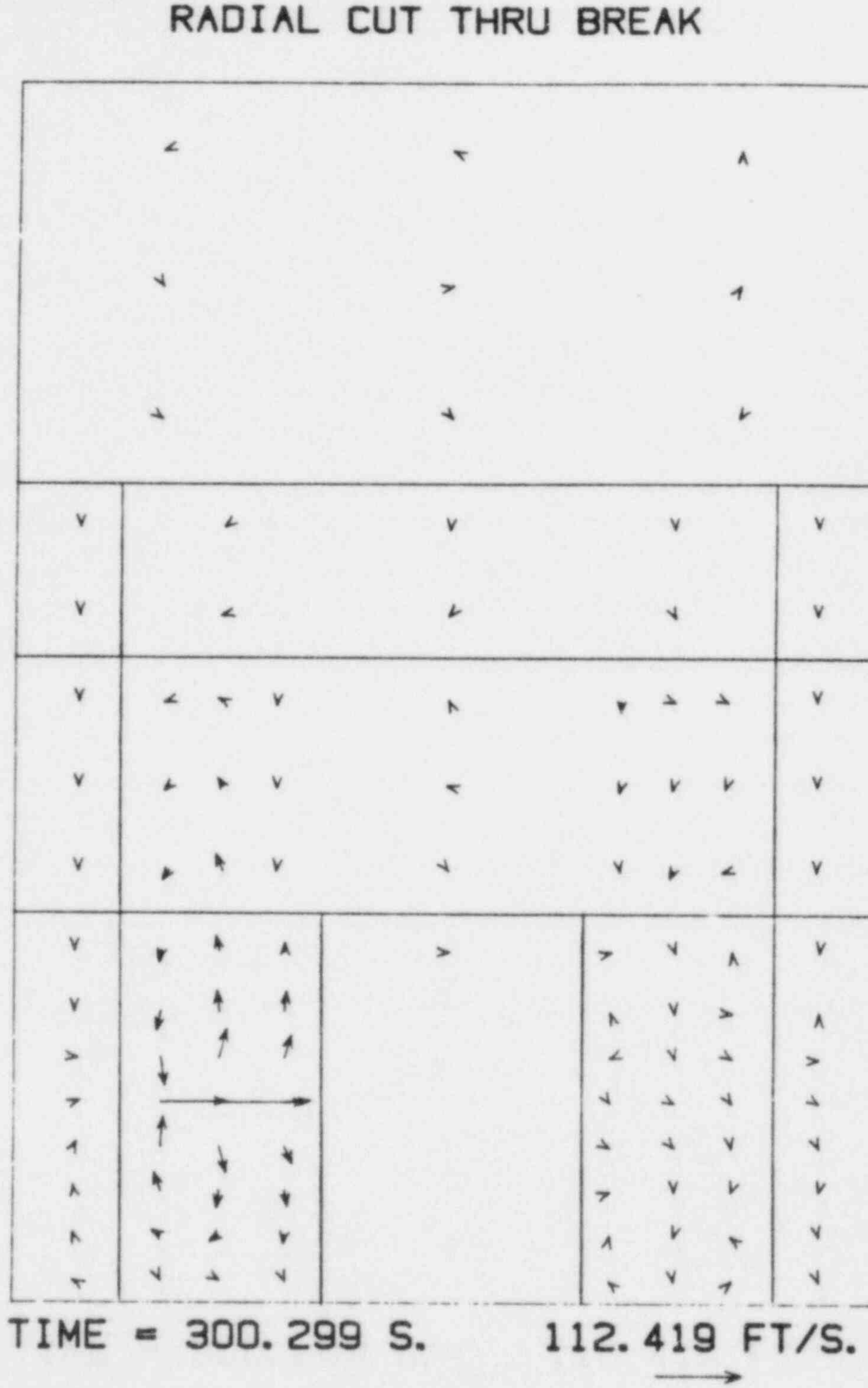

FIGURE 6.23. Model 2 Vapor Velocity Vector at 300 Seconds

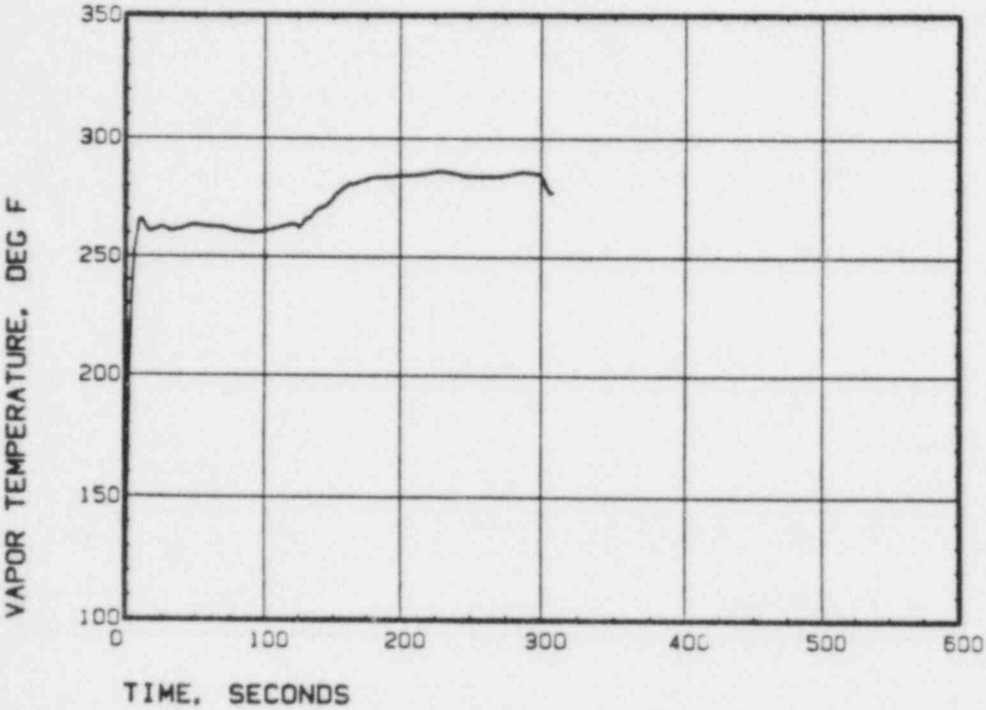

FIGURE 6.24. Model 3 Steam/Air Lower Containment Average Temperature

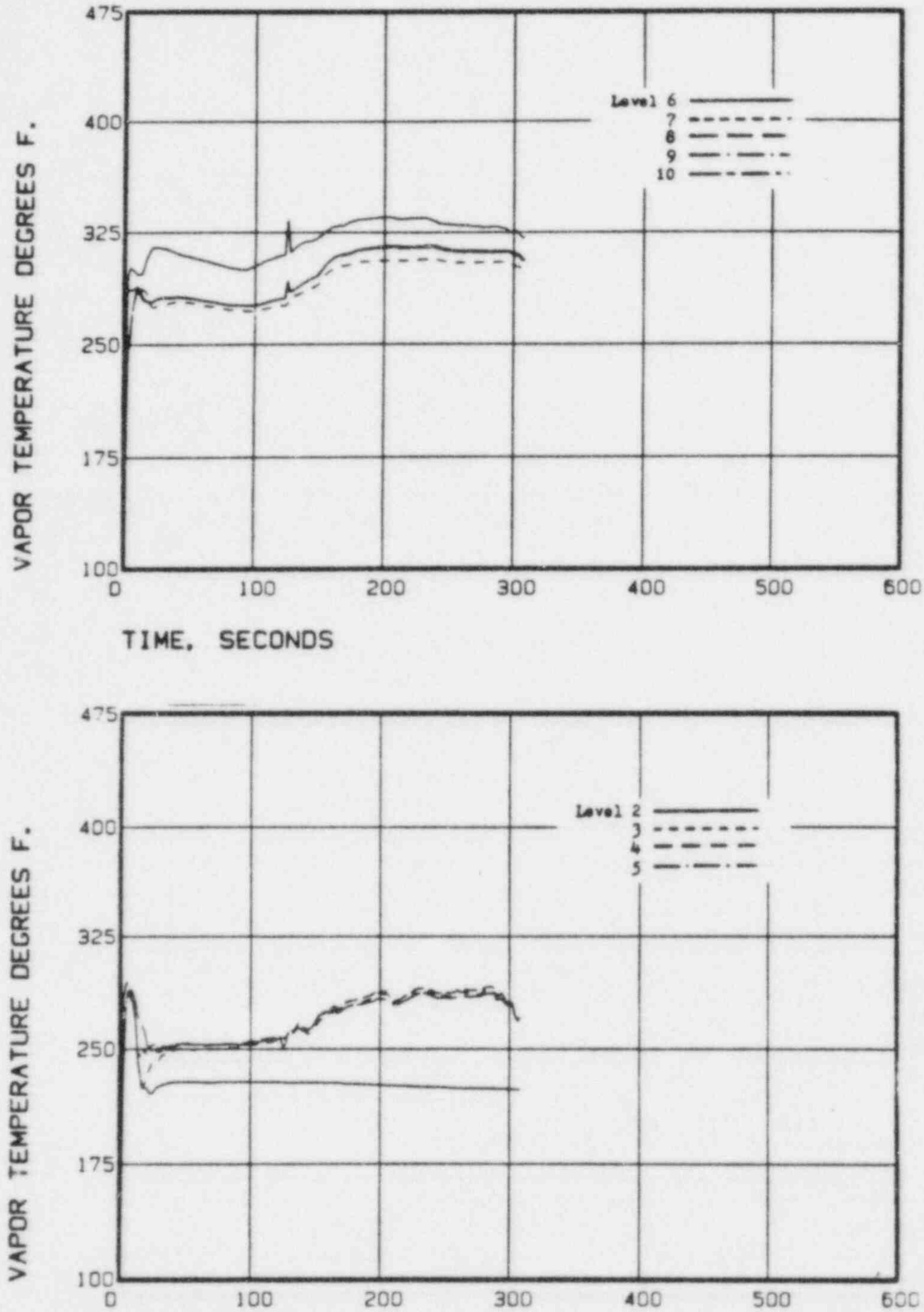

FIGURE 6.25. Model 3 Temperature History in Channel 107

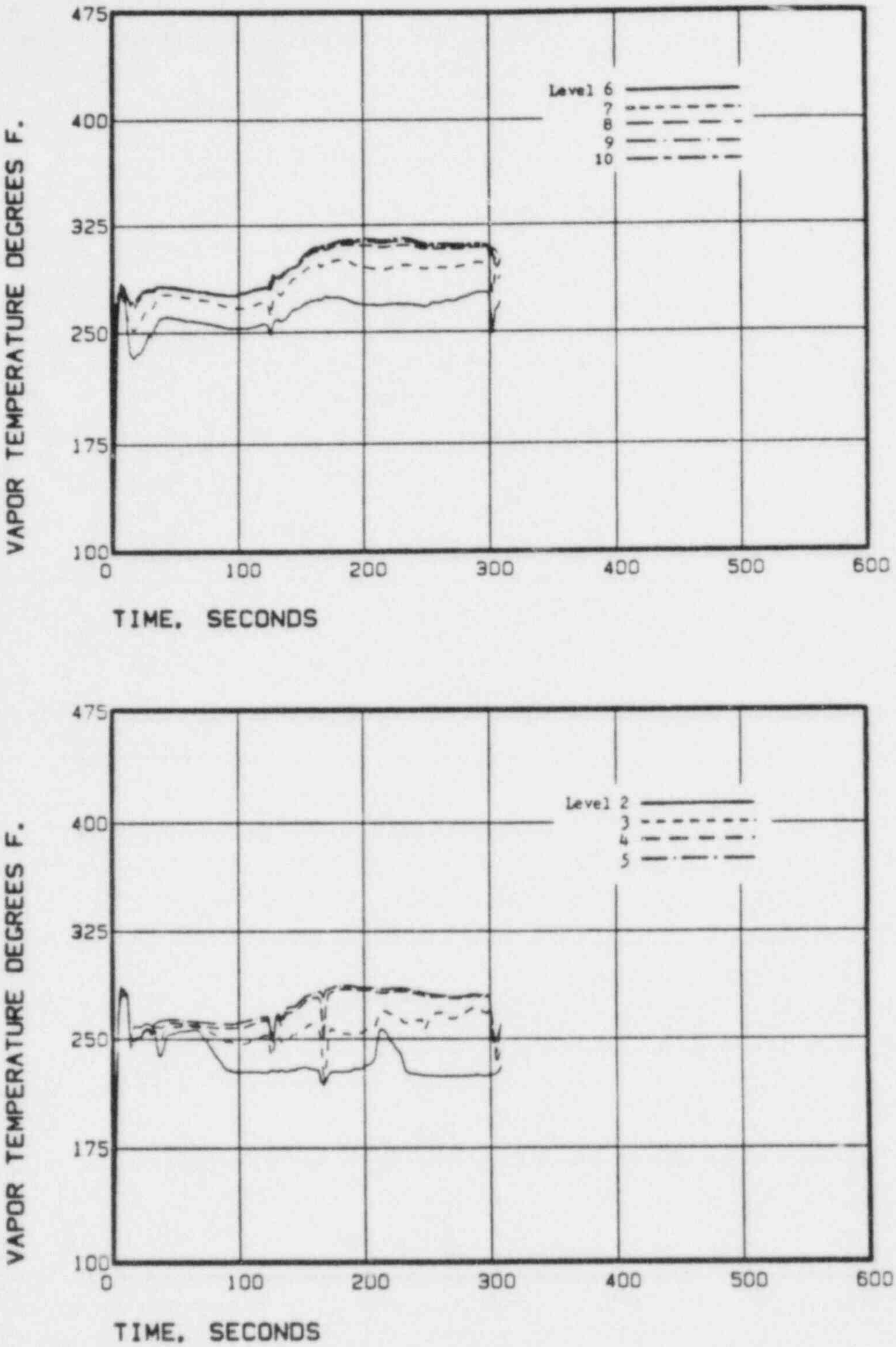

FIGURE 6.26. Model 3 Temperature History in Channel 23

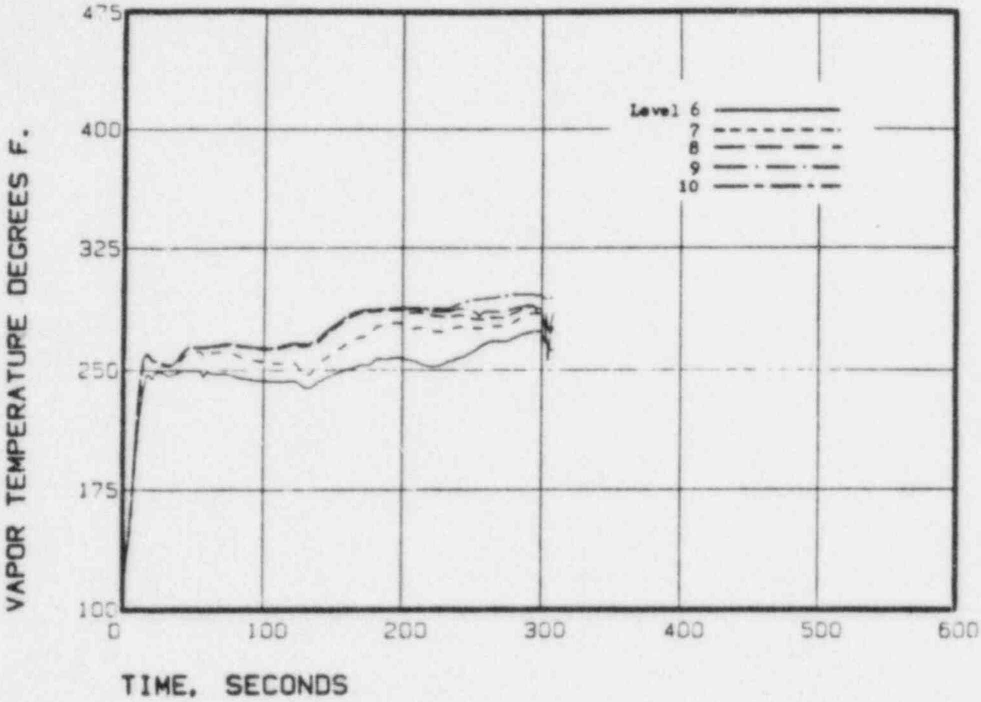

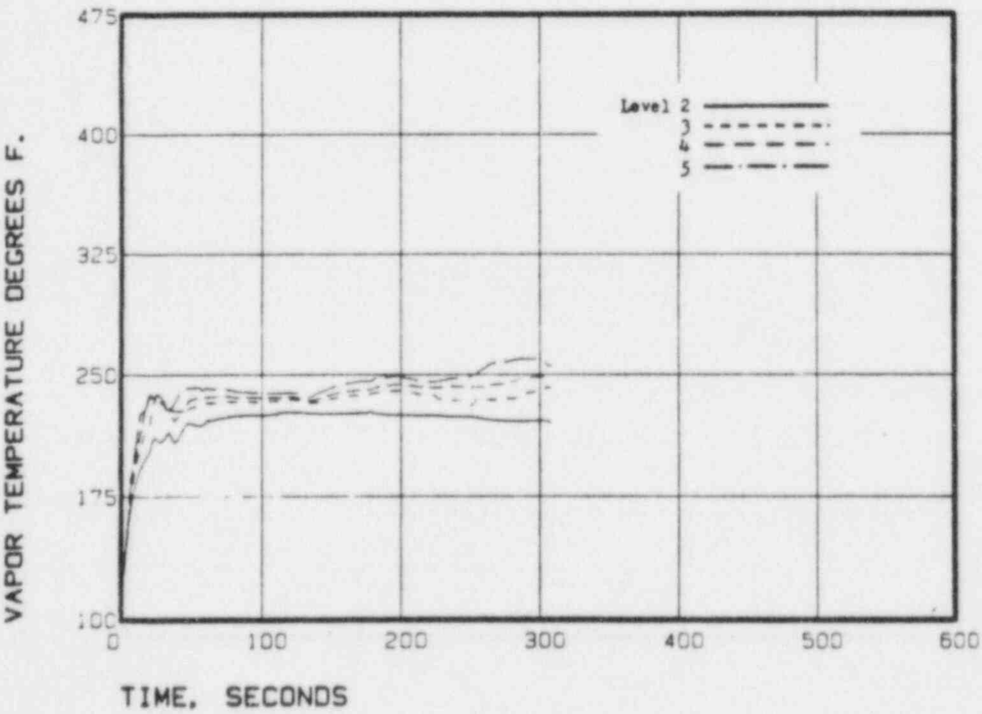

FIGURE 6.27. Model 3 Temperature History in Channel 11

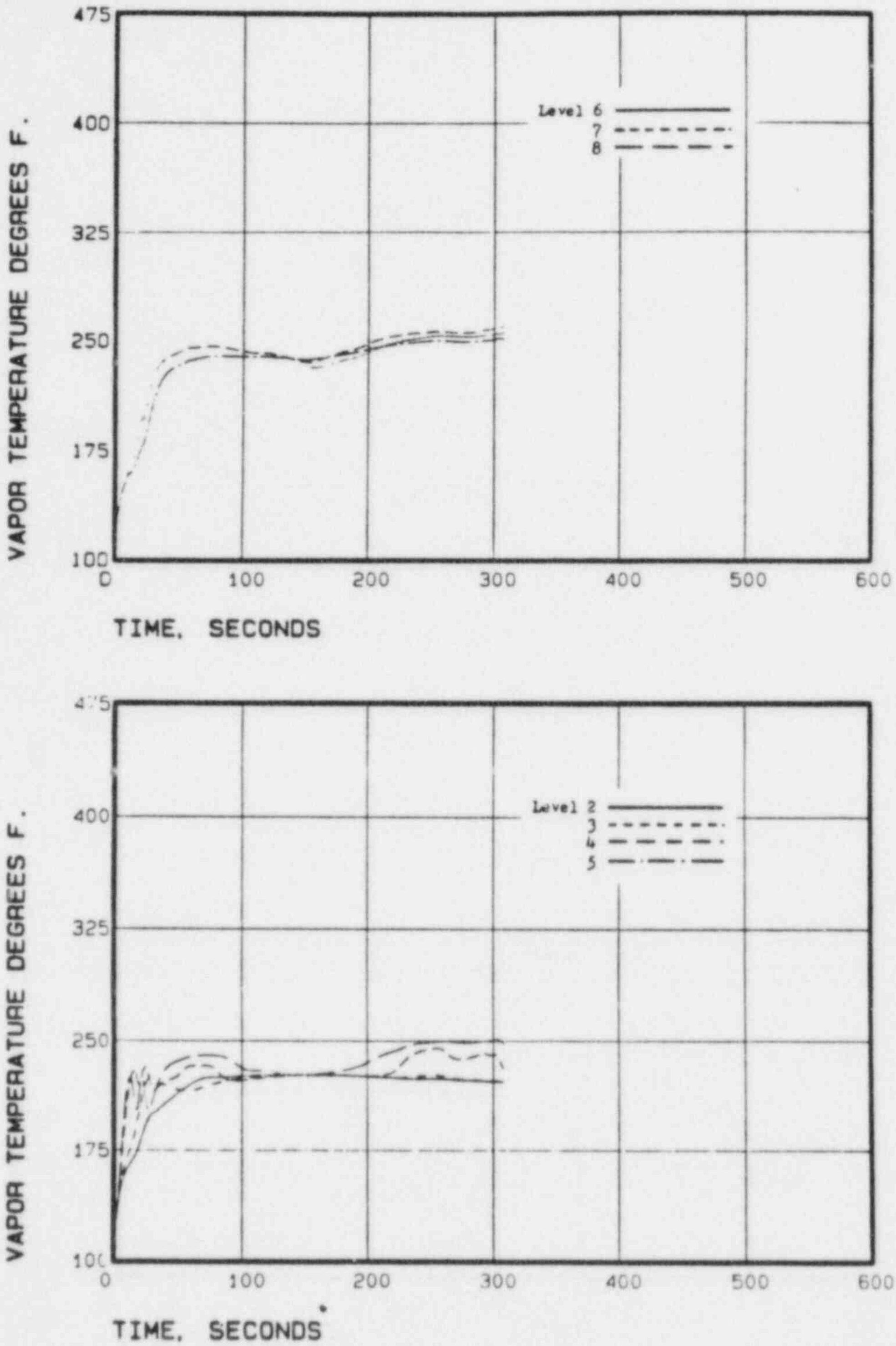

FIGURE 6.28. Model 3 Outer Compartment Temperatures - Channel 8

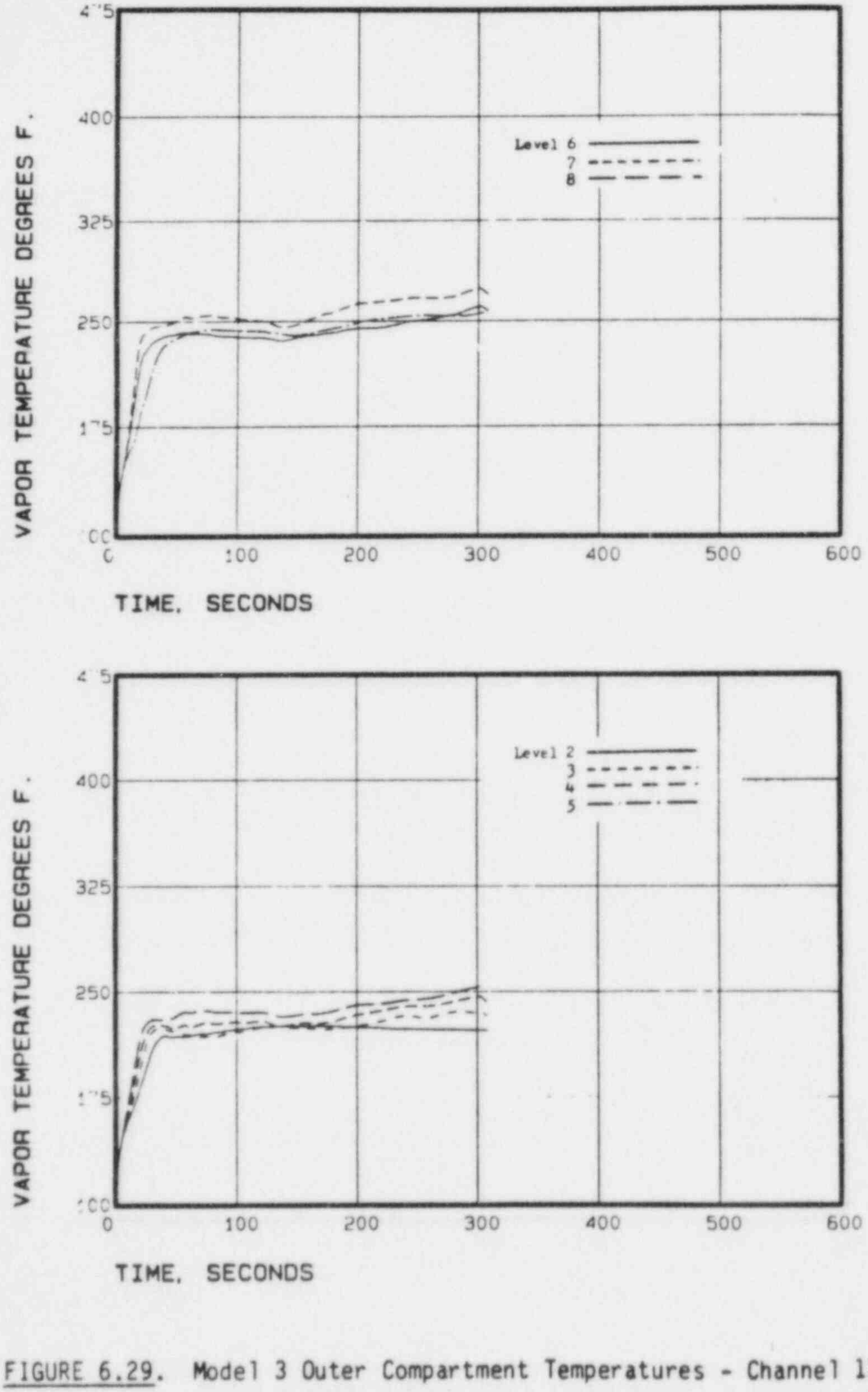

FIGURE 6.29. Model 3 Outer Compartment Temperatures - Channel 12

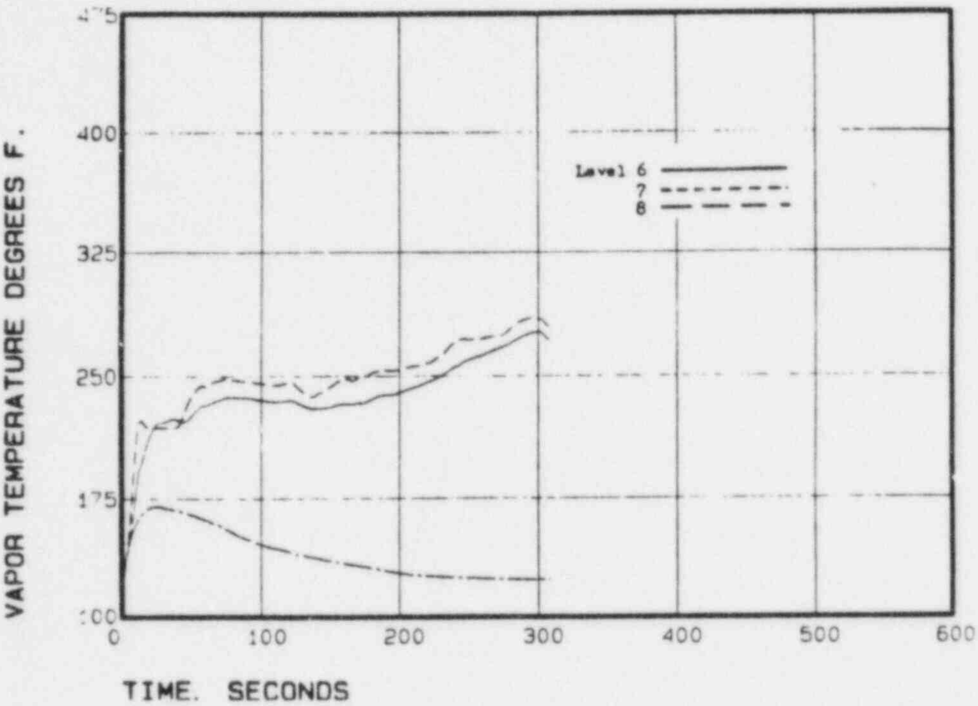

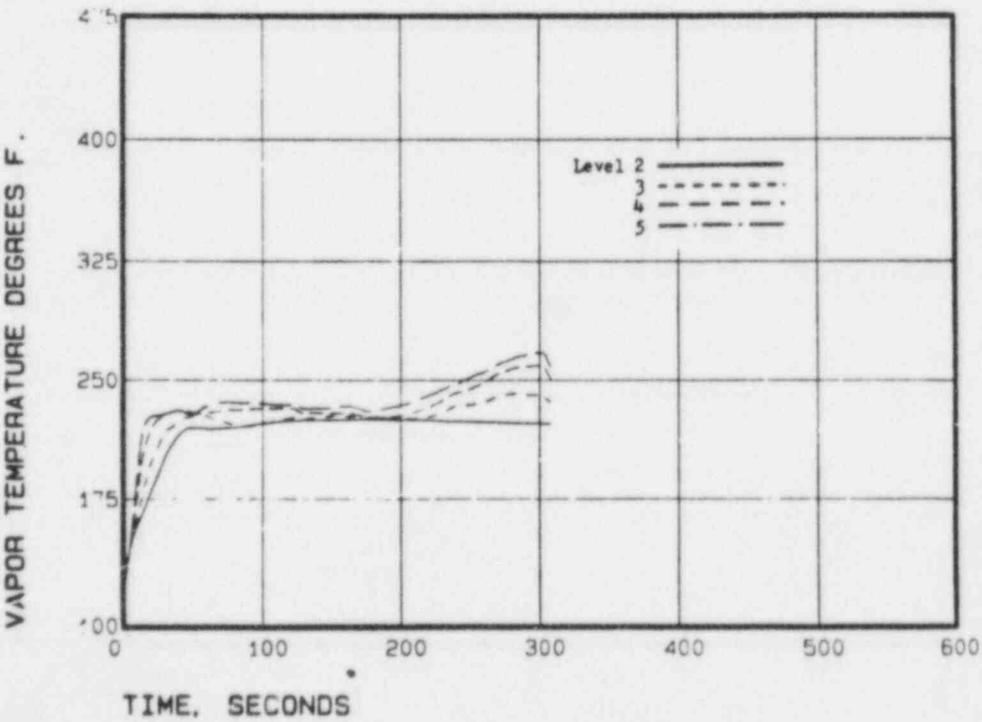

FIGURE 6.30. Model 3 Outer Compartment Temperatures - Channel 16

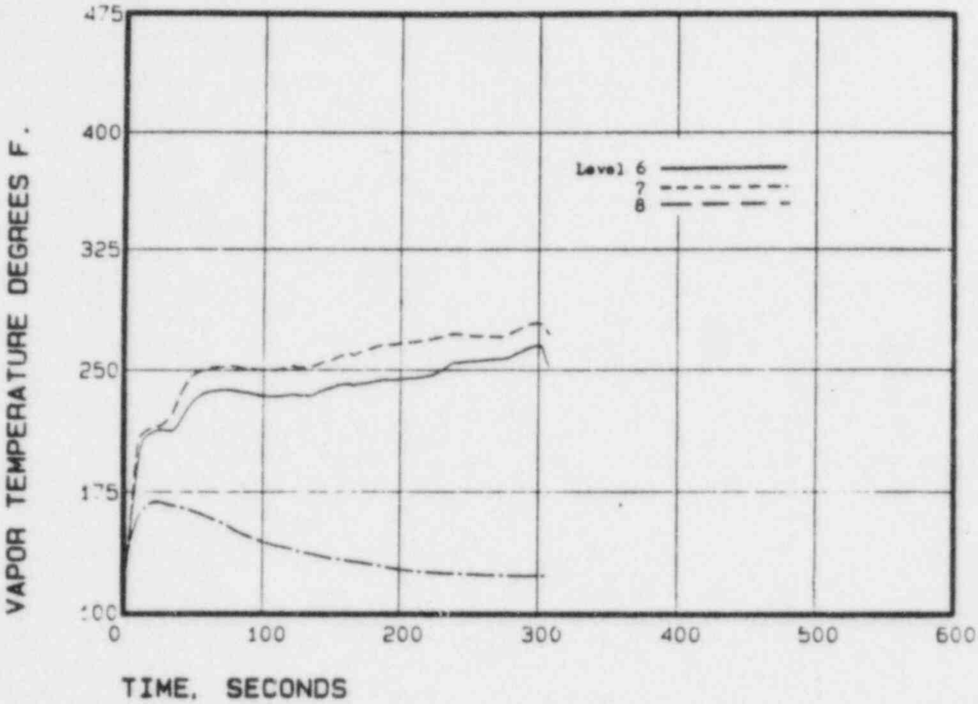

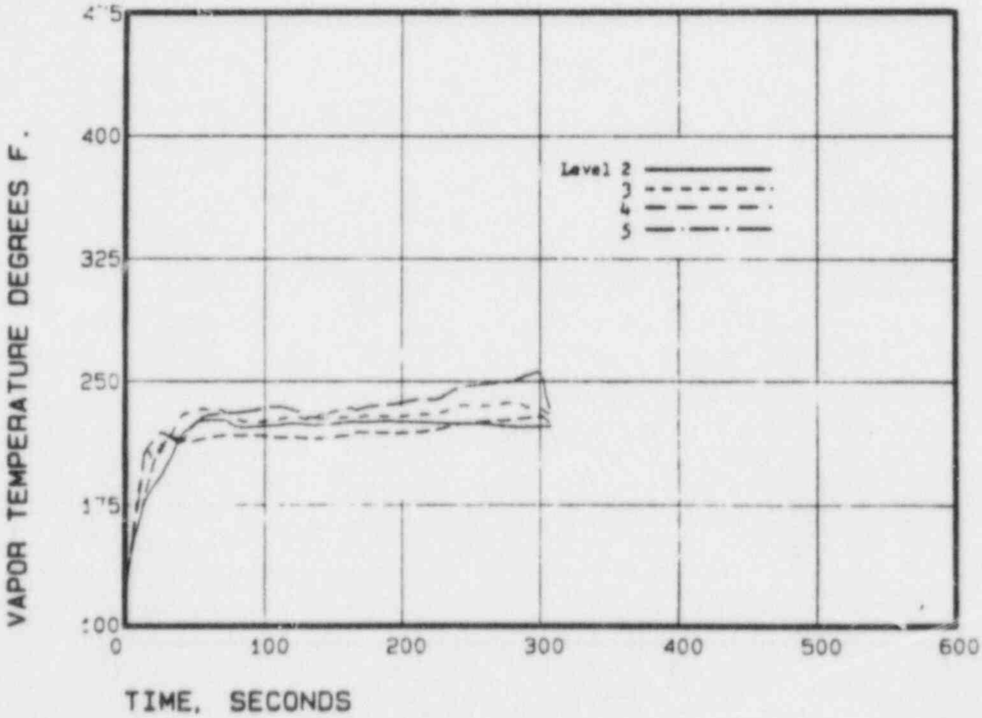

FIGURE 6.31. Model 3 Outer Compartment Temperatures - Channel 20

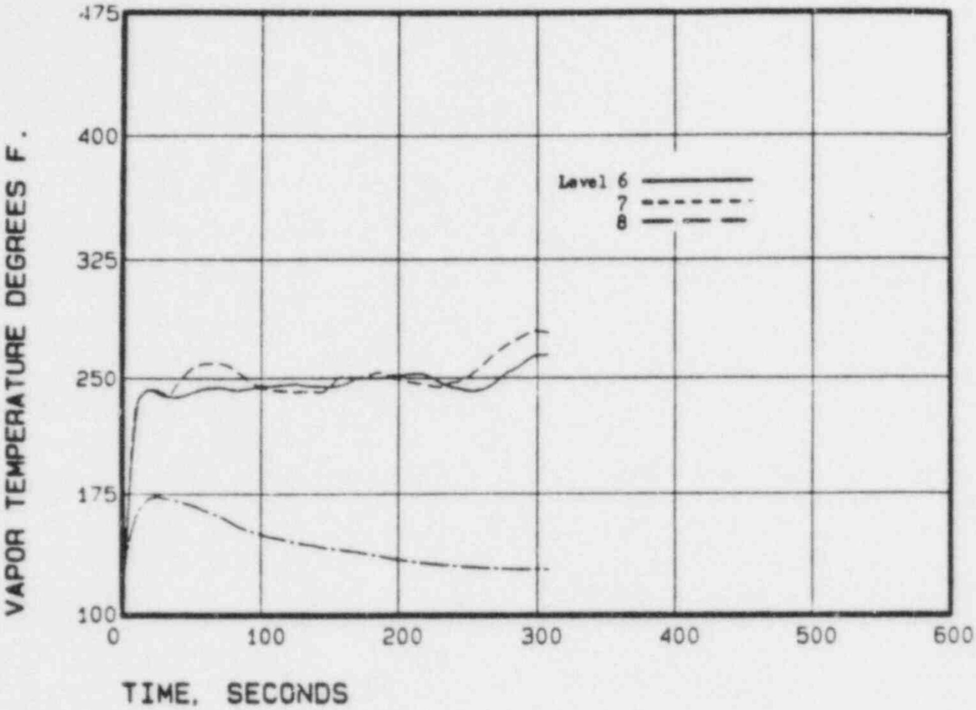

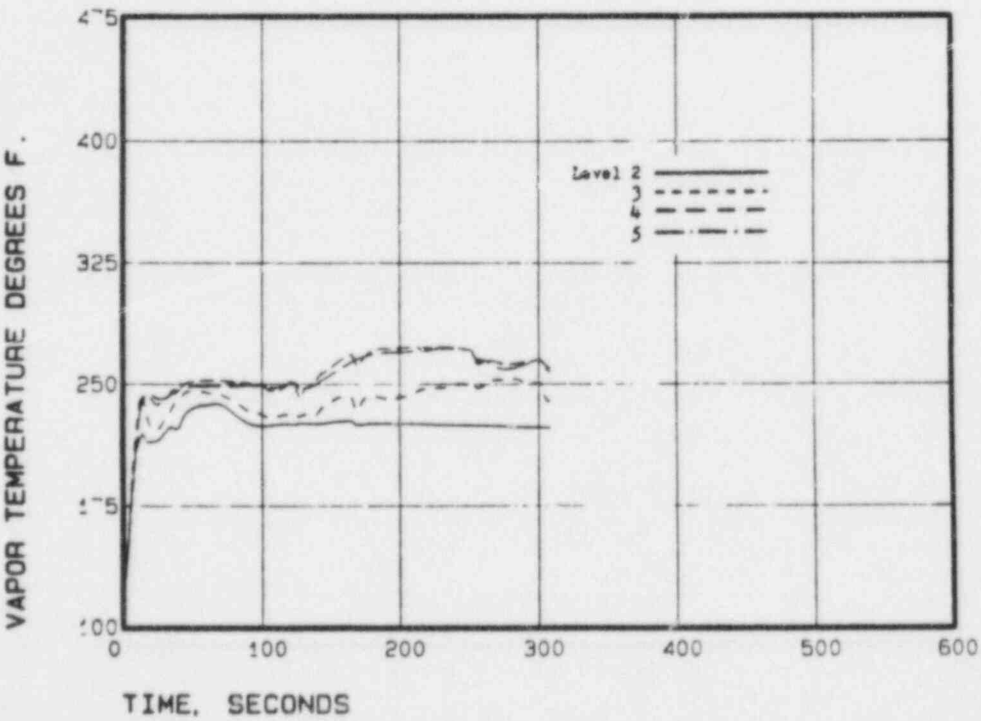

FIGURE 6.32. Model 3 Outer Compartment Temperatures - Channel 24

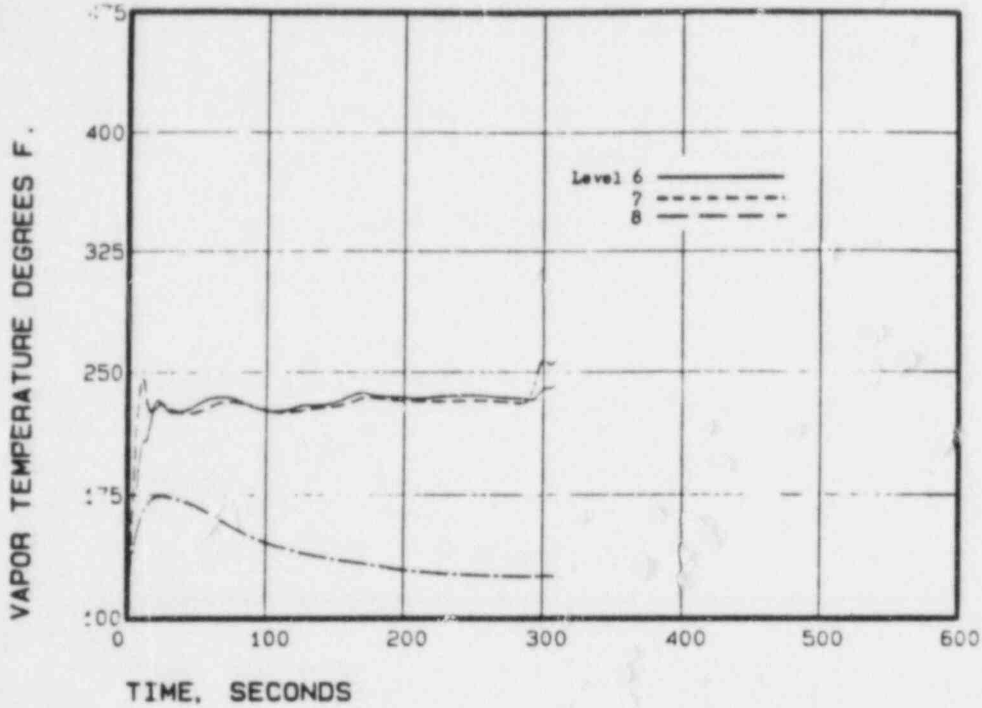

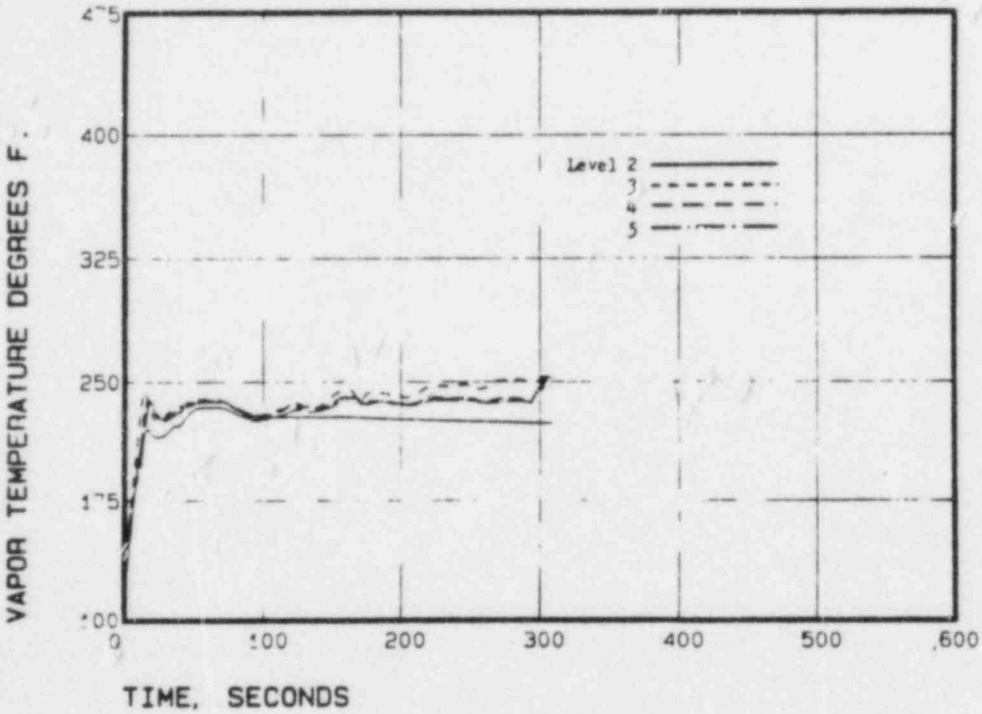

FIGURE 6.33. Model 3 Outer Compartment Temperatures - Channel 28

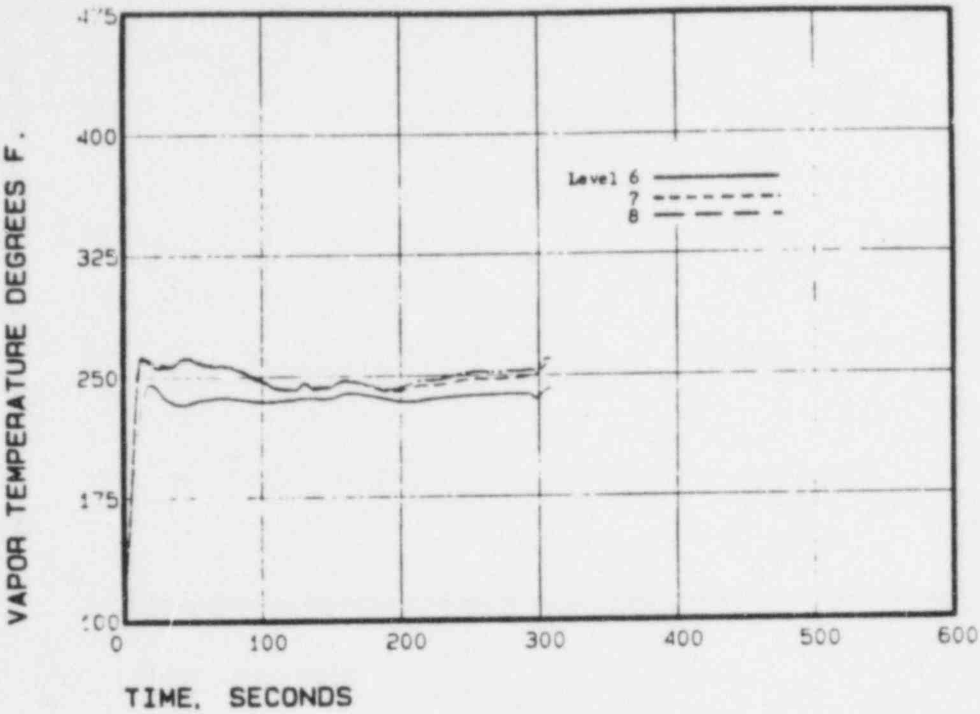

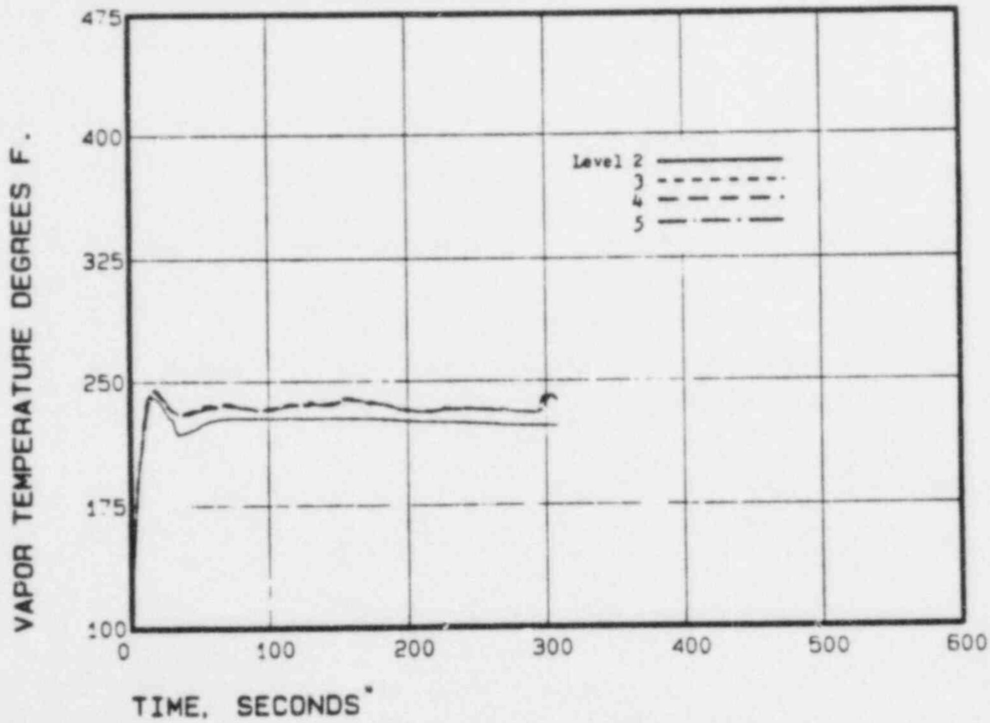

FIGURE 6.34. Model 3 Outer Compartment Temperatures - Channel 32

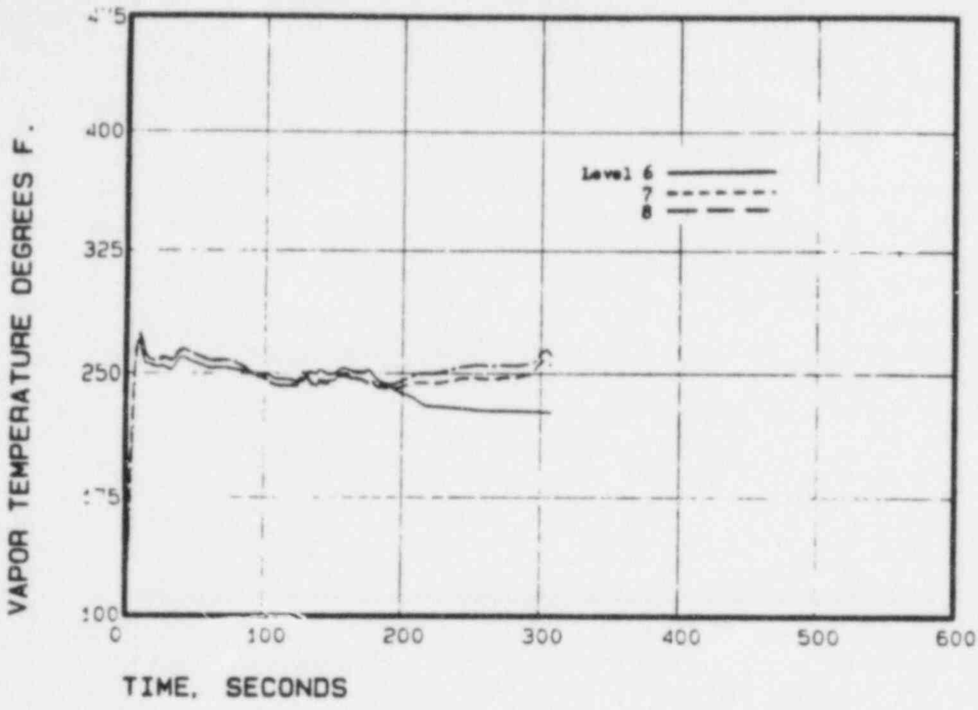

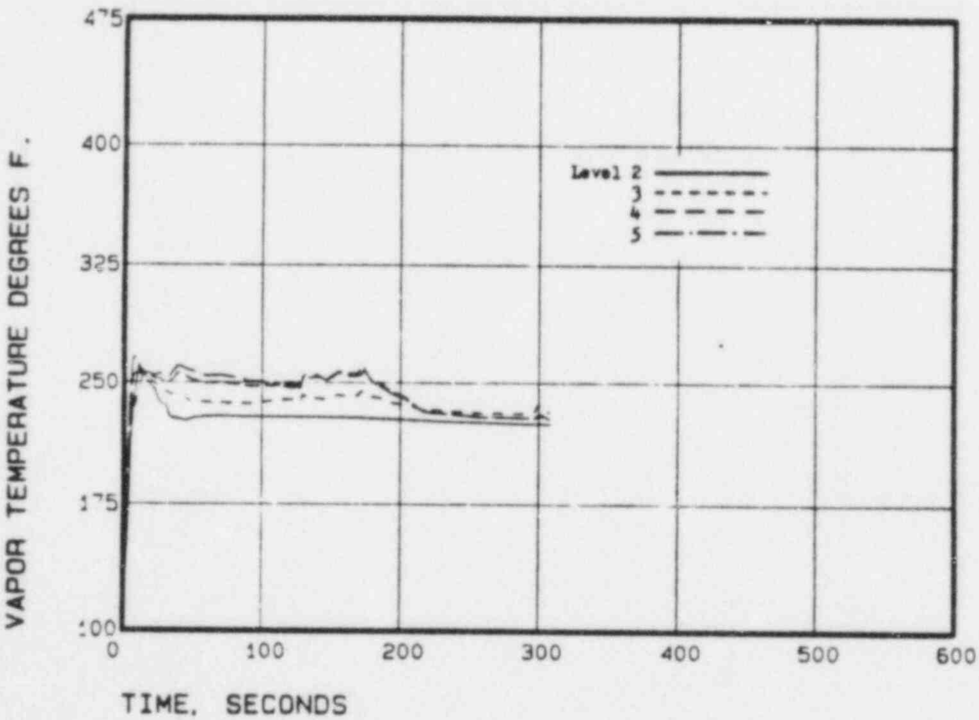

FIGURE 6.35. Model 3 Outer Compartment Temperatures - Channel 36

causing the initial heatup. This steam condenses leaving a steam fraction of about 10% at 300 seconds and therefore, a much lower saturation temperature.

Figure 6.36 shows temperature contour maps at 300 seconds. The results are very similar to Model 2 indicating good mixing around the containment.

Typical slab surface temperatures are shown in Figures 6.37, 6.38, and 6.39. The curves are for concrete, thin steel and thick steel at level 6 in channels 31, 23, and 11. The plots indicate some superheating of the steel although much less than for Model 1 because of the lower steam temperatures. The curves show the concrete surface temperature cooling after various times in the transient. At these times the doors above closed with cold air dropping down from the upper containment and collecting behind the doors. The steam partial pressure decreased along with the liquid saturation temperature. This made the drain water introduced as a film on the crane wall in these channels substantially subcooled at the lower containment steam pressures. The net effect of the cold liquid on the walls was reduced revaporization since the steam must first heat the water to the saturation temperature.

The lower containment pressure history is shown in Figure 6.40. The pressure history of all three models was nearly identical. Initially the pressure rises to 21 psia as the air in the lower containment is forced into the upper containment. The pressure begins to drop off slowly as air drops back down into the ice condenser and steam that passed through the ice bed during the initial blowdown phase condenses in the upper containment.

The air concentration is shown in Figures 6.41 and 6.42. Except for the nearly isolated outer compartments at the top of Channels 16, 20, 24 and 28, there is very little air left in the lower containment. Figure 6.42 shows the unwrapped outer compartment around the containment. The region at the top of Figure 6.42 is the upper deck region in the containment which has a high air fraction. The air concentration profiles in the lower conpartment indicate the entrance of the dead ended compartments.

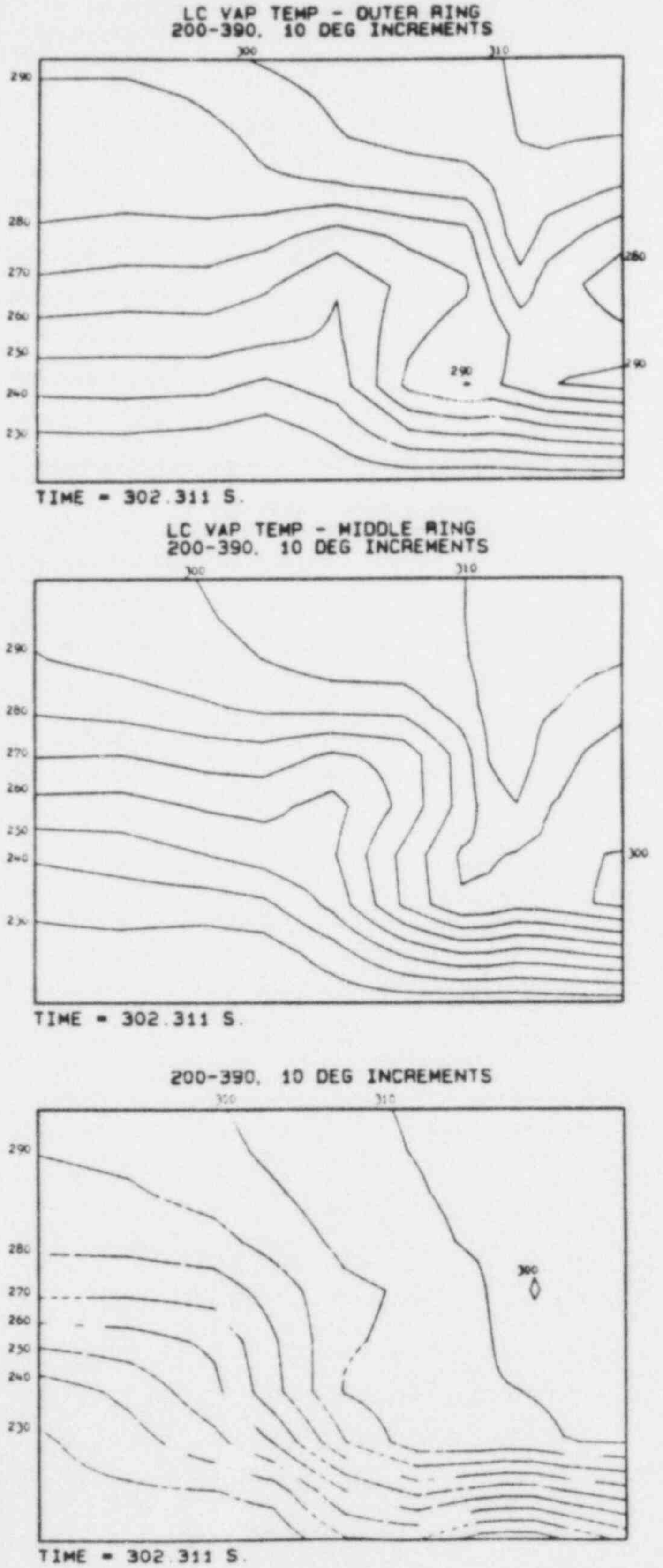

FIGURE 6.36. Model 3 Lower Containment Vapor Temperatures at 300 Seconds

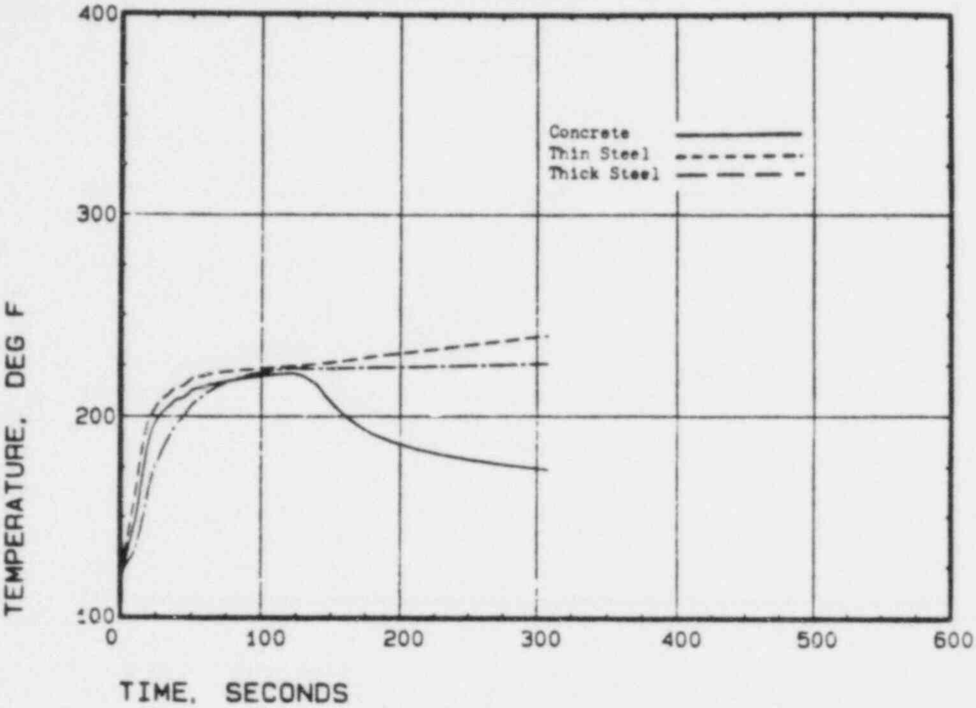

FIGURE 6.37. Model 3 Typical Slab Surface Temperatures, Channel 31, Level 6

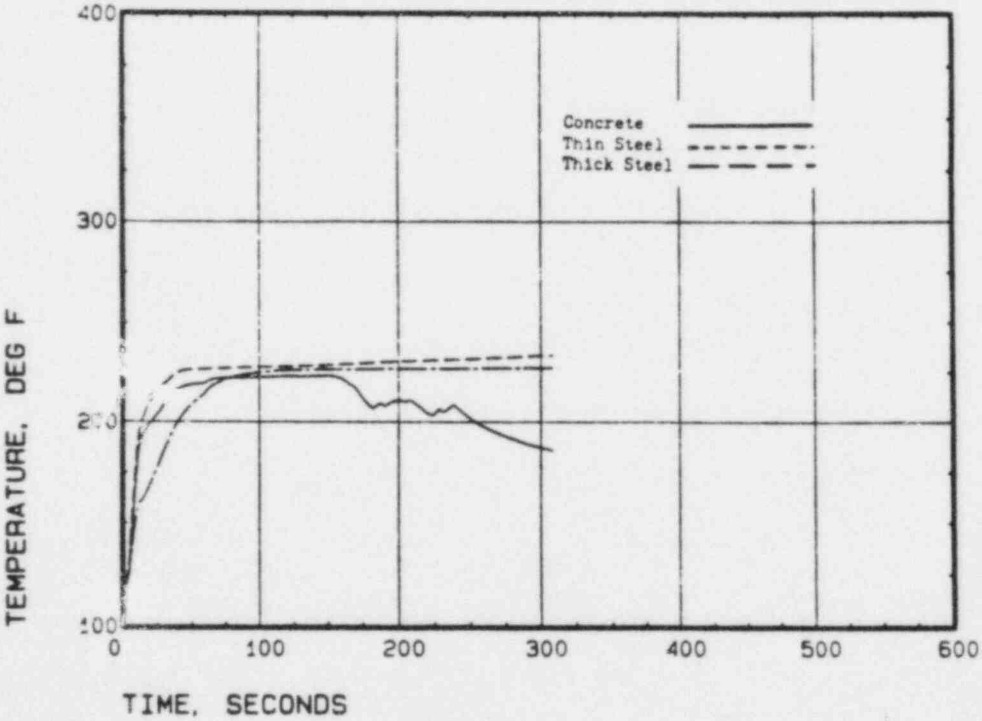

FIGURE 6.38. Model 3 Typical Slab Surface Temperatures, Channel 23, Level 6

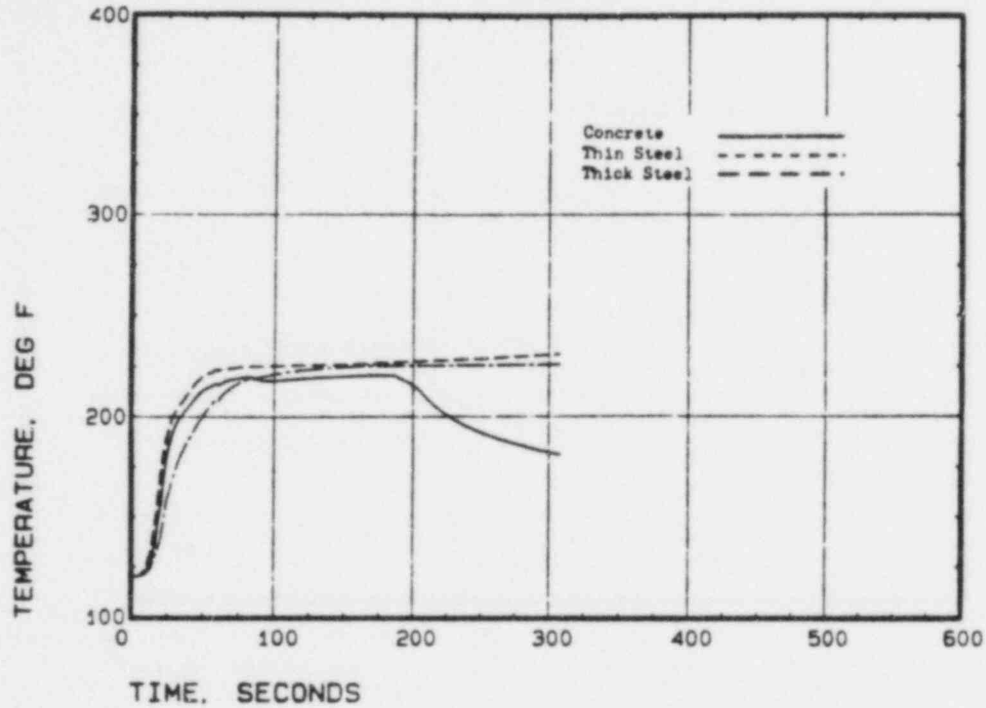

FIGURE 6.39. Model 3 Typical Slab Surface Temperatures, Channel 23, Level 6

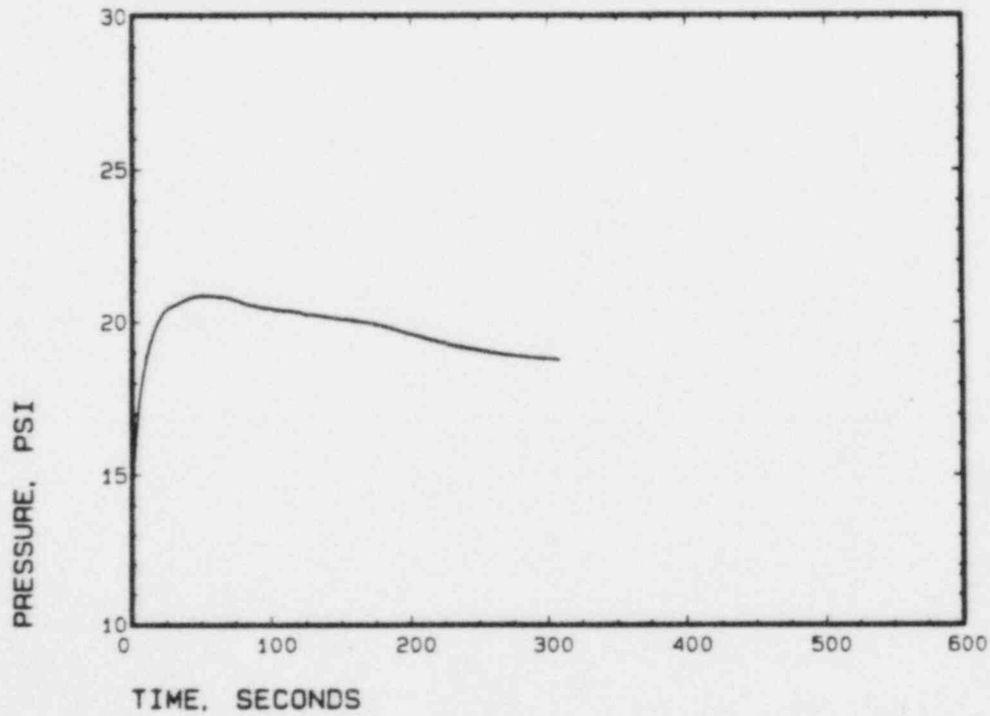

FIGURE 6.40. Model 3 Lower Containment pressure History

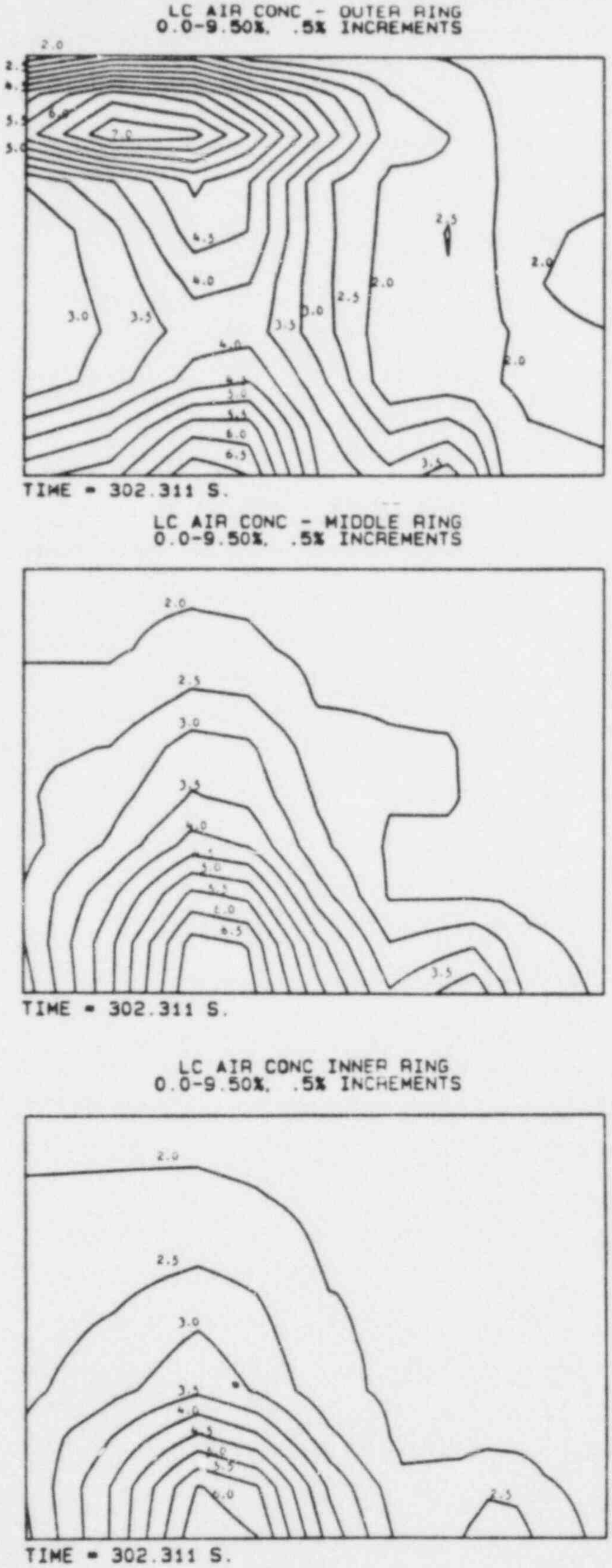

FIGURE 6.41. Model 3 Lower Containment Air Concentration Contours at 300 Seconds

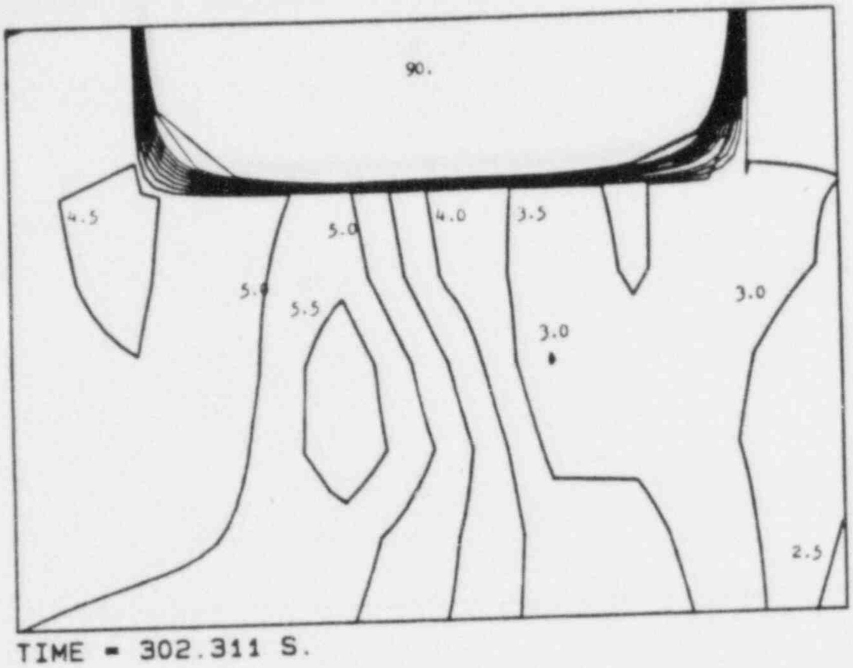

FIGURE 6.42. Model 3 Outer Compartment Air Concentration Contours at 300 Seconds.

Figures 6.43, 6.44, and 6.45 show vector plots of the vapor at 300 seconds. The maximum velocities are about a factor of three times higher than those from Model 2. This is a direct result of the finer noding in the break region. The jet momentum is not diffused as rapidly with the smaller cells. Note that for this cut the velocities in the ice condenser are downward on both sides of the containment. The axial cuts shown in figure 6.45 are at levels 2, 6 and 10.

Figures 6.46, 6.47 and 6.48 show similar vector plots for the entrained drop velocity. From Figure 6.47 it can be seen that drops as far away as channel 23 are being swept toward the break. Figure 6.46 shows that just downstream of the break the velocity of drops coming up from below is actually larger than the downward velocity of the drops above the break. That is because the drops above the break are injected with no velocity and must be accelerated by gravity and the vapor. Below the break the drops are smaller in diameter due to vaporization and they travel with nearly the vapor velocity.

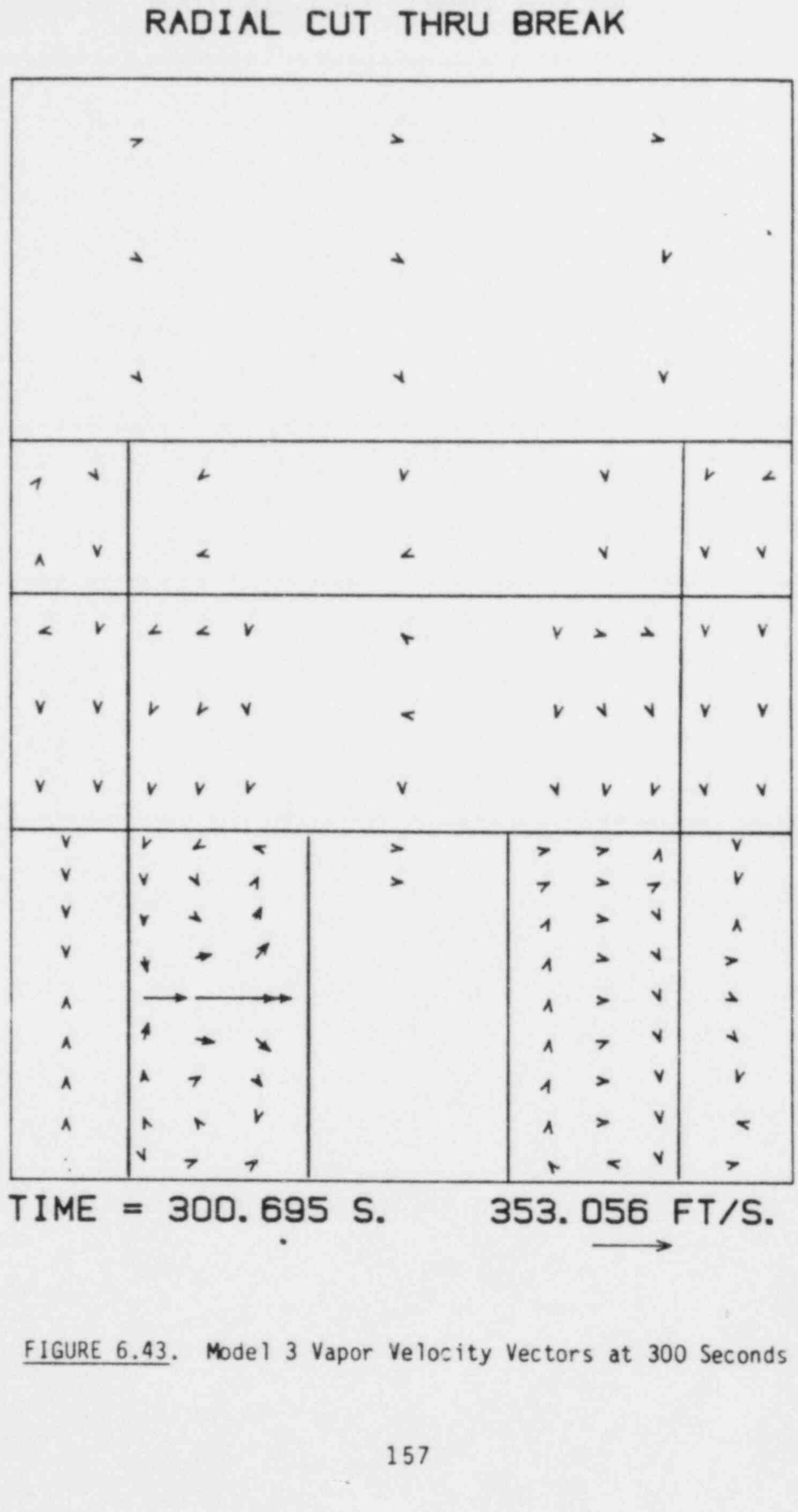

FIGURE 6.43. Model 3 Vapor Velocity Vectors at 300 Seconds

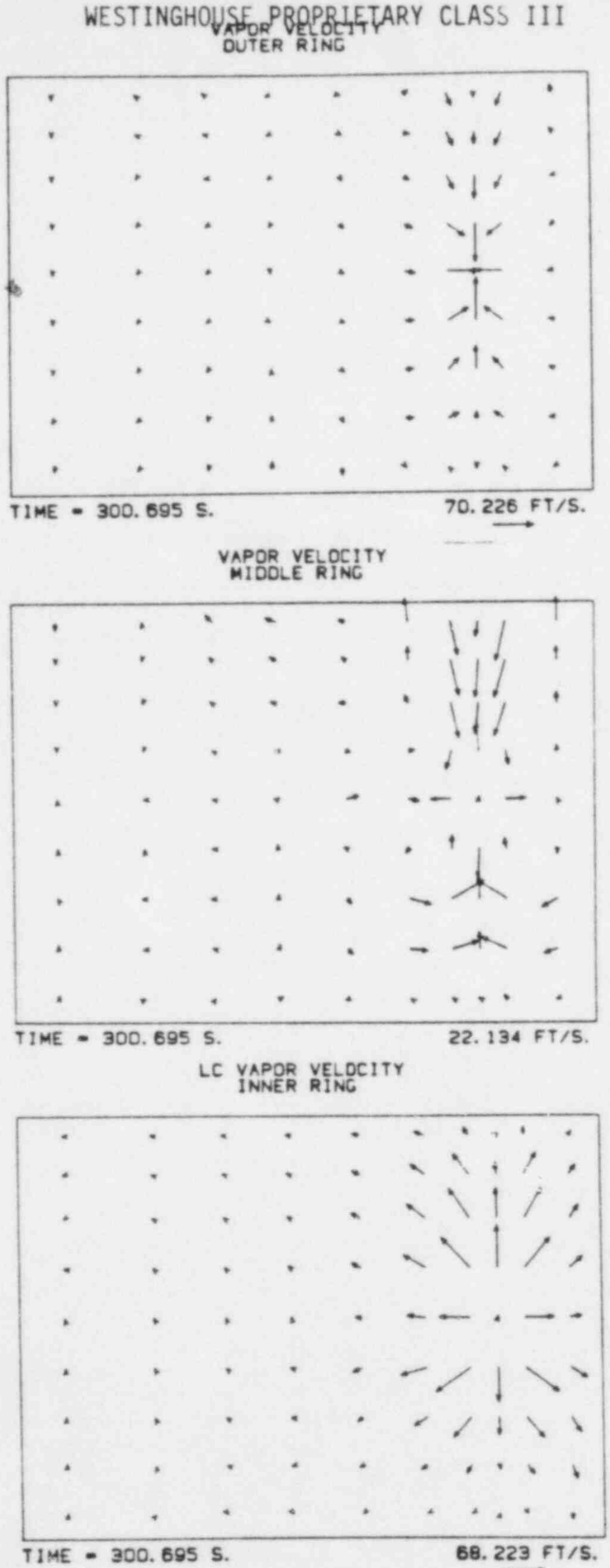

FIGURE 6.44. Model 3 Lower Containment Vapor Velocity Vectors at 300 Seconds

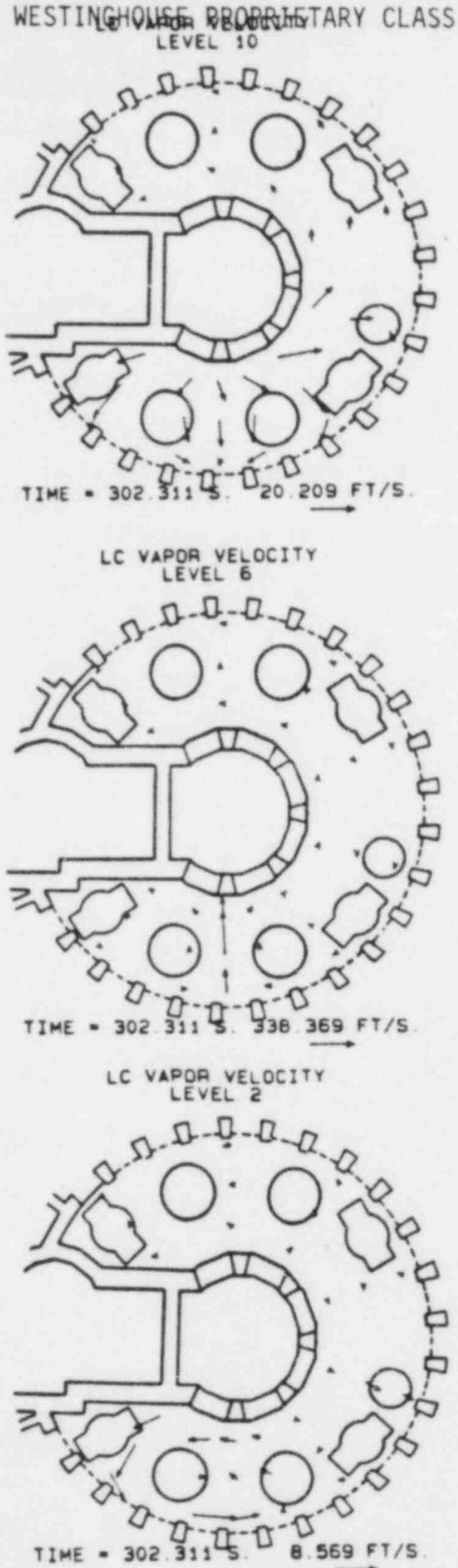

FIGURE 6.45. Model 3 Lower Containment Vapor Velocity Vectors at Seconds Levels 2, 6 and 10

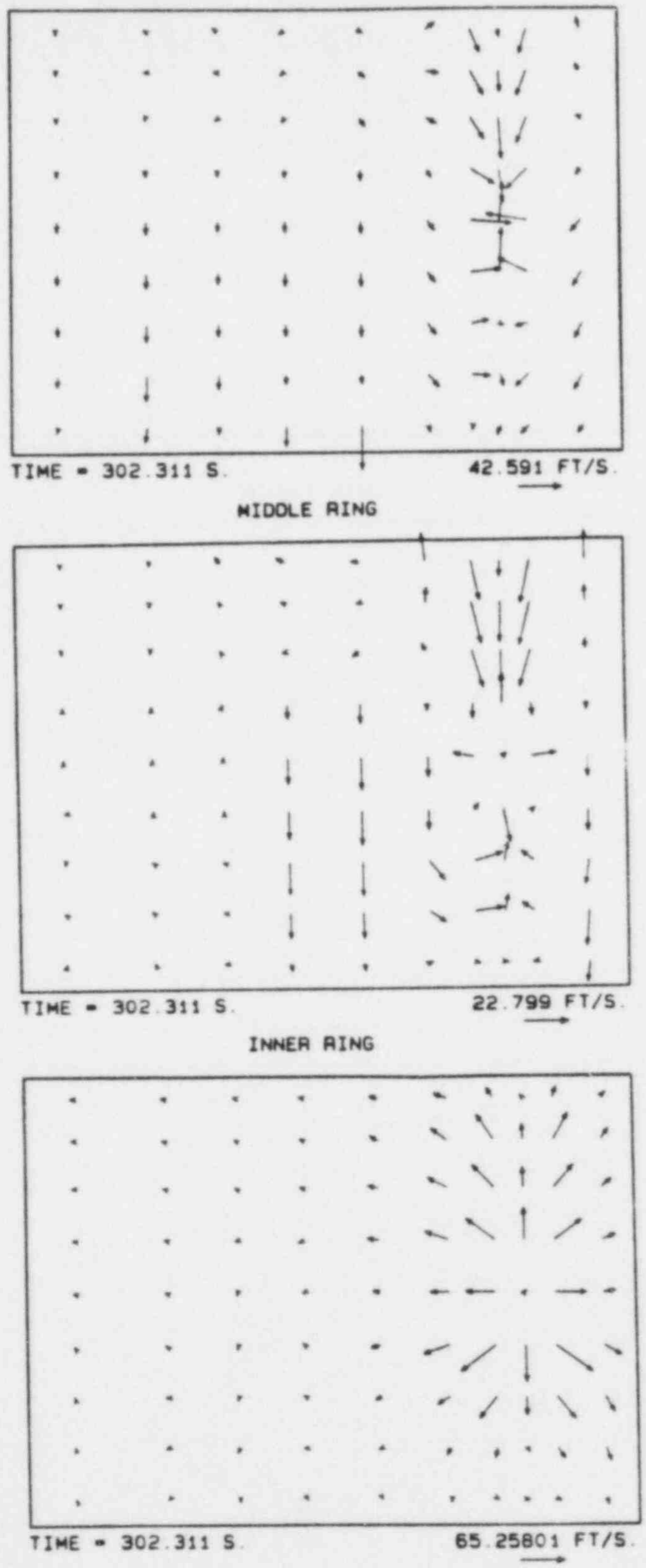

FIGURE 6.46. Model 3 Drop Velocity Vector at 300 Seconds

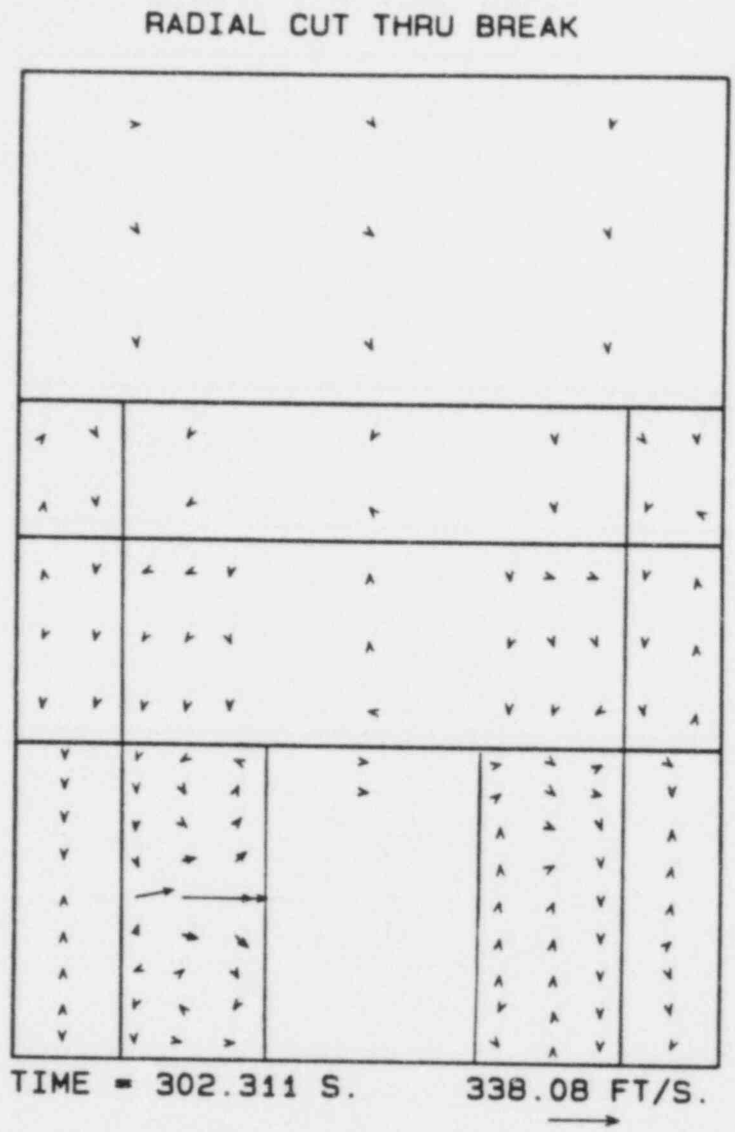

FIGURE 6.47. Model 3 Lower Containment Drop Velocity at 300 Seconds

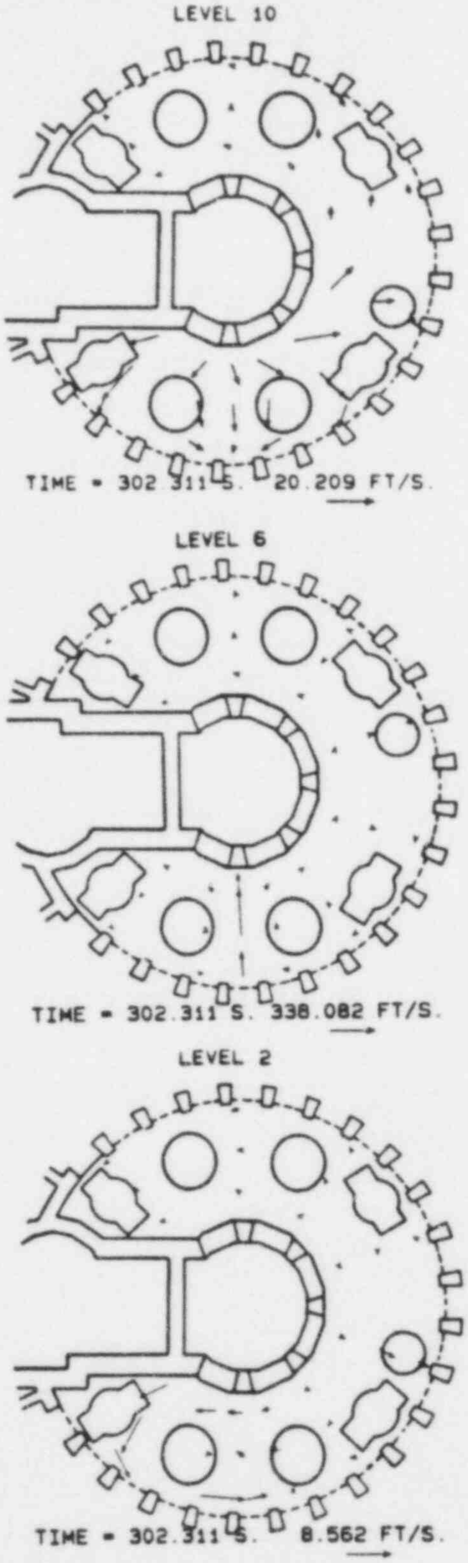

FIGURE 6.48. Model 3 Lower Containment Drop Velocity at 300 Seconds Levels 2, 6 and 10.

Figure 6.49 shows vector plots in the two rings of the ice condenser at 300 seconds. The bottom block of arrows represents the velocities in the door region in Section B. The upper block represents those parts of the ice condenser in Sections C and D. At the door level the velocity is predominately into the plot (if the door is open) so that large axial velocities do not appear. Referring to the ice condenser sector by the lower containment channel number beneath it, it can be seen that the majority of the steam flow goes up sectors 8, 24, and 36. Most of the other sectors have down flow. It also is apparent that most of the flow goes up the inside ring and that there is quite a bit of recirculation induced in the outside ring.

Figure 6.50 shows contour plots of the fraction of initial ice remaining at 300 seconds. The ice melt is the greatest at the inside ring in sector 36 which receives the greatest share of steam flow. At all locations more than 50% of the initial ice remains and nearly all of it remains in the upper levels of the ice bed.

The ice condenser door velocities are shown in Figures 6.51 through 6.60. Except for door 20 between 250 and 300 seconds, there is no significant backflow through the doors. The doors on the cold side of the containment begin closing at about 190 seconds. Door 24 closed at 300 seconds, releasing the suspended drops in the ice condenser and causing the drop in the bulk temperature at the end of the simulation. The doors above the break closed early into the transient because of the low pressure created by the break jet. They opened momentarily at 120 seconds when door 36 closed and released suspended drops to the drains. In the later part of the transient the majority of the steam flow is through the top half of door 36.

Figures 6.61 and 6.62 show the drain flows for each sector of the ice condenser. Note that even though the doors above the break close early in the transient, the flow rates in all the drains on the hot side of the containment remain at a fairly high level. The recirculation within the ice condenser helps to even out the ice melt and the drain flow distribution.

ICE CONDENSER OUTSIDE CHANNELS

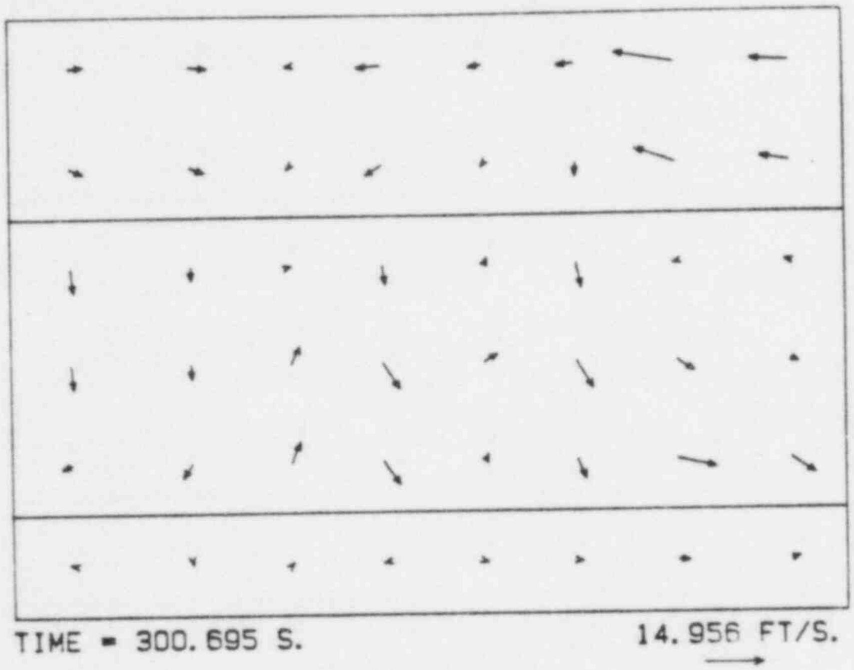

ICE CONDENSER INSIDE CHANNELS

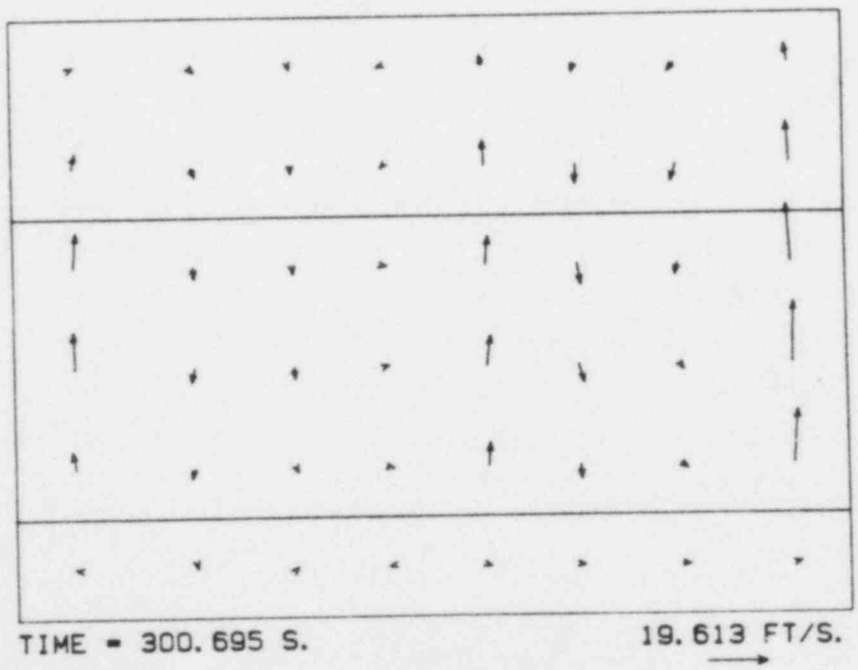

FIGURE 6.49. Model 3 Vapor Velocity Vectors in the Ice Condensers

MODEL 3 FRACTION OF INITIAL ICE AT 300 SEC. - OUTSIDE CHANNELS

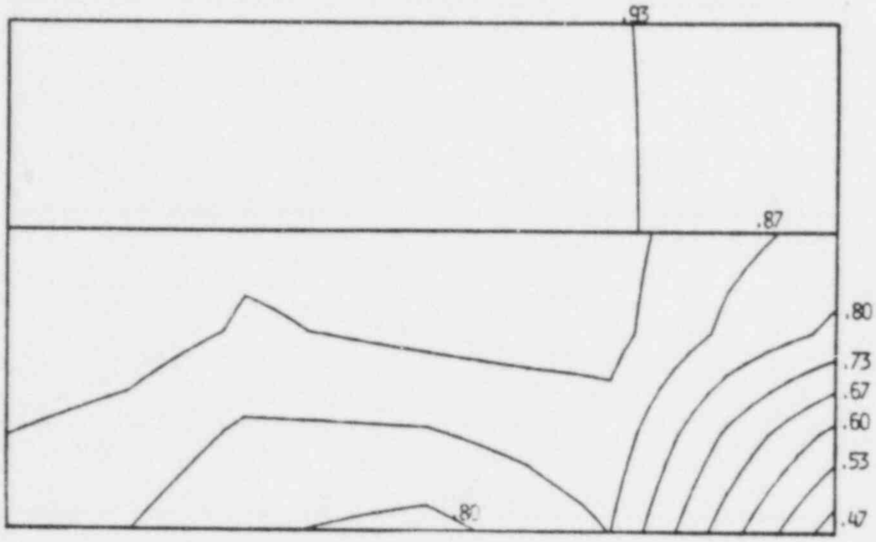

MODEL 3 FRACTION OF INITIAL ICE AT 300 SEC. - INSIDE CHANNELS

FIGURE 6.50. Model 3 Fraction of Initial Ice Contours at 300 Seconds

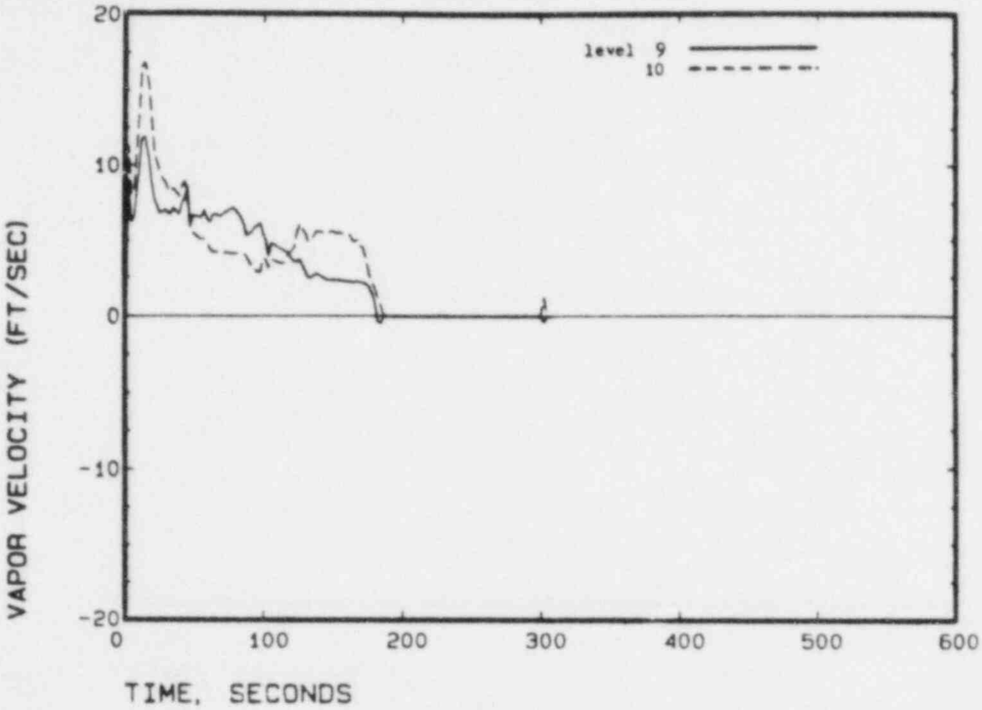

FIGURE 6.51. Model 3 Ice Condenser Door Vapor Velocities - Door 8

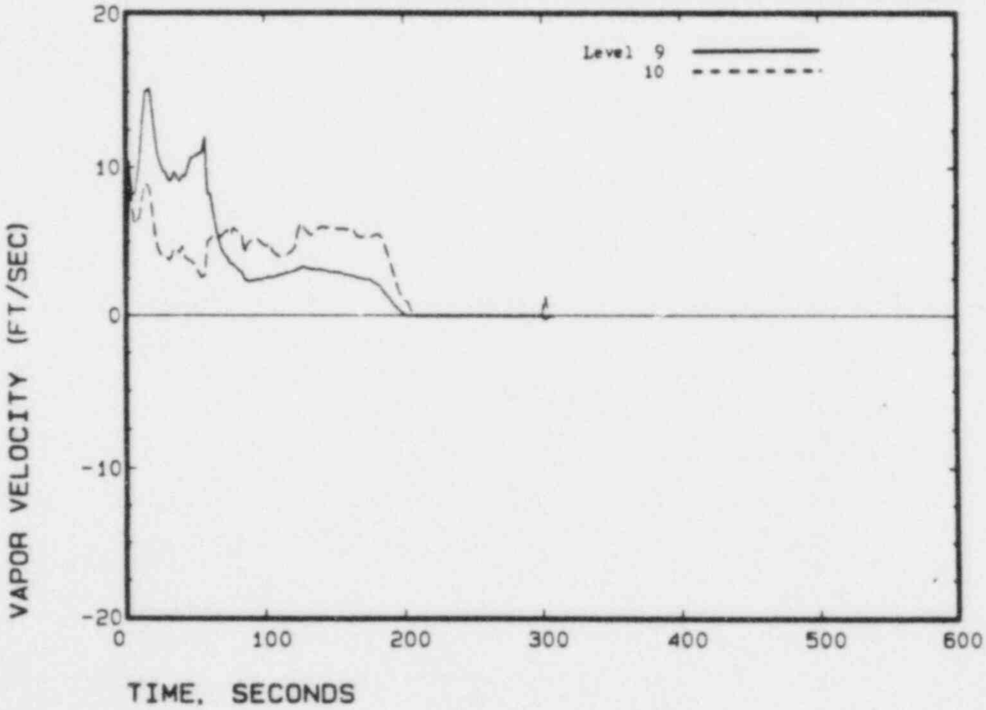

FIGURE 6.52. Model 3 Ice Condenser Door Vapor Velocities - Door 12

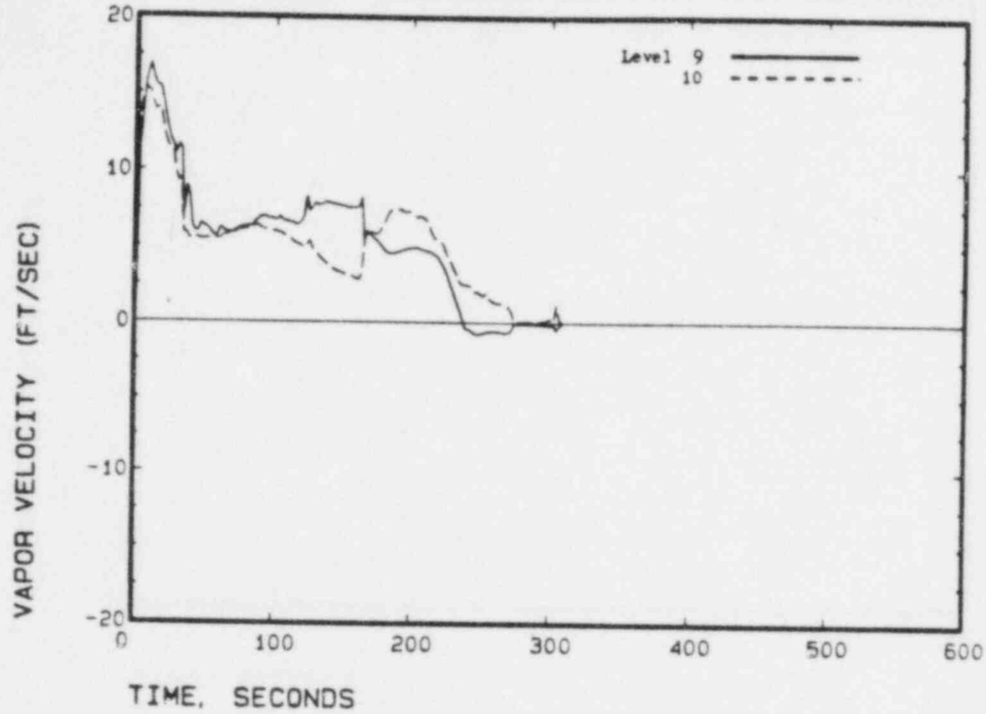

FIGURE 6.53. Model 3 Ice Condenser Door Vapor Velocities - Door 16

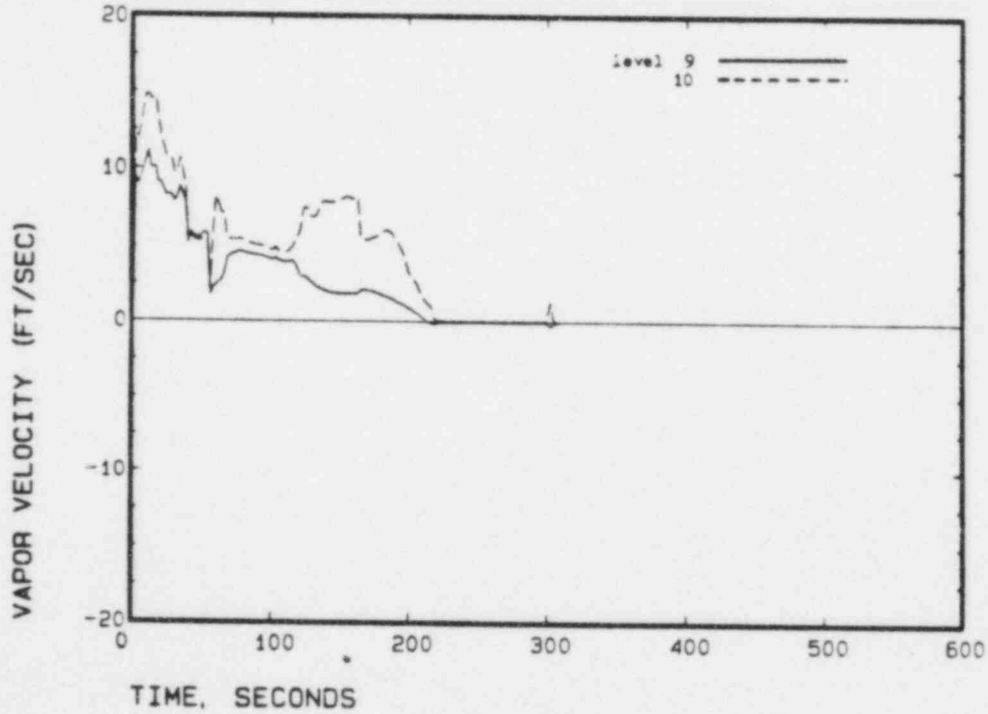

FIGURE 6.54. Model 3 Ice Condenser Door Vapor Velocities - Door 20

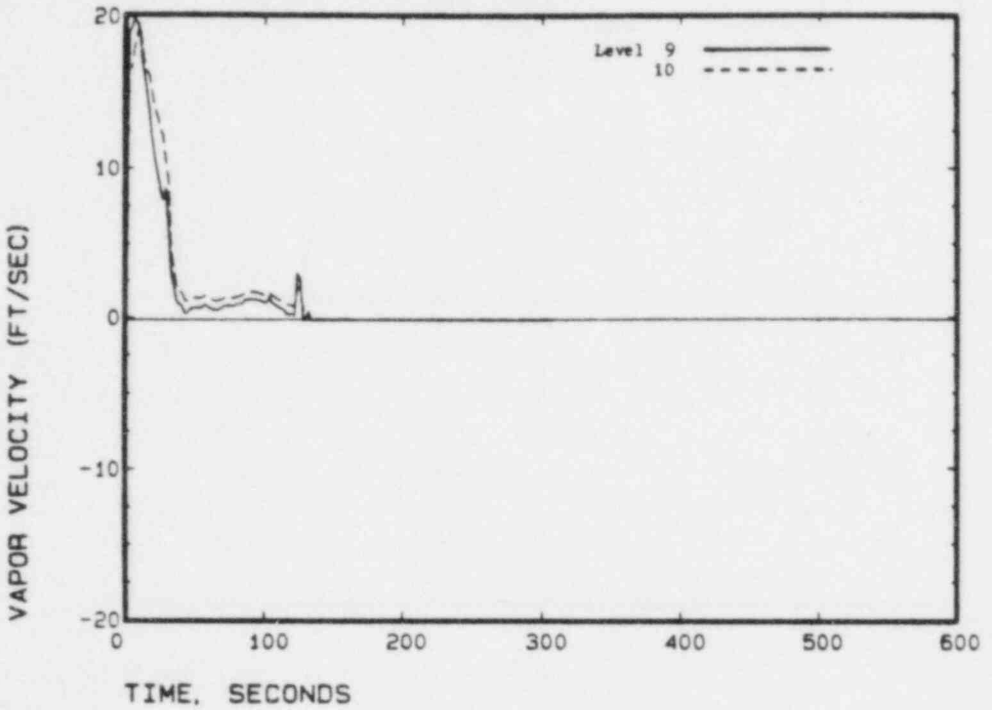

FIGURE 6.55. Model 3 Ice Condenser Door Vapor Velocities - Door 24

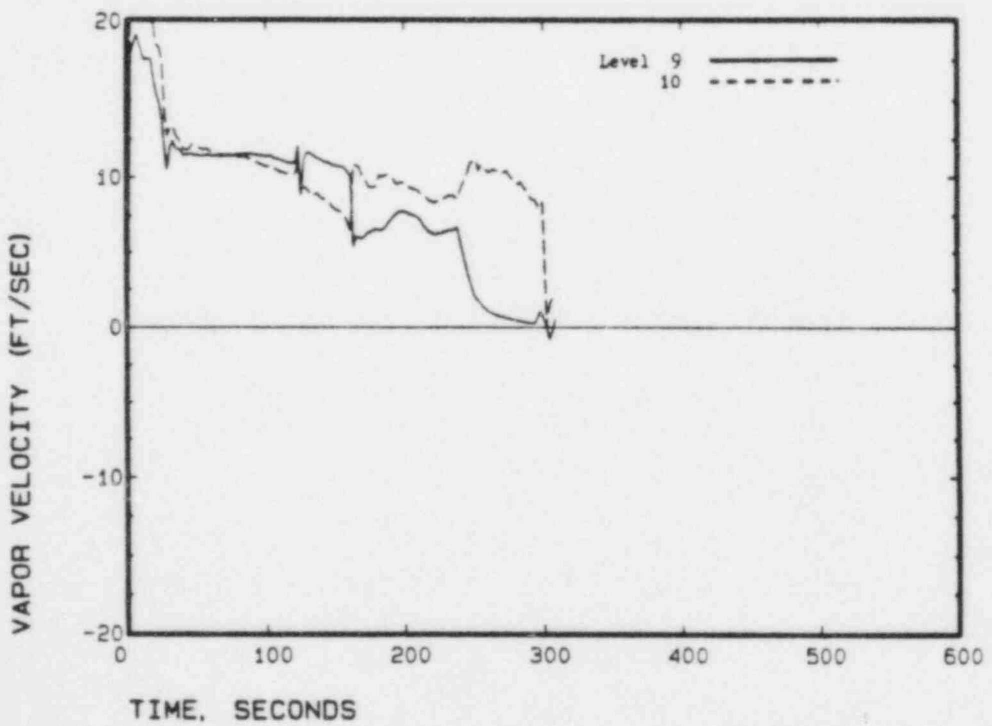

FIGURE 6.56. Model 3 Ice Condenser Door Vapor Velocities - Door 28

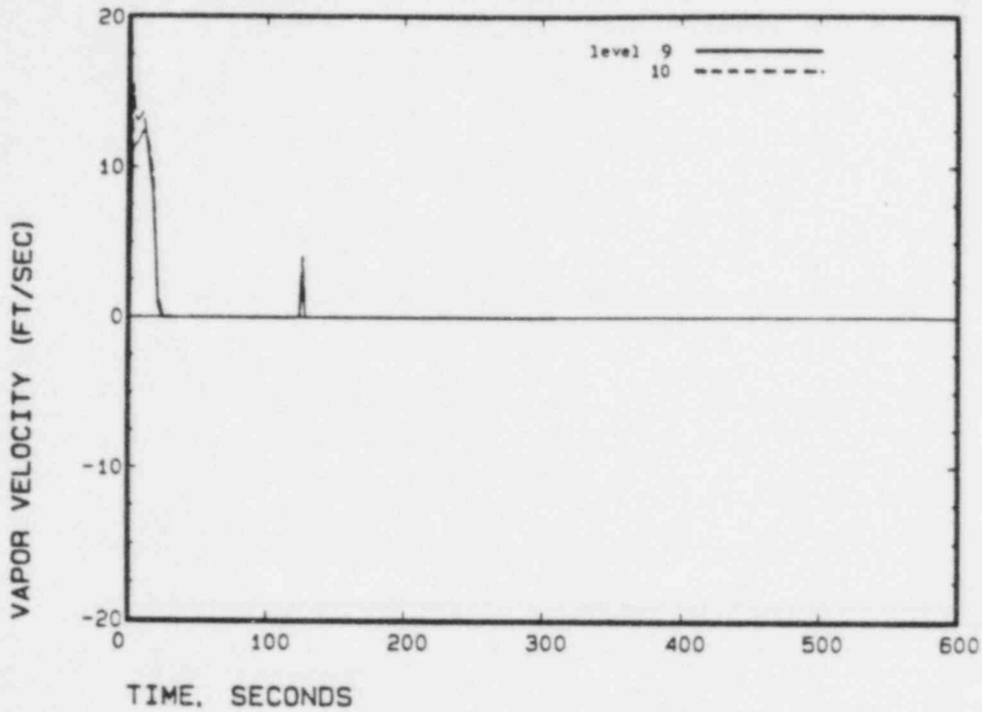

FIGURE 6.57. Model 3 Ice Condenser Door Vapor Velocities - Door 32a

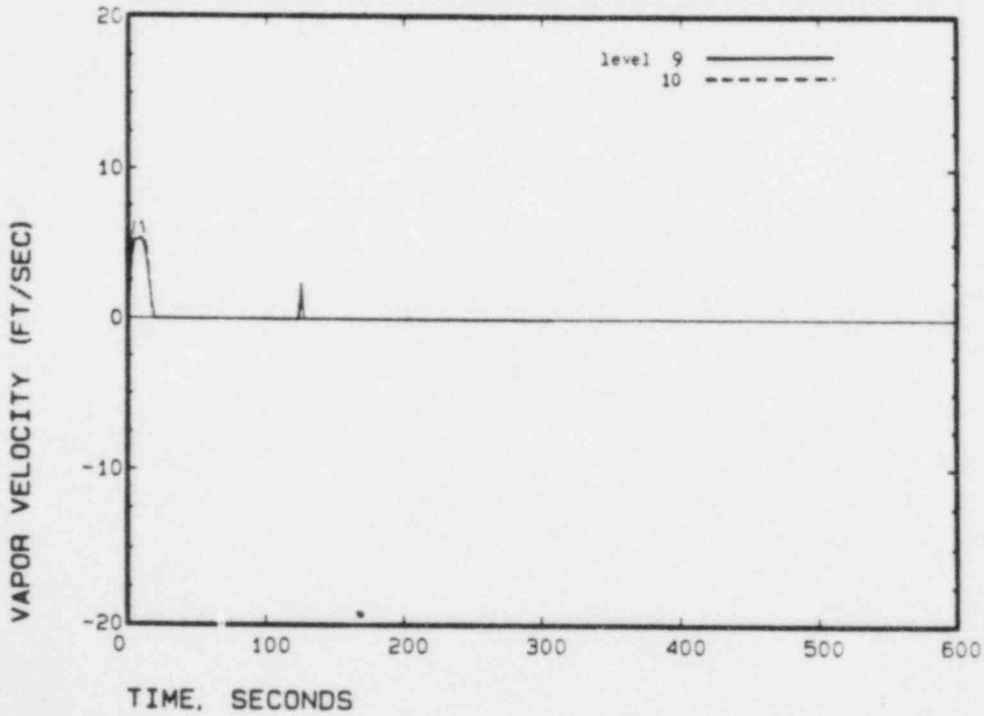

FIGURE 6.58. Model 3 Ice Condenser Door Vapor Velocities - Door 32b

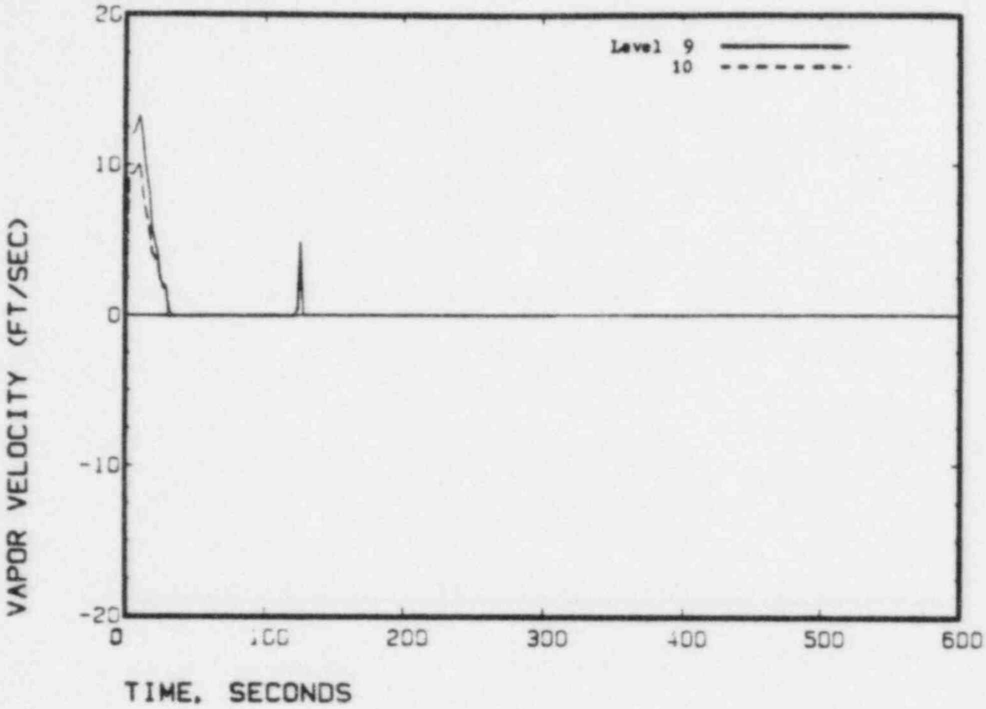

FIGURE 6.59. Model 3 Ice Condenser Door Vapor Velocities - Door 32c

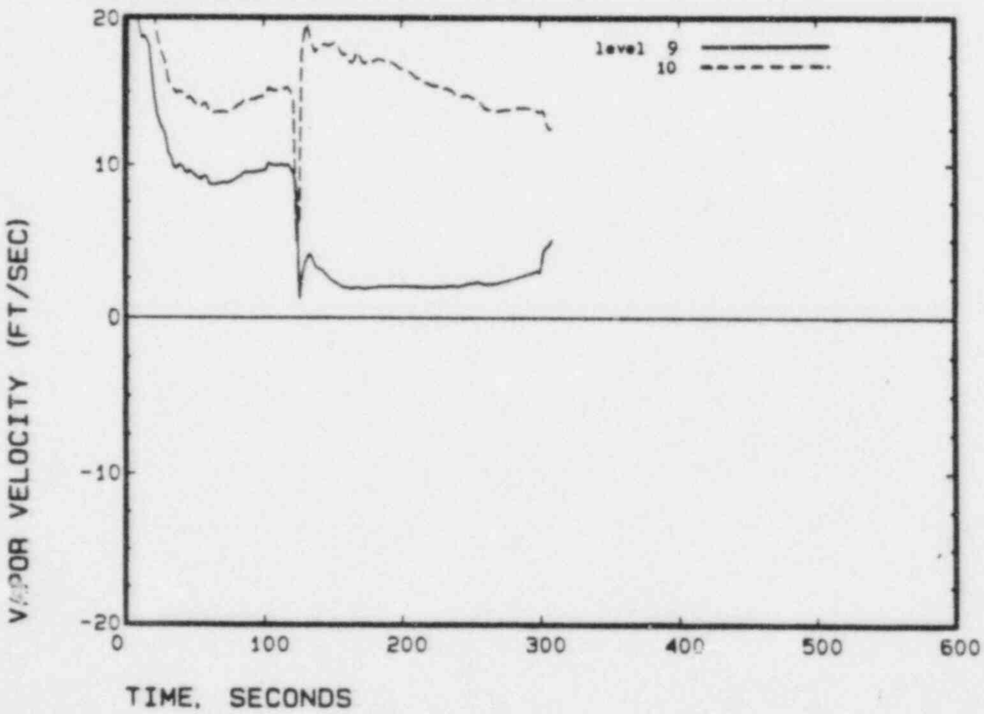

FIGURE 6.60. Model 3 Ice Condenser Door Vapor Velocities - Door 36

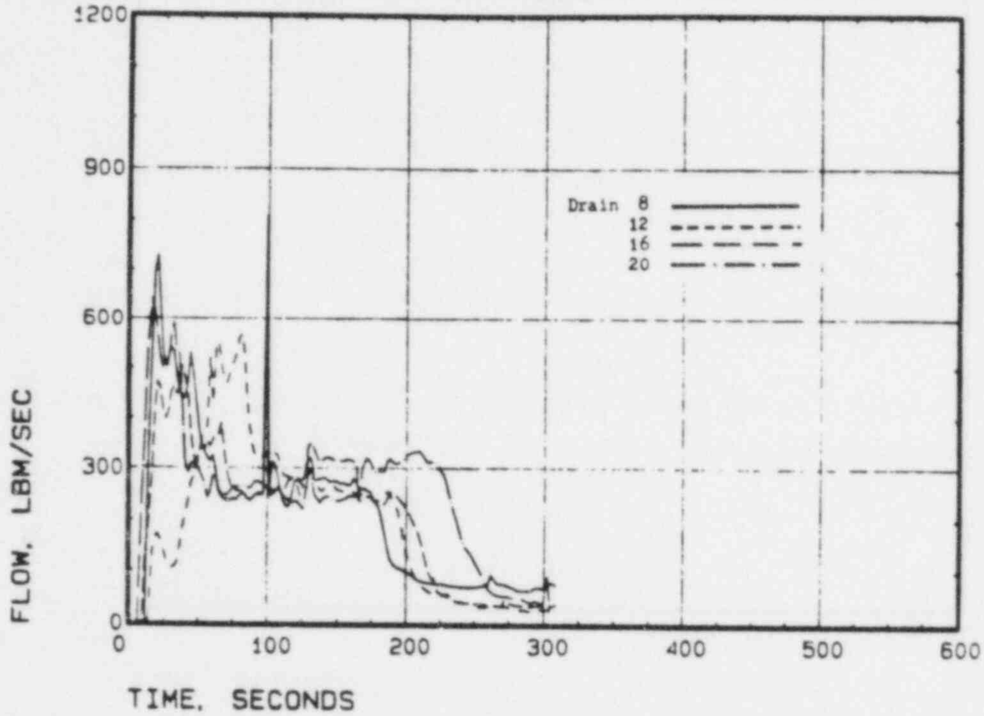

FIGURE 6.61. Model 3 Drain Flow Rate - Drains 8, 12, 16, and 20

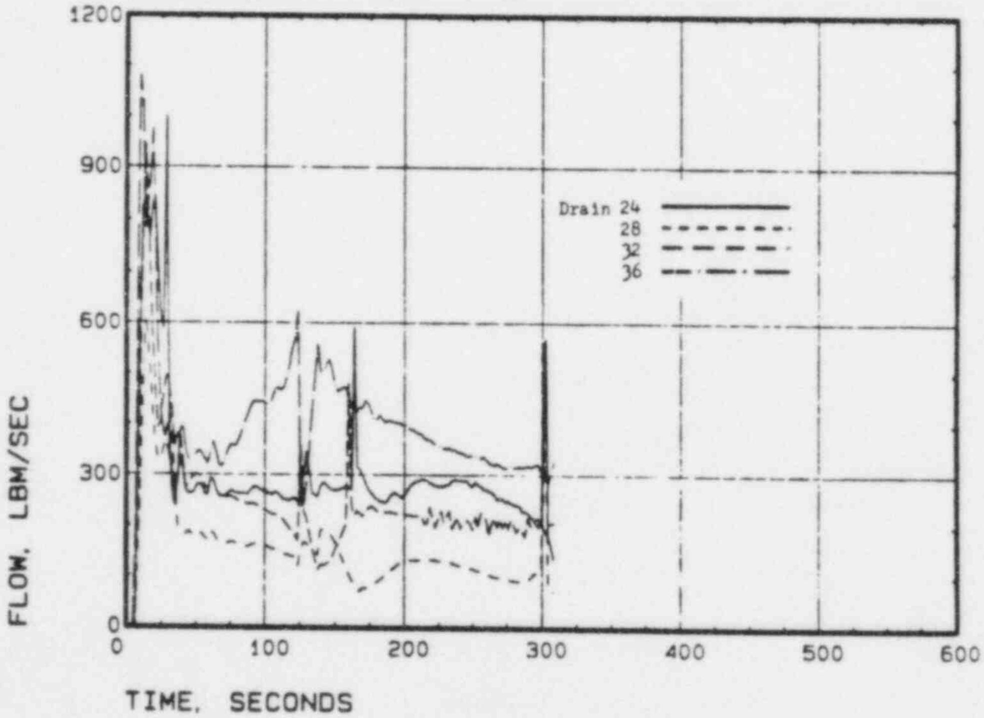

FIGURE 6.62. Model 3 Drain Flow Rate - Drains 24, 28, 32 and 36

Figures 6.63 and 6.64 show the total lower containment condensation and vaporization rates. These can be compared to the same results for Model 1. The vaporization rate shown in Figure 6.64 includes the revaporization of lower containment condensate and vaporization of the drain flows. The cumulative condensation and vaporization are shown in Figures 6.65 and 6.66.

The total lower containments liquid mass inventory in film and drop is shown in Figures 6.67 and 6.68. Assuming a drop size of 0.2 inches the total drop area at 300 seconds is about 12,000 ft.2. This compares to approximately 30,000 ft.2 of lower containment concrete which is all covered by film. The water inventory (film and drop) for level 2, the containment floor, is shown in Figure 6.69. Based on the total floor area, 100,000 lbm of water is equivalent to about 3.5 inches of water on the floor. The mass inventory of water in the sump/instrument tunnel is shown in Figure 6.70.

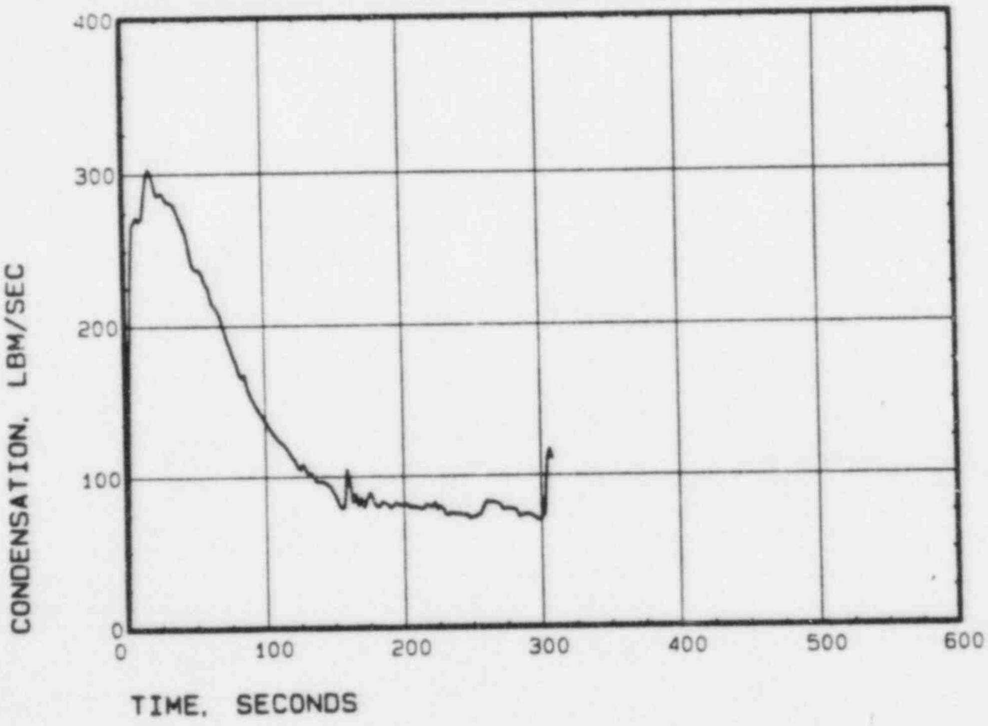

FIGURE 6.63. Model 3 Total Condensation Rate in Lower Containment

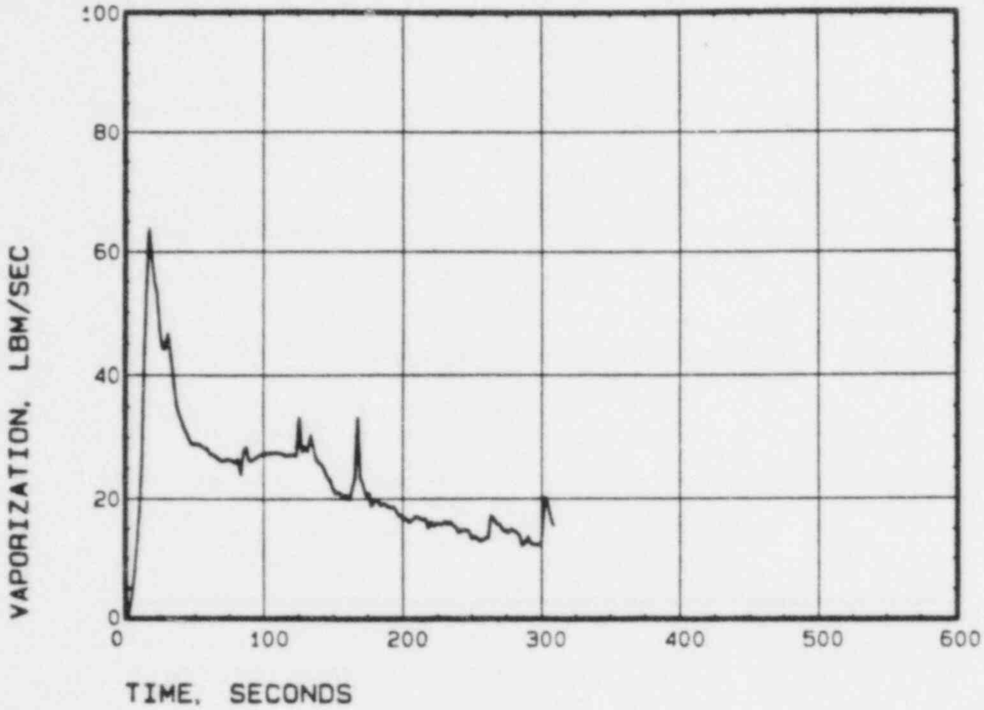

FIGURE 6.64. Model 3 Total Vaporization Rate in Lower Containment

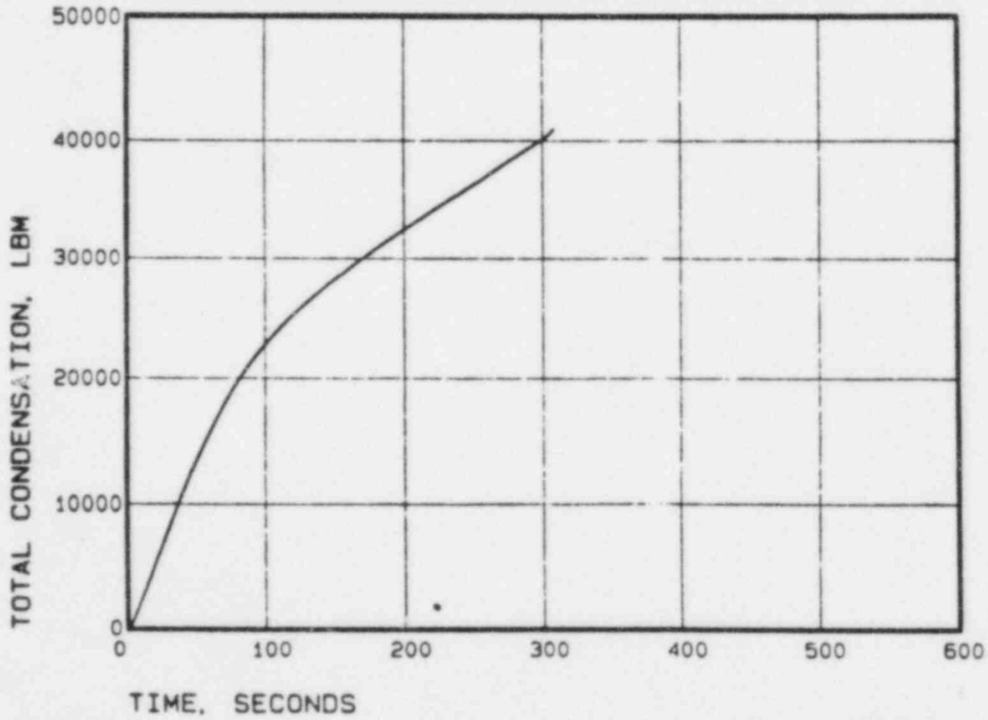

FIGURE 6.65. Model 3 Cumulative Condensation in Lower Containment

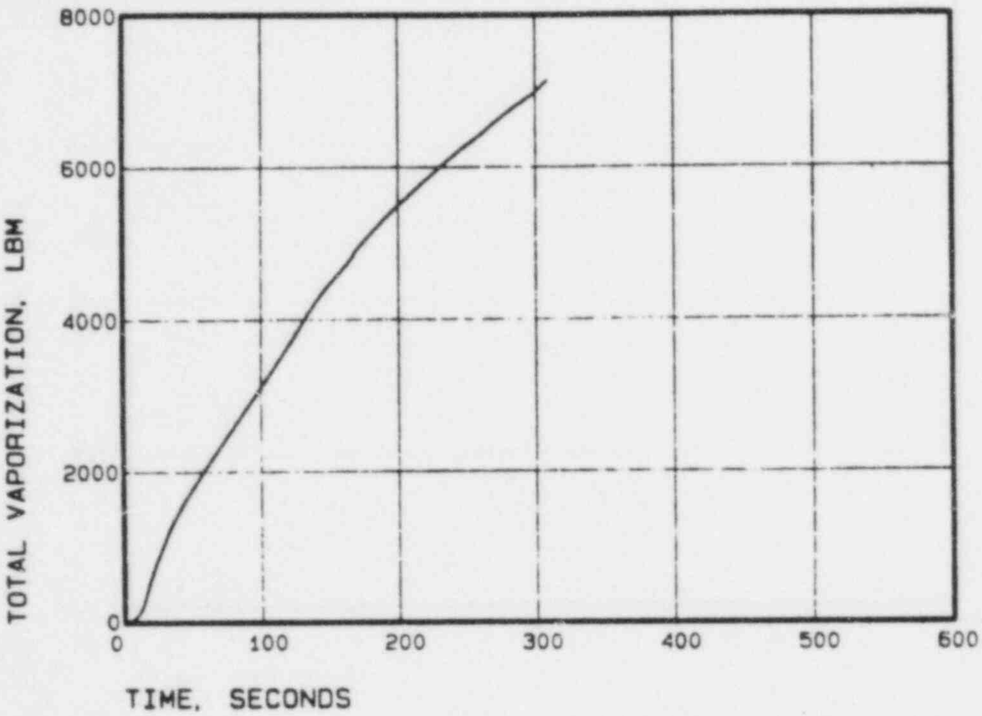

FIGURE 6.66. Model 3 Cumulative Vaporization in Lower Containment

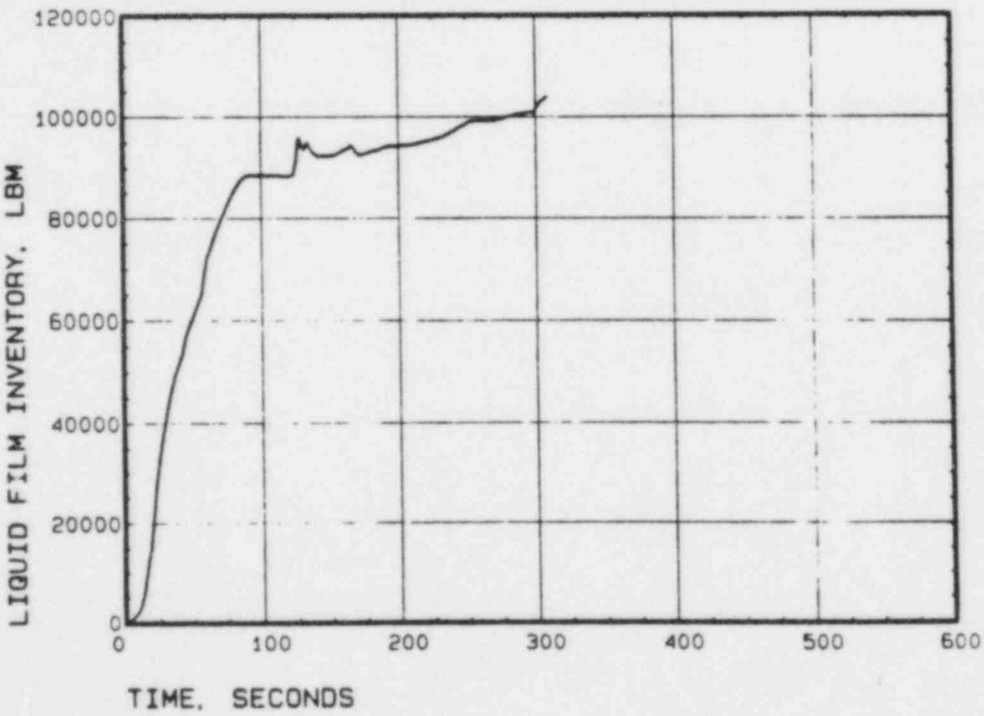

FIGURE 6.67. Model 3 Total Lower Containment Liquid Film Mass Inventory

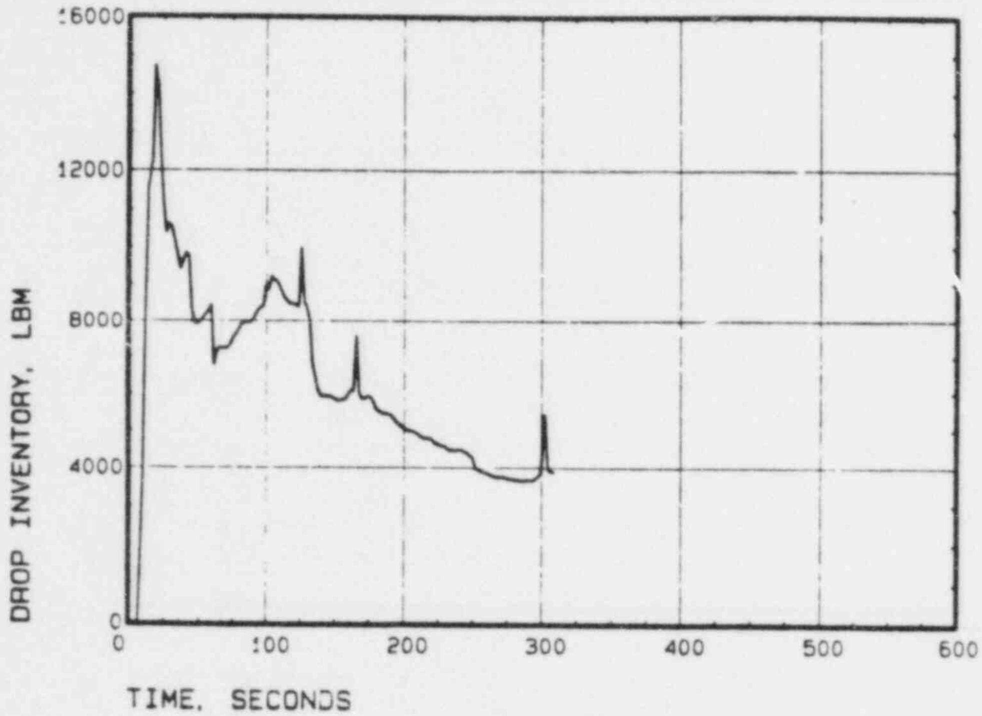

FIGURE 6.68. Model 3 Total Lower Containment Drop Mass Inventory

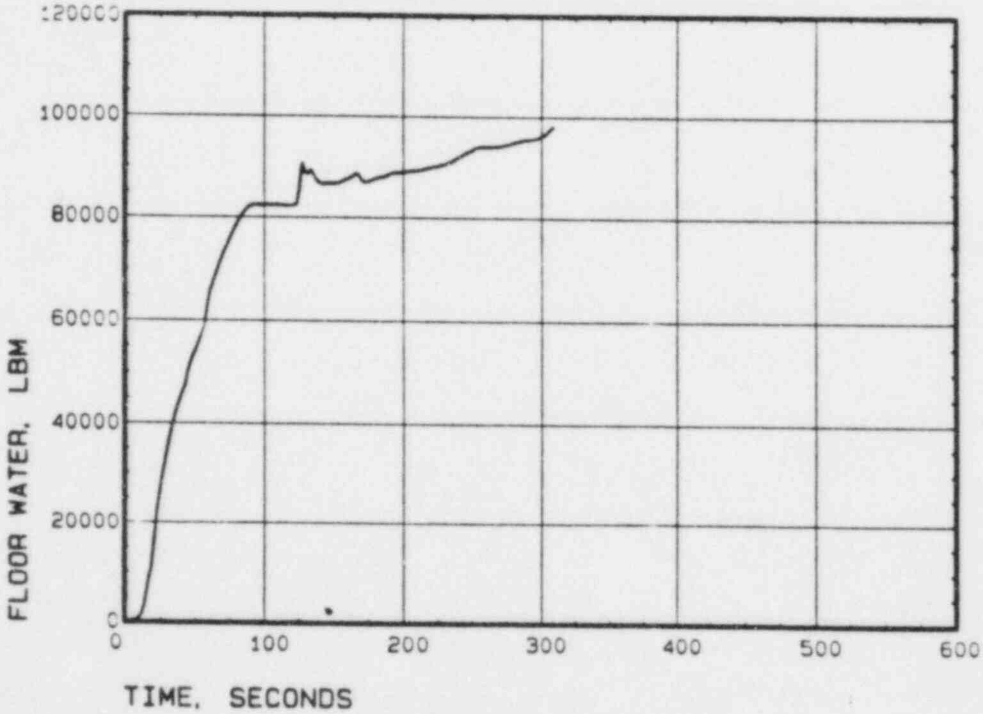

FIGURE 6.69. Model 3 Containment Floor Water Inventory

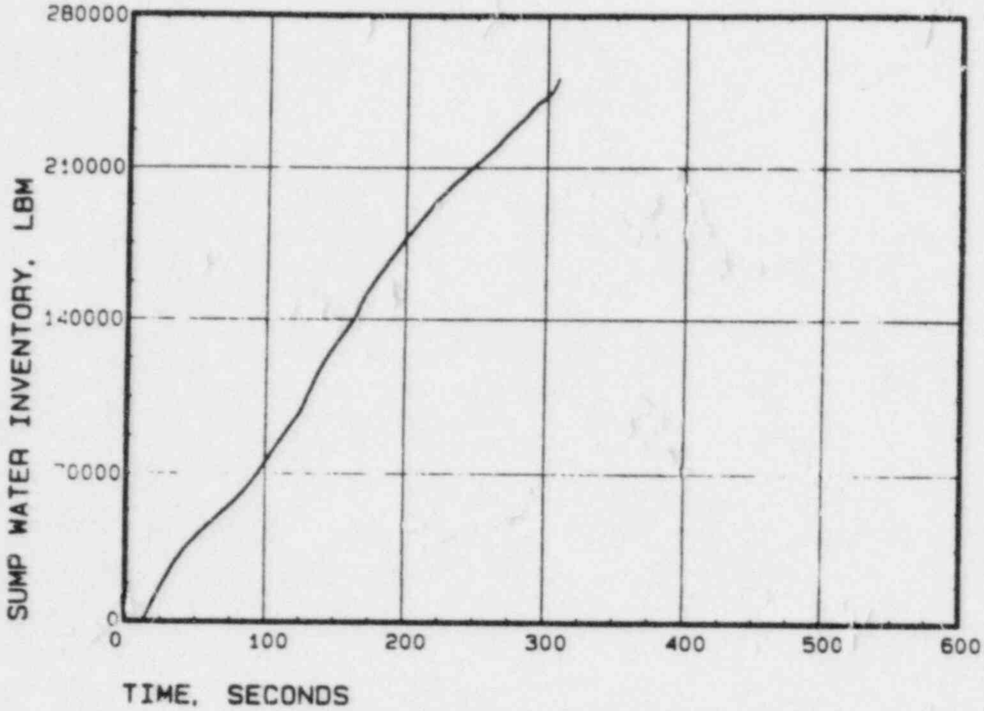

FIGURE 6.70. Model 3 Sump Water Inventory

6.4 Applicability of COBRA-NC Results of Other Ice Condenser Plants

As Table 6.1 indicated, the major containment parameters for the different ice condenser units are very similar, therefore it is expected that the containment response for these different units would be very similar. A cross section of the lower compartment at the ice condenser door elevation for the Watts Bar units is shown in Figure 6.67 and can be compared to Figure 2.2 for the Catawba Unit. The two figures indicate that the main primary system components are in the same relative locations such as the reactor coolant pumps, the steam generators, and the pressurizer. However the ice condenser drain locations in the Watts Bar units are grouped closer together around the locations of the steam generators and main steam lines. Where as in the Catawba COBRA-NC calculation, the containment node in which the break was postulated only had ice condenser drains directly flowing into this node; a similar noding for the Watts Bar unit would have ice condenser drains directly flowing into the break node. Therefore, the superheated vapor from the break would be immediately brought into contact with large amounts of subcooled water which would result in even lower break node temperatures for the Watts Bar containment as compared to the Catawba COBRA-NC calculation. Therefore it is expected that the Watts Bar containment temperature would be the same or lower than the calculated Catawba containment temperature.

TABLE 6.1

COMPARISON OF WATTS BAR AND CATAWBA CONTAINMENT PARAMETERS*

TOTAL NET FREE VOLUME
(FT^3)

	WATTS BAR	CATAWBA
UPPER COMPARTMENT	651,000	670,100
UPPER PLENUM	47,000	47,000
ICE CONDENSER	86,200	97,348
LOWER PLENUM	24,200	25,000
LOWER COMPARTMENT (ACTIVE)	289,014	273,218
LOWER COMPARTMENT (DEAD-ENDED)	94,000	71,799
TOTAL CONTAINMENT VOLUME	1,191,414	1,184,445

STEAM TOTAL MASS
(LBM)

	WATTS BAR	CATAWBA
UPPER COMPARTMENT	2,190,149.28	887,282.91
LOWER COMPARTMENT	937,333.62	442,493.77
ICE CONDENSER	2,342,527.49	2,342,572.49
TOTAL	5,470,055.39	3,672,349.16

SURFACE AREA CONCRETE
(FT^2)

	WATTS BAR	CATAWBA
UPPER COMPARTMENT	27,760	18,797.3
LOWER COMPARTMENT	53,744	31,912.6
ICE CONDENSER	16,391	16,391
TOTAL	97,895	67,100.9

* Values taken from LOTIC-III input

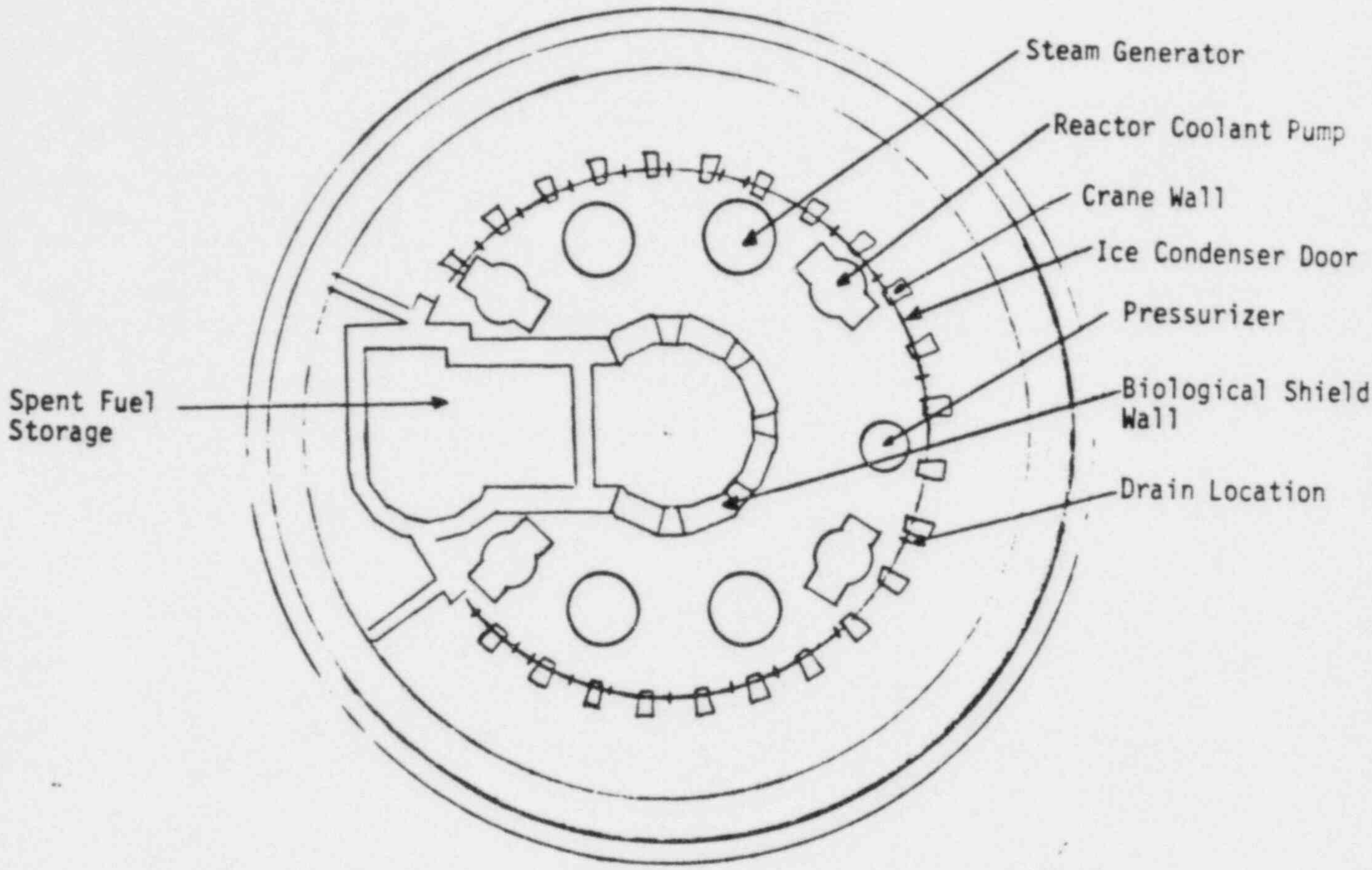

FIGURE 6.71. Watts Bar Lower Containment - Ice Condenser Door Elevation

7.0 CONCLUSION

Three COBRA-NC models were set up and run to simulate a main steam line break in the Catawba Unit 1 ice condenser containment. The three models taken together demonstrate the effect of the drain water and mesh resolution on the temperature distribution in the lower containment. A model with the drain flow discarded predicted a peak volume average temperature in a lower containment of 337°F. The local peak at the break cell was 358°F. Including the drain flow reduced the bulk and local peaks to 291°F and 330°F respectively. Finer noding in the vicinity of the break did not greatly affect the peak temperature values, giving a bulk peak of 285°F and a local peak of 334°F. The temperatures in all of the outer compartments were well below 300°F throughout the transient simulation for the cases that included the drain flow.

The major cooling effect is the vaporization of drops and films in the high velocity, high temperature region of the jet. The jet velocity was sufficient to entrain vapor and drops from a large portion of the lower containment. Vapor velocities were high enough to carry drops upward against gravity into the jet. The high steam velocities ensure that the drops will be well distributed in the lower containment with little chance of any self-shielding as the drops vaporize.

The jet momentum was sufficient to cause nearly uniform mixing of the lower containment. Very little air remained in the lower containment.

The ice condenser doors on the cold side of the containment closed as the break flow reached lower levels, but this did not adversely affect the temperature distribution in the lower containment. Circulation within the ice bed was sufficient to distribute some of the ice melt and drain flow around the containment. Large drain flows were predicted on the hot side of the containment where they could provide the greatest benefit in terms of cooling the jet.

The COBRA-NC models were intended to be realistic representations of the transient behavior in an ice condenser containment. However, when assumptions or approximations had to be made, a conservative approach was used. The following conservatisms have been defined in the COBRA-NC models.

1) The loss coefficients in the lower containment were based on losses for a sharp edge orifice in a pipe, using the minimum projected open area. This tended to reduce velocities resulting in less mixing, lower heat transfer coefficients, and less drop sweeping.

2) Superficial velocities, rather than velocities based on the restricted flow area, were used. The consequences of this approach are the same as for number 1 above.

3) The large vessels, reactor coolant pumps and the insulated piping were neglected as either heat sinks or surfaces that could be wetted with liquid films. This reduced the amount of vaporization from films and could have been particularly significant in the simulations without drain flows.

4) Heat transfer surfaces were removed from the total wettable surface areas when the surface temperature exceeded the film temperature even if the surface was subcooled. This caused reduced vaporization since the total film surface was made smaller.

5) The minimum film thickness was assumed to be 1/64 of an inch which is large compared to to the thickness of condensate formation on walls. This again reduced the total film surface area resulting in reduced vaporization.

6) The drops injected to simulate the drain flows were assumed to have a diameter of 0.2 inches., Westinghouse drain test data indicates a drop size of between 0.1 and 0.15 inches. The use of the larger drop size reduced drop entrainment by the jet and reduced the total drop surface area resulting in smaller vaporization rates.

7) The ice condenser door model was formulated such that the doors were hard to open and easy to close compared to the actual door test data. This minimized any cold air dumping into the lower containment which is an effective cooling mechanism.

8) The COBRA-NC entrainment and de-entrainment models were turned off. The velocities in the jet region are high enough to entrain drops off liquid films and drop deposition on surfaces would keep most, if not all, of the structure in the lower containment subcooled and wet. The approach used to incorporate the drain flow test data reduced the amount of vaporization from surfaces.

The COBRA-NC models, with these conservatisms, demonstrated a significant margin for the environmental qualification limit. Improved modeling techniques that could eliminate one or more of these conservations would lower the bulk and local lower containment temperatures even further.

REFERENCES

1. Westinghouse Letter SED-LEH-1092, October 10, 1984.

2. R. J. Davies, L. E. Hochreiter, W. M. Kavalkovich, N. Lee, P. A. Linn, T. C. Reck, and S. S. Tsai, "Ice Condenser Drain Test Results, Data Analysis, and Development of Drain Flow Models for the LOTIC-III Ice Condenser Containment Code", WCAP-10986, November 1985.

3. M.J. Thurgood, et all., "COBRA/TRAC - A Thermal-Hydraulics Code for Transient Analysis of Nuclear Reactor Vessels and Primary Coolant Systems," NUREG/CR-3046, Pacific Northwest Laboratory, Richland, Washington, 1983.

4. M. Ishii, Thermo-Field Dynamic Theory of Two-Phase Flow, Eyrolles, 1975.

5. J. Marshal and P. J. Holland, "Effect of Air Content and Mass Inflow on the Pressure Rise in a Containment During Blowdown," 2nd Australian Conference on Heat and Mass Transfer, pp. 339-346, February, 1967.

6. A. Uchida, A. Ogama and Y. Toyo, "Evaluation of Post Incident Cooling Systems of Light Water Power Reactors," Proceedings of the 3rd International Conference on the Peaceful Uses of Atomic Energy," Niva, Switzerland, August 31-September 9, 1964, Volume 13, New York; United Nations 1915, pp. 93-104. (A / Conf. 28 / p. 436).

7. T. Hsieh, N. J. Liparulo, "Westinghouse Long Term Ice Condenser Containment Code-LOTIC-3 Code," WCAP 8354-P-Sup.2, Westinghouse Electric Corporation, PWR Systems Division, Pittsburgh, Pennsylvania, February, 1979.

8. Catawba Unit I FSAR, Chapter 6.

PAGES 184 THRU 267 ARE CONSIDERED PROPRIETARY a,c
IN THEIR ENTIRETY